An Implantable Electronic System for InVivo Stability Evaluation of Prostheses in Total Hip and Knee Arthroplasty

Hao, Shiying

Award date:
2010

Awarding institution:
University of Bath

An Implantable Electronic System for In-Vivo Stability Evaluation of Prostheses in Total Hip and Knee Arthroplasty

Submitted by

Shiying Hao

For the Degree of Doctor of Philosophy of University of Bath

Department of Electronics and Electrical Engineering

March 2010

Table of Contents

List of Figures

List of Tables

Acronyms

AGC: Automatic Gain Control

CMOS: Complementary Metal–Oxide–Semiconductor

CMRR: Common-Mode Rejection Ratio

DVRT: Differential Variable Reluctance Transducer

FET: Field-Effect Transistor

LVDT: Linear Variable Differential Transformer

NMOS: N-channel MOSFET

OPA: Operational Amplifier

OTA: Operational Transconductance Amplifier

PCB: Printed Circuit Board

QALE: Quality-Adjusted Life Expectancy

QALY: Quality-Adjusted Life Year

rms: Root Mean Square

RSA: Radiostereometric Analysis

SNR: Signal-to-Noise Ratio

THA: Total Hip Arthroplasty

THR: Total Hip Replacement

TKA: Total Knee Arthroplasty

VCO: Voltage-Controlled Oscillator

Acknowledgements

I would like to thank my supervisor Prof John Taylor for supervision, support and encouragement throughout my PhD studies, and correcting my English.

I would also like to thank Prof Tony Miles for supervision and teaching me biomedical related techniques.

Thanks to Dr Sabina Gheduzzi and Dr Chris Bowen for valuable comments and modifications on my thesis.

I would like to express my gratitude towards Mr Andrew Matthews, Mr Richard Weston and Mr David Parker for help with building the system for in vitro experiments. Mr Andrew Matthews also helped me a lot on English corrections of my thesis.

Thanks to the Engineering and Physical Sciences Council (EPSRC) UK for providing funding for the project. Thanks to the websites http://www.recoverdiscover.com and http://www.the-health-pages.com for sharing their images.

Finally I'm very grateful to all the people in Room 2E 2.24, for sharing ideas and for being friends.

Abstract

Total hip arthroplasty (THA) and *total knee arthroplasty* (TKA) are relatively new biomedical techniques developed during the last century, which are frequently recommended for patients with joint diseases. In spite of their success and huge popularity, the postoperative failure rates for these procedures remain significant. *Migration* and *micromotion* of the implant are the primary indicators of its postoperative stability and many *in vitro* measurement techniques have been discussed. However, effective, practical methods to measure these metrics *in vivo* have proven elusive and the evolution of such a technique is the subject of this thesis.

An implantable, remotely interrogated electronic system for the *in vivo* measurement of both micromotion and migration in the axial direction is proposed. The main purpose of the device is to improve the ability of clinicians to assess the long-term stability of orthopaedic implants and also to plan and optimise patients' rehabilitation protocols. The system is based on a modified form of *differential variable reluctance transducer* (DVRT) in which the null-point of the system set automatically by means of a self-calibration process.

Simulations and preliminary *in vitro* measurements on the bench show that the self-calibration algorithm works correctly in spite of component tolerances and initial set up errors, allowing a gross displacement (migration) to be measured with a resolution of 15 μm and a range from 0 to 4 mm, and that the device can measure micromotion with an amplitude as low as 1 μm in the range from -200 μm to 200 μm. Accuracy of less than 10 % are achieved in both micromotion and migration measurements.

Prototypes of all the major components and sub-systems have been fabricated in CMOS integrated circuit (IC) technology as part of the project. Measurements support the feasibility of constructing an integrated version of the complete system for implantation and *in vivo* use in the future.

1. Introduction

THA, *total hip arthroplasty* or *total hip replacement*, was first performed by John Charnley in the 1960s [1]. It is now seen as one of the most important surgical advances of the 20th century, with 50,000 hips replaced in the UK with an overall cost of £140 million per annum [2]. Furthermore, TKA, *total knee arthroplasty*, which has been developed over last thirty years, is challenging THA in terms of volume. It is reported by the UK National Health Service (NHS) that more than 70,000 knee replacements were carried out in England and Wales in 2007 [3]. These numbers will increase even more in future as THA and TKA become more and more accepted, due to their contributions to both pain relief and function improvement in patients. The outcomes of such surgery are also encouraging [4-7] Many other studies have also verified that THA and TKA are highly beneficial and cost-effective procedures [8-9].

In spite of this success, a high postoperative failure rate has been increasingly reported in recent years. These failed implants usually led to *revision surgery*, which in addition to being more expensive than the initial procedures has inevitable adverse effects such as higher operative complication rate and a reduction in prosthesis durability [10]. As a result, much effort has been made during last few decades to understand better the failure mechanisms involved. This has led to corresponding technical advances which have improved prosthesis design for long-term survival.

Many investigators consider aseptic loosening, either symptomatic or asymptomatic, to be the most common failure mode in both THA [11,12] and TKA [13,14]. Hence, the extent of post-operative implant stability, which largely determines the incidence of loosening, is an important predictor of durability for both cemented and, in particular, uncemented prostheses which rely on bone-ingrowth for long term fixation [15-17]. In addition, it is also important to reduce the risk of long term failure of implants [18].

Prostheses with inadequate stability tend to suffer from excessive motion at the prosthesis-bone or cement-bone interface under daily weight-bearing loads [17], leading to ultimate failure. As a result the post-operative stability of implants is quantified in terms of their postoperative *migration* and *micromotion*. The former is nonrecoverable and permanent movement of the implant, while the latter is load induced and recoverable. Therefore, evaluation and minimization of these two modes of movements are key tasks concerning the improvement of THA and TKA technology [20].

There have been many studies that focus on the post-operative stability prediction of implants by measuring their *micromotion* and *migration in vitro* (outside the body) via Differential Variable Reluctance Transducer techniques) or measuring *migration in vivo* (inside the body) via radiographs. Recently a study on *micromotion* measurement by means of radiostereometric analysis (RSA) was reported [100], leading to a more comprehensive description of the post stability of implants and a better understanding of failure mechanism. These techniques are briefly discussed in Section 2.2.2 and 2.2.3. In spite of the availability of methods for monitoring *migration* or *micromotion*, there is currently no electronic method for direct *in-vivo* measurement of both *migration* and *micromotion* of an implant with a resolution up to the order of μm.

In this project we describe an electronic device which has potential to combine *in vivo* measurement of both *micromotion* and *migration* in the context of applications such as THA and TKA. The device acts as a DVRT (Differential Variable Reluctance Transducer) sensor incorporating a RL-Wheatstone bridge as its essential part with signal processing electronics realized in 0.35 μm CMOS technology for micro-movement testing. The axial *micromotion* of the implant is detected by observing the electrical output signal of the bridge in that the output signal amplitude can be modified by moving a ferrite core inside a pair of inductive coils arranged in the bridge, with the core attached to the implant and the coils fixed to the bone. This system is electronically self calibrating, with additional advantages of allowing an accurate *micromotion* measurement and providing a record of long-term implant settling (*migration*). With the use of this device, an in-depth analysis of the operation of the system is presented and validated by detailed *in-vitro* bench measurements. These measurements indicate a limiting axial resolution of about 1 μm for *micromotion* with a detectable range between -200 μm to 200 μm, and an axial resolution of 15 μm for *migration* with a range between 0 to 4 mm. Although the system as described in this thesis is designed for measuring the motion of the stem in the axial direction at the prosthesis-bone interface, it can in principle be adapted to detect motion in other planes.

2. Background

In this chapter, some previous work on THA and TKA is investigated and summarized. The development, characteristics and evaluation methods employed in THA and TKA are introduced and discussed.

2.1 Total Hip Arthroplasty (THA) and Total Knee Arthroplasty (TKA)

THA, *total hip arthroplasty or total hip replacement*, and TKA, *total knee arthroplasty*, are the fundamental research background of this project. In this section their history, development and shortcomings as well as revisions, are described.

2.1.1 Introduction of THA and TKA

THA and TKA are relatively new biomedical techniques developed in the last century. They have both undergone substantial developments and benefited a great number of patients over the last four decades.

2.1.1.1 Summary

Total hip arthroplasty, a surgical treatment usually recommended for patients with primary osteoarthritis (Swedish Hip Registry, annual Report 2007 [24]), is one of the greatest triumphs of modern medical science in the last century [21]. Although it started gaining popularity in the late 1960s, the history of the hip surgery could date back to the 19th century. In the early days, the survival rate was always very low due to the poor knowledge of anesthesia and aseptic precaution [22]. Whereas much effort had been made in the development of surgical techniques throughout the 19th century, the breakthrough didn't come until 1923, when Dr. Marius Smith-Peterson moulded a piece of glass cup into an arthritic femoral head to cover and reshape it, and reconstruct its function. This was the start of modern hip replacement which coincided with the era of plastic materials for such surgery. In 1938 Philip Wiles proposed the first THA using stainless steel components fixed to bones with screws, without any satisfactory practical results however [104]. Original operations of hip replacement always failed, however, due to a lack of stiffness and durability. For this reason, implants made of metal materials were then developed for long-term use.

The first metallic hip replacement was performed by Austin Moore in 1942, with the head of the prosthesis made of vitalium [106,107]. In addition, Thompson (in 1951 [108]) and Moore (in 1940 [109]) separately developed a hip replacement with an entire ball of the hip and a metal stem, which is called hemiarthroplasty [32]. Edward Haboush and Kenneth McKee developed implants with the use of dental acrylic cement to secure the long term fixation in late 1940s [105]. Haboush also reported the first use of methacrylate for fixation between metal cups and bone in 1953 [22]. Innovations then came in 1960s, when THA was established as a practical and reproducible procedure by John Charnley [105]. Charnley advanced the idea of replacing both the *femoral head* and *acetabulum*, and carried out such surgery successfully with a steel femoral component and a plastic cup in 1961 [32]. Additionally, he fixed the implant to the bone with acrylic cement. This was the original low friction *total hip arthroplasty*. This technical innovation has resulted in a large amount of published research on the subject of improving the prosthesis design during last four decades, which consequently made contributions to increasing the survival rate. It was reported by Swedish Hip Registry in 2007 that the national average survival rate of the primary THR was 94.7% ± 0.4%, with revision or extraction of the prosthesis as the end point [24].

Due to the high survival rate and long-term stability, THA has gained more and more popularity and become one of the most frequently performed reconstructive procedures in orthopaedic surgery [26]. A survey in 2002 shows that more than 150,000 primary total hip replacements are performed annually in the United States [27], with an approximate increase of 50% per 100,000 persons between 1990 and 2002 [28]. The annual number of procedures is expected to rise further by 100,000 in the next 30 years [22]. In the UK there were about 38,000 hip replacements performed in 1994/1995 reported by NHS [29], and this number increased significantly to 46,000 in 1996 [30] and nearly 50,000 currently [2]. The need for hip replacements could double within the next 30 years, according to the BBC [30].

The great success of hip replacements has substantially promoted innovation of arthroplasty of other joints, in particular the knee, which has been developed in parallel line with THA. The first total condylar knee was introduced by Ranawat, Insall and Walker in 1974 [110]. In the early days, however, TKA was considered to be a poor operation due to the low survival rates. It was not until late 1980s that surgeons realized that it was necessary to resurface the joint and reproduce normal knee anatomy with a

low friction joint during the operation [33], and significant improvements in flexibility and survival rate of knee prostheses have been subsequently introduced with this new concept. Diduch reported an 18-year survival rate of 87% among the patients with an average age of 51 years [34], while Gill reported an overall survivorship of 96.5% at 18 years among patients of the same age with the use of a cemented Total Condylar Prosthesis [35]. Seon reported an average postoperative knee flexion of 130.7º using high-flexion prostheses and 128.5º with mobile bearing prostheses [36], both of which were sufficient enough to restore function as the flexion range of a normal knee is about 130º [37]. As a result of this development, TKA is now challenging or surpassing THA, with 70,000 knees replaced in England and Wales in 2007 [7], and 581,000 in the United States annually at a cost exceeding $11 billion [38]. In the US this number is expected to rise to 3.4 million by 2030 [39].

2.1.1.2 Mechanism

Fig 2.1a shows a picture of an unassembled prosthesis used in the total hip replacement. As noted, an artificial hip prosthesis is composed of an acetabular shell, a cup-shaped liner, a ball as the femoral head and a stem. During the operation first an incision in the surrounding soft tissues is created to allow access to the damaged hip. After the hip is exposed, the damaged ball (femoral head) is removed and the hip socket (acetabulum) is reamed to allow the replacement. Then the prosthesis is placed inside the body, with its acetabular shell and femoral head in the cavity of the pelvis, and its stem placed into the top of the thighbone. A polyethylene liner is sometimes inserted between the acetabular shell and the femoral head as a bearing surface. The diagram of an assembled hip prosthesis placed inside the bone is shown in Fig 2.1b.

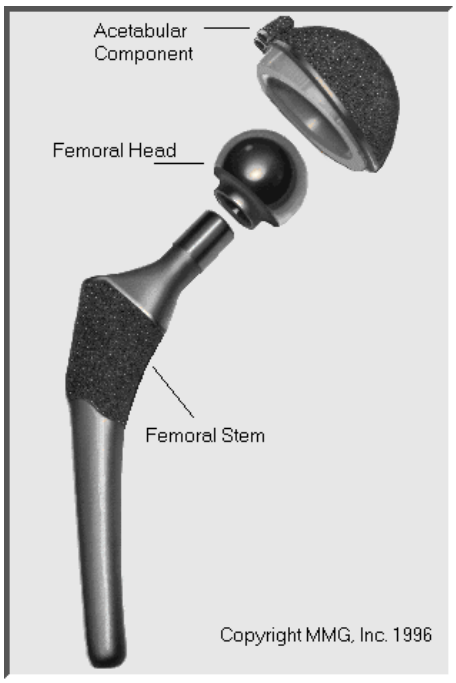

Fig 2.1a An artificial hip joint used in THA [112] (Image reproduction is permitted)

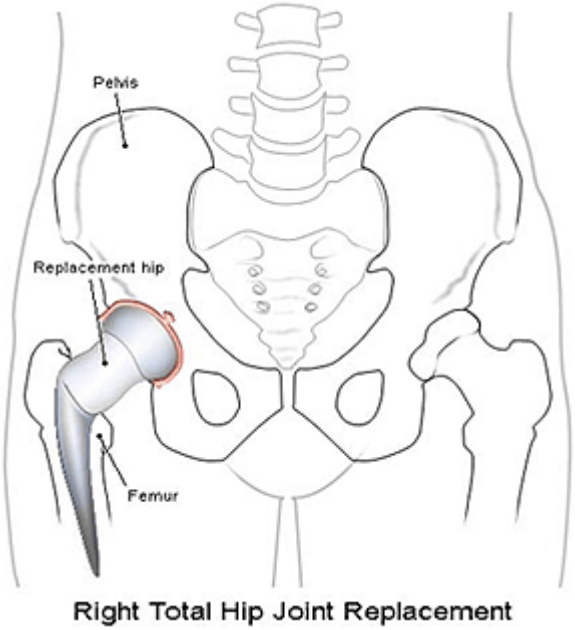

Fig 2.1b Total hip joint replacement [111] (Image reproduction is permitted)

Fig 2.2 is a picture of a knee implant this comprises four parts: a femoral and a tibial metallic component, a polyethylene tray inserted between the two metallic components and a polyethylene button placed on the articulating side of the patella. The patellar component can sometimes be omitted.

During the surgery the damaged cartilage and subchondral bone are resected and the bone ends are shaped so to accommodate the replacement articulation.

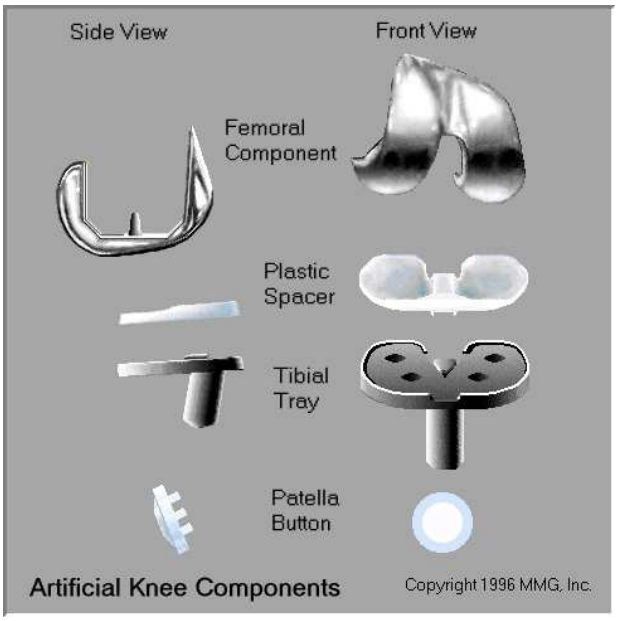

Fig 2.2 Total knee replacement [112] (Image reproduction is permitted)

Joint prostheses can be fixed with or without cement. The first artificial hip joint in THA developed by Charnley was attached to the bone via *cement* (Fig 2.3). It was one of three contributions to the evolution of THA made by Charnley (the other two contributions are the concept of low friction torque arthroplasty and the introduction of high-density polyethylene [41]). As the traditional fixation method, cemented prostheses have been proven to be exceptionally durable [42] [25] [41] [43], and are still used today [19,46,47]. Williams et al. [44] reported a 100% survival rate for the cemented Exeter stem at the time of the ten-year follow-up. The Swedish Hip Register

reported a 98% survival rate for both the Exeter and the Spectron stems at seven and nine years, respectively [45].

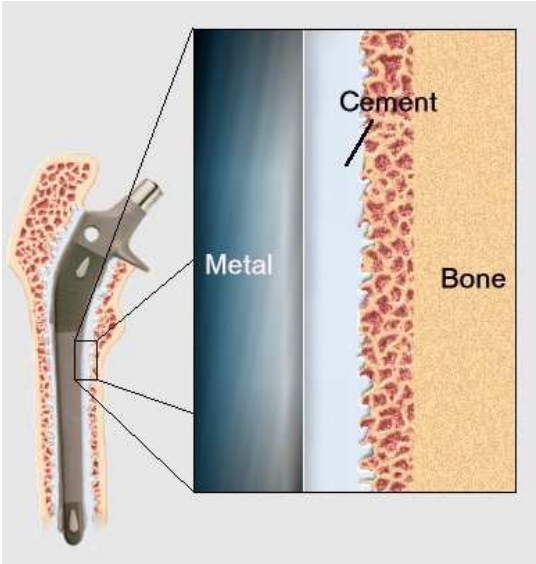

Fig 2.3 A hip prosthesis with cement [112] (Image reproduction is permitted)

Although good survival rates of implants have been achieved with the development of cement techniques, shortcomings of this fixation method such as implant loosening and loss of bone stock [42], emerged especially among young patients or patients with high levels of activity. These problems were first described in terms of "cement disease" because of misinformation. In reality, these problems are now recognised as originating from wear-debris particles [48]: tiny bits of metal or plastic from joint replacements called *debris* induce an inflammatory response from the tissues around the implant, causing the bone dissolve and consequently resulting in implant loosening [49]. In order to improve the stability and durability of the prosthesis to meet the requirements of the increasing number of young patients and active older patients, as well as the increasing life expectance [50], cementless implants were developed. A cementless prosthesis relies on direct fixation to the surrounding bone; this is achieved by introducing surface features on the implant. The bone then can grow into the surface of the prosthesis, achieving a mechanically sound interface between the implant and bone, which is the prerequisite for the long-term durability of the fixation [51]. Bone ingrowth also reduces

the *migration* of wear debris on the implant-bone interface [31]. An implant without cement is shown in Fig 2.4.

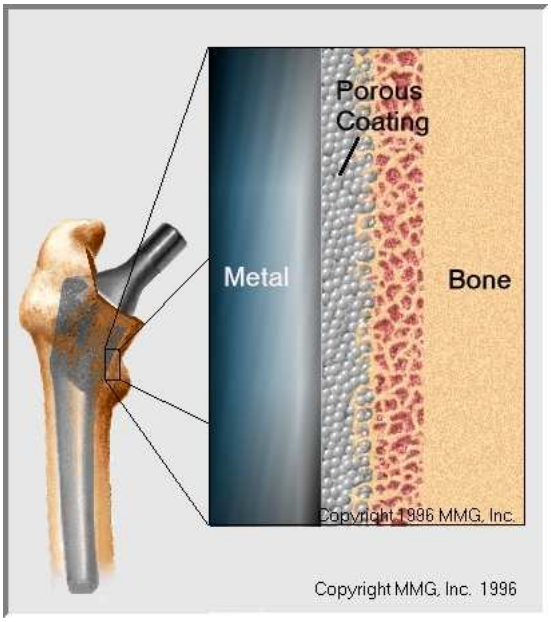

Fig 2.4 A hip prosthesis without cement [112] (Image reproduction is permitted)

Recent studies [52-54] have shown that the performance of implants with cementless fixation are excellent when tested in the short or intermediate-term (in Archibeck's study even a survival rate of 100% at ten years with the use of the Anatomic Hip stem is reported [54]). Cementless implants in the first generation were restricted to young patients due to high cost. However, with the further refinements of cementless techniques and the increasing number of the active elderly, the value of this method of fixation should not be dismissed [55].

A study of the trends of hip implant selection in North America from 1995 to 2001 showed that the rate of use of stems with cement fell by 27.6%, and the use of cemented cups reduced by 4.2% [26]. One reason for the decreasing popularity of cemented prosthesis is that cementless fixation has been widely accepted over the last decade due to the increasing number of young patients and active old patients with hip disease. Another reason is the emergence of hybrid total hip replacement [56-58], which involves a prosthesis that includes a cementless acetabular component and a cemented

femoral component, with an effort to maximize the durability and the longevity of the implant [59].

2.1.1.3 Benefits of THA and TKA

THA and TKA can relieve pain and restore functions of arthritic hips, improve the prosthesis durability, optimize the stability and mobility of the articular couple [6], and eventually benefit health-related quality of life [7] [8] in many aspects, such as sleep and rest, emotional behaviour, social interaction and recreation and pastimes [9]. The outcomes of such treatments are also encouraging: the satisfaction rate as reported in previous investigations [4,5] is more than 80% after primary TKA; Ng [7] and Ramiah [6] claimed that quality of patients' lives has been improved and sustained up to five years after THA. In addition, quality-adjusted life expectancy (QALE) rises after either THA or TKA. Researchers found that QALE was increased by 2 years for patients aged 85 and older after THA [9]. For TKA, a survey done by Harutyunyan shows that the average QALE increased by 1.1 years per patient after TKA [60] and in an ABC news report the increase is as much as 2.5 years among most patients receiving knee replacements [61].

In addition, THA and TKA are both cost-effective procedures [3]. Take THA as an example: in Navarro Espigares's investigation the cost per quality-adjusted life year (QALY) gained for hip interventions was about €7936 [62], with a threshold of €30,000 considered acceptable; In the US a bulletin on the effectiveness of health service interventions reported cost effectiveness for total hip replacements ranging from $4600 to $80,000 per QALY gained [29]. The average cost per QALY of THA compared with other Medicare services in the US is shown in Fig 2.5, demonstrating THA to be a reasonable medical treatment in terms of the cost effectiveness (the threshold is about $50,000/QALY [63]). The cost effectiveness of TKA compared with other medical interventions is also unparalleled: In Lansingh's report the cost per QALY is approximately between $6500 and $12,700 [64], which is quite acceptable. The cost per QALY of THA and TKA could vary with the severity of the pre-operative state and age and health condition of the patient [29]. The average cost including implants for a THA and a TKA are both about £6000.

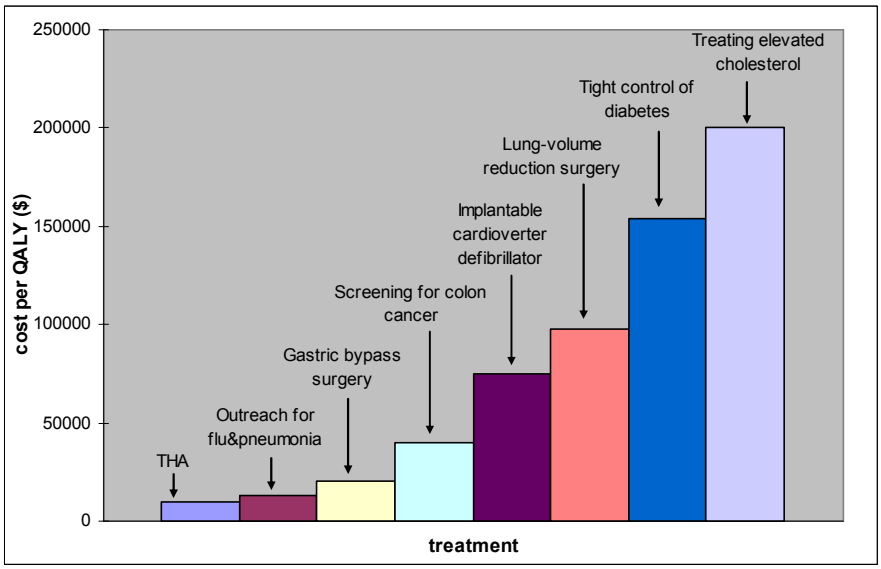

Fig 2.5 Cost per QALY for different Medicare services. The columns from left to right represent: THA, outreach for flu&pneumonia, gastric bypass surgery, screening for colon cancer, implantable cardioverter defibrillator, lung-volume reduction surgery, tight control of diabetes, treating elevated cholesterol. All the data are collected from [66].

With so many advantages, total hip replacement is now the second most common elective surgical procedure in the UK [67], the commonest one being the cataract surgery [68], while total knee replacement is also one of the most common major orthopaedic operations [33]. A dramatic growth for both is expected in the next few decades with improvements in surgical techniques and implant design, development of new materials, better understanding of the failure mechanism and an increasingly aging population.

2.1.2 Postoperative Failure

In spite of the success, a high postoperative failure rate has been increasingly reported in recent years. Failure rates ranging from 10 to 20 percent for knee prostheses during the first five years have been shown Ranawat [69] and Skolnick [70]. Similarly, Losina [71] found that 4.4% of prostheses failed by the end of the fifth year after primary THA. These failed implants usually led to *revision surgery*, which in addition to being more expensive than the initial procedures (cost at least 35% more than the primary procedure

in THA [72]) has inevitable adverse effects such as higher operative complication rate (infection, exposure, loss of bone stock and ligament damage [73]) and a reduction in prosthesis durability [10]. As a result, increasing attention has been paid to the postoperative failure mechanisms of THA and TKA, As a result, much effort has been made during last few decades to understand better the failure mechanisms involved [11,14,74-76]. This has led to corresponding technical advances which have improved prosthesis design for long-term survival.

Survival of a joint prosthesis is closely related to the quality of surgery, patient factors and implant choice, with the first the greatest variable [77]. Factors leading to failure for hip implants include aseptic loosening, dislocation and periprosthetic fracture, as well as infection [78]. The failure mechanisms for the knee replacements, on the other hand, are mainly comprised of loosening, instability, sepsis, extensor mechanism power loss, poor range of motion, bone fractures and prosthesis facture [13].

Despite these various mechanisms, many investigators consider aseptic loosening, either symptomatic or asymptomatic[1], to be the most common failure mode in both THA and TKA in many studies [11,14,74-76]. Hans Lindahl [74] reported that aseptic loosening was responsible for 2036 [60.1%] of the reoperations in the Swedish National Hip Arthroplasty Register from 1999 to 2000. Andrea E. Buckwalter [75] reported 10% of 357 hips required a revision because of aseptic loosening at a period of twenty-five years. As for the knee replacements, in Ducheyne's survey [14] loosened knee implants accounted for 5.8% and in Friedmen's investigation [76] 73% of the revision knee implants were due to loosening.

The predominant reason for loosening in THA is the generation of wear debris. It has been established that the debris generated from the wear and corrosion of implant materials will ultimately lead to aseptic loosening at the bone-implant interface by the formation of a granulomatous tissue and osteoclastic and histiocytic response [12]. Aseptic loosening of a hip implant can also result from poor patient selection, modulus mismatch between bone and implant or fixation failure [78].

On the other hand, the major cause of loosening in TKA is malalignment, which is strongly associated with the surgical factors at the time of the arthroplasty. Malalignment may produce off-center weight-bearing loading on the tibial component

[1] Most of the patients with loosening implants are symptomatic; asymptomatic loosening is rare, and may be detected by radiographic assessment in periodic follow-up examinations [77].

of the prosthesis and thereby place the prosthesis at a high risk of imbalance and loosening. As a result, correct alignment of the prosthesis during the operation, i.e. the line between the center of the femoral head and the center of the ankle should pass over the center of the knee, is essential to its long-term survival. Other factors contributing to the loosening include poor initial fixation, stress on the implants and the bone stock. Loosening caused by wear debris in TKA is not as common as in THA [13] due to a different wear mechanism.

Since loosening is one of the most common failure modes, the extent of post-operative implant stability, which largely determines the incidence of loosening, is an important predictor of durability for both cemented and, in particular, uncemented prostheses which rely on bone-ingrowth for long term fixation [15-17]. Previous studies have shown that prostheses with inadequate stability tend to suffer from excessive motion at the prosthesis-bone, or cement-bone interface for cemented implants, under daily weight-bearing loads [17], leading to ultimate failure. As a result the post-operative stability of implants is quantified in terms of their postoperative movement. The characteristics of such movements are detailed in Section 2.2.

2.2 Methods of Post Stability Evaluation for THA and TKA

With the purpose of optimizing the implant configuration and increasing the rate of survival, which is the ultimate objective of this project, the design of an implant must be evaluated before general release by predicting its long-term stability. The main predictor for the long-term stability of an implant is its post-operative movement, as described in the previous section. There are two types of movement due to loosening: *micromotion* and *migration*; both can be measured *in vitro* or *in vivo*.

2.2.1 Predictors for Postoperative Stability – *Migration* and *Micromotion*

There are two sorts of motion of a hip implant caused by loosening: *migration* and *micromotion*. They are shown in Fig 2.6.

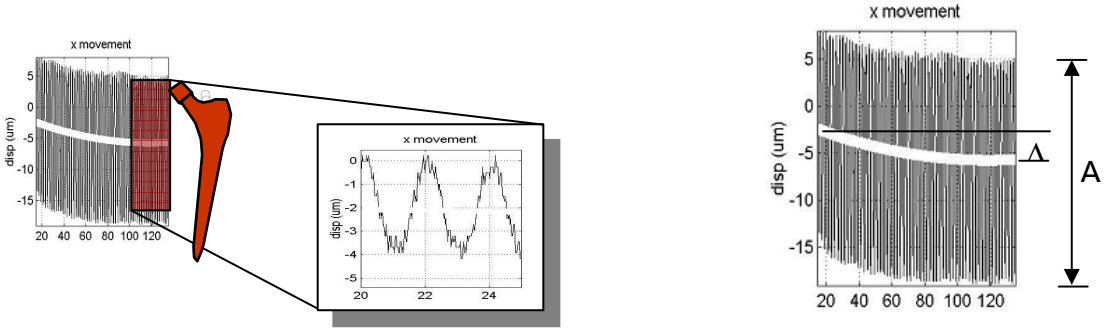

Fig 2.6 Example of *migration* (Δ) and *micromotion* (A) from *in-vitro* measurements [79]

2.2.1.1 *Migration*

Migration is the *unrecoverable* movement due to loading, like walking, standing on one leg or running. It reveals the continuous embedding of the implant into the host bone [79]. Thus the quality of fixation can be estimated by the amount of the implant *migration*. Gross *Migration* can generally be measured by radiographs. Walker *et al* [80] showed that failed stems had migrated by a longer distance (about 4.32 mm) than that of successful cases. Also, *migration* at the stem-cement interface occurred in almost every failed stem, compared with a rate of 24% in successful ones. Kobayashi's study [81] proved that a mean *migration* of < 0.4 mm at two years would predict a ten-year survival rate of 95%, and a 50% chance of revision over ten years was also predicted by two-year *migration* > 2 mm. In Skwara's study of the primary stability of tibial components in TKA a *migration* of more than 2 mm was defined as failure [102]. Based on these studies, *migration* can be used as an accurate predictor of implant loosening and failure, which eventually benefits the implant design. Kobayashi [81] suggested that any prosthesis that was newly designed should be followed-up radiologically in a clinical trial for first two years before general release, and the implant status of individual patients should be measured after five years to determine whether close review was still needed for those patients.

2.2.1.2 *Micromotion*

Unlike *migration*, *micromotion* is the *recoverable* relative movement between the implant and the host bone; it is a function of elasticity.

Evidence suggests that early implant *micromotion* of uncemented hip implants is strongly correlated with clinical loosening and hence premature failure [82]. This is because excessive movement will inhibit bone ingrowth onto the implant surface, which is the base of the biological fixation [17,97]. Burke [83] has reported that *micromotion* of 75 μm began to induce connective tissue ingrowth. In a canine model Pilliar [84] found that *micromotion* greater than 150 μm resulted in the formation of a pure fibrous tissue interface between the bone and the implant, which is harmful to the implant stability.

In this project, a sensor is designed to measure both *migration* and *micromotion* of the implant for the prosthesis design evaluation.

The principal components of postoperative *micromotion* and *migration* can be resolved according to a coordinate system defined on the implant and therefore can be classified in term of translations and rotations. These two modes of motion always occur at the same time however the prevalence of one with respect to the other depends on the applied load. In a hip implant, for instance, translation is dominant movement during single leg standing or walking, while rotation is dominant during stair climbing [17]. As for knee implants, the extent of medial and lateral translations during step activity is higher than during pivot activity [103]. The tendency of the postoperative motions of an implant also depends on the implant material. For instance, according to Hans Hyldahl's study on a 24-month follow-up with TKA [23], there was a tendency to anterior tilt of the metal-backed completely cemented components, while with all-polyethylene completely cemented components these were evenly spread around zero. In our project, only the axial translations along the bone have been measured for simplicity.

2.2.2 *In-Vitro* Measurements

It is important to highlight that the sensor designed in this project is for *in vivo* measurement. At present, there is no viable electrical or mechanical method for such experiments. Instead *in vitro* measurements which are carried out outside the body using artificial or cadaveric bones are carried out to infer the behaviour of implants *in-vivo*. With the use of a displacement sensor system, loading configurations and bone substitute materials, conditions that occur *in vivo* can be estimated and the implant status predicted, helping with assessment of the implant design before clinical trials.

1) Displacement Sensor

The fundamental device in the *in-vitro* measurement system is a displacement monitoring sensor. Several types of sensing devices have been used. The traditional one is a mechanical dial gauge, with disadvantages of limited accuracy (more than 5 μm) and degree of freedom. Then LVDTs (Linear Variable Differential Transformers) [86,87] were developed for better resolution (generally around 5 μm). Three-dimensional translation and rotation detection can be achieved by holding systems with several LVDTs [88] or eddy current transducers [89, 90]. Higher resolutions can be obtained in measurements with the use of optoelectronic devices [91].

Displacement sensors can be classified according to whether the predominant motion is known prior to the experiments or not [82]. When the motion is defined, only one-dimensional detecting sensors are needed. When no assumption on the predominant motion can be made, the movement needs to be monitored by devices with six degrees of freedom; these devices more difficult to implement. In this project, the predominant motion is defined as that in the vertical (z or axial) direction.

2) Loading Configurations

The motion and loosening of an implant are caused by daily loading, like single-legged standing (the most frequent one), stair climbing and running. Thus *micromotion* and *migration* can be assessed by applying loading mimicking these activities to the prosthesis; this is usually achieved by a material testing machine [85,91]. To simulate activities like standing or climbing, a vertical directed force is exerted on the head of the implant after the host bone is fixed [82], and then measurements of the implant displacement can be carried out. Usually displacement information is recorded for several times during each loading cycle so that both *micromotion* and *migration* can be measured.

3) Bone Substitute

Composite femora, such as Sawbones, can be used instead of real bones in most tests with good performance [82], though in some cases real bones are still used [91].

In vitro evaluation of the postoperative stability of implants has been well developed and widely used during last four decades as a convenient and low-cost method with simply constructed apparatus and high resolution. The shortcoming of this method is that the extent of the implant displacement inside the body could be interfered by environment factors (surrounding tissue, body temperature or bone ingrowth), patient factors (sex, age, activity et al.) and surgical factors, which are difficult to be estimated or predicted *in vitro*. For these reasons, *in vivo* measurements have been developed for clinical investigations.

2.2.3 *In-Vivo* Measurements

Although some good results can be achieved in *in-vitro* measurements, *in-vivo* experiments are still needed to get the precise position of an implant by observing its status inside the body. For this reason, X-ray techniques have been developed. The conventional method uses standard radiographs [80, 92], with an accuracy of 0.5 mm. To improve the sensitivity of radiographic measurements *stereoradiographic* methods have been used [93], like *roentgen stereophotogrammetric analysis* (RSA). It has been proven that RSA has the highest sensitivity and resolution (0.2 mm [102]) among these methods. However, RSA is difficult to perform and is time-consuming as well as costly [92], and hence is not widely used. Previous radiographic measurements were constrained to *migration* detection until recently a RSA approach to the dynamically inducible *micromotion* measurement was developed with a clinical precision of 0.3 mm [100].

X-ray methods have been applied in many investigations about prosthesis failure. Nevertheless, the disadvantages of limited resolutions and accuracy as well as harmful radiations produced during the testing have become noticeable. As a result, a new *in-vivo* measuring system, with high accuracy, high efficiency and low cost is required for implant movement detection, which is the eventual objective of this project. Although some systems have been reported in previous studies for biological signal detection [94, 95] and measurements of loading applied to bones or implants [96], so far there is no viable electrical method for *in-vivo* measurements of implant movement.

2.3 Conclusion

THA and TKA have benefited a large number of patients with hip disease since last century. Meanwhile, their long-term instability has been reported by many institutions and researchers over last two decades. *In-vitro* measurements are utilized in previous work to evaluate the stability of the implants in THA and TKA with the purpose of improving the implant design.

This project mainly concentrates on the design of an implantable electronic system for the evaluation of the prosthesis stability. The aims and objectives of the project are described in the next chapter.

3. Aim and Objectives

The aim of this project is to design an implantable sensor with the purpose of detecting the postoperative *micromotion* and *migration* of implants *in vivo* in applications of THA and TKA. This will benefit the evaluation and improvement of the implant design, and thus improve the survival rate and the long term stability of the implants. The requirements of this sensor system are:

1) It is an integrated electronic system in a size sufficiently small that it can be placed in the host bone cavity.
2) It must be a low-cost and low-power system.
3) The sensor will have a single degree of freedom for both *migration* and *micromotion* measurement in the axial direction (z) along the bone. Measurements for these two modes of movement must be independent.
4) Good linearity at the system output should be preserved over a wide range of *micromotion*, whose upper limit exceeds the experimentally established limit to avoid the formation of connective tissue at the bone-implant interface. The resolution of the *micromotion* measurement is required to be as small as 1 μm.
5) The detectable range for *migration* with this system should be no less than 2 mm. This was determined statistically from the results of the *migration* limit for failure in previous work, as shown in Section 2.2.1.1.
6) The sensor must have ability of self calibration. i.e. The calibration can be carried out in vivo after implantation of the system..
7) The system designed in this project must be compatible with a telemetry system which provides control as well as data transmission and a power supply as shown in Appendix F, although these aspects are not discussed.

4. System Configurations

The design of an implantable sensor is the main objective of this project. In this chapter the configuration and working function of the system are described.

4.1 Overview of the System

The system consists of an *RL* bridge as the essential part, with its input generated by a voltage controlled oscillator (VCO). A self-calibration subsystem is used for calibration and *migration* measurements by sending, receiving and recording control signals to and from the VCO and the bridge, with a preamplifier in connection with the bridge used for *micromotion* measurement. The block diagram of the whole system is shown in Fig 4.1. A description of each block is provided in the following sections.

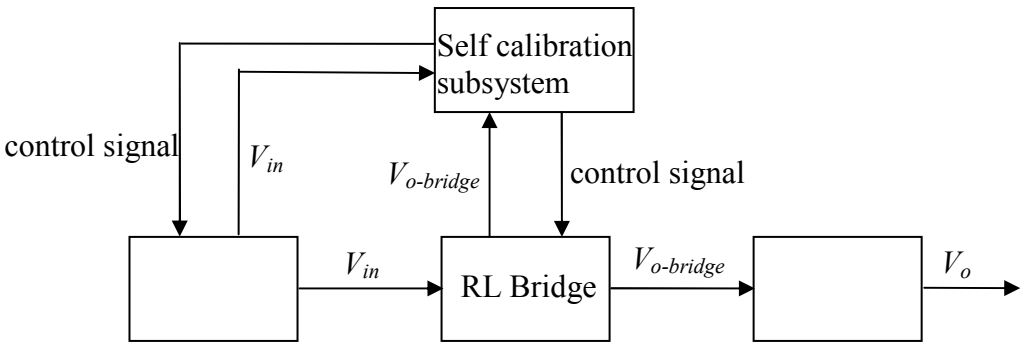

Fig 4.1 The block diagram for the whole system

4.2 *RL* Bridge – the Essential Part

The system is based on a modified form of *differential variable reluctance transducer* (DVRT). Fig 4.2 is the circuit schematic of the DVRT showing its connection to the

signal processing electronics, and Fig 4.3 shows typical dimensions for use in THA. The circuit consists of a pair of coaxial cylindrical coils L_1 and L_2, and two pairs of variable resistors R_1, R_2 and R_3, R_4 connected to form an *RL*-Wheatstone bridge. A short ferrite rod attached to the implant engages with the coils along their axis, while the coils themselves are attached to the bone. Thus the position of the implant can be recognized by recording the signal amplitude at the differential output of the bridge, which is modified by moving the rod inside the coils. The bridge is driven by a voltage controlled sinusoidal oscillator (VCO) of amplitude V_{in}, internal resistance r and frequency f. V_{in} was chosen to be about 100 mV and f about 100 kHz since these values can be conveniently generated by a CMOS VCO in integrated circuit form. In addition, this choice of operating frequency requires resistors of a few hundred ohms (which can be easily realised in integrated circuit form as either fixed or variable components) and inductors of about 1 mH which can be realised as cylindrical coils sufficiently small for implantation (operation at lower frequencies is also considered). The outputs of the bridge and the VCO are both required as inputs to the signal processing circuitry.

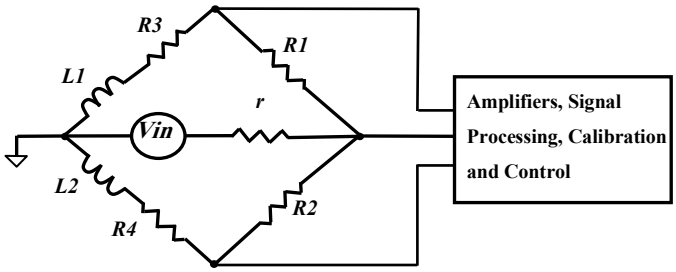

Fig 4.2 Circuit schematic showing the form of the DVRT and its connection to the signal processing electronics (the series resistances of the coils are not shown in the figure)

The experimental results reported in this project were obtained from a bench model with the dimensions of Fig 4.3. A photograph of the bench model is shown in Fig 5.1a. L_1 and L_2 each consisted of a 5-layer coil of 38 SWG insulated copper wire (about 400

turns in total) with a coupling coefficient k and series resistance r_L. The ferrite rod is a standard cylindrical component with a relative permeability (μ) of 48, resulting in a self-inductance of about 800 μH for each coil, a typical mutual inductance of about 165 μH and a series resistance of about 11Ω for each coil at 100 kHz.

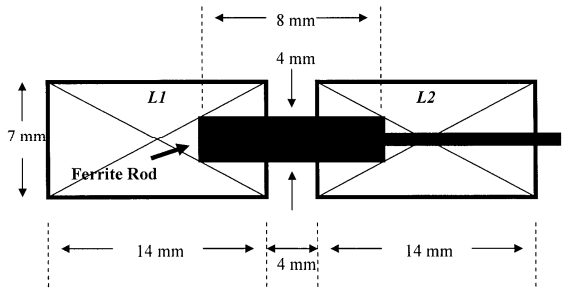

Fig 4.3 Approximate coil and ferrite rod dimensions for use in THA

Only the axial displacement is measured in this project. The impact of displacement in these two directions can be ignored, as 1 μm displacement in either of these two directions only causes a measurement error of 1 nm in the distal direction. Note that the inner diameter of the coil is 5 mm, so the range of movements in other two directions is less than 2.5 mm.

The signal processing employed in the bench experiments was very simple, consisting of a signal generator (for the VCO), an amplifier for the bridge output with a gain of about 300 and bandwidth about 200 kHz, and the outputs being read on an oscilloscope. The variable resistors were multi-turn components, which were adjusted manually according to the algorithm described below.

The transfer function of the bridge, $H_1(j\omega)$, is given by the following expression where ω is the angular frequency (= $2\pi f$; see Appendix A for the detailed derivation):

$$H_1(j\omega) = \frac{V_{o-bridge}(j\omega)}{V_{in}(j\omega)} = REAL + j.IMAG \tag{4.1}$$

where $V_{o\text{-}bridge}(j\omega)$ is the output voltage of the bridge (see Fig 4.2) and *REAL* and *IMAG* are functions of $R_{1\text{-}4}$, $L_{1,2}$, k and ω. If A_v is the voltage gain of the preamplifier, the overall transfer function of the system is:

$$H(j\omega) = A_v.H_1(j\omega) = A_v(REAL + j.IMAG) \tag{4.2}$$

Initially the system is set so that $R_1 = R_2$ and $R_3 = R_4$. If the rod is then placed at the geometrical centre of the coils so that $L_1 = L_2$ the bridge is balanced and the output voltage is zero since both the terms *REAL* and *IMAG* in eqn. (4.1) are zero. However, in practice it is impossible to achieve this level of balance due to mis-positioning of the ferrite rod as a result of imprecision in the surgical assembly and/or tolerances in the values of the inductors and other components. In consequence, it is impossible to determine either the static displacement (misalignment) of the core once the system has been implanted or its gross movement thereafter (*migration*), thus reducing the effectiveness of the DVRT in this application. However, these problems are solved by means of the *calibration* procedure described in Section 4.3.

4.3 Subsystem for Calibration and *Migration* Measurement

The calibration algorithm and its automated hardware implementation are described in this section.

4.3.1 Calibration Algorithm

As already noted, the key problem is orientating the ferrite rod precisely at the geometrical centre of the coils so that at rest the inductors L_1 and L_2 are equal and the bridge is balanced giving zero output. If, as is generally the case, such mechanical precision is not feasible, it is shown that it is possible to bring the output of the bridge close to zero by adjusting the electrical parameters of the system, specifically the frequency f and the values of the four resistors R_1, R_2, R_3, R_4. In practice, two of the resistors (say R_2, R_4) can be preset to fixed values, which simplifies the calibration process (the algorithm described below assumes this simplification). Suitable choices for these resistor values are discussed in Section 6.2.3 and Appendix D. Application of

the method will also absorb tolerances in the component values generally. Note that if four variable resistors are employed, greater precision is possible at the expense of a more complex algorithm and an increased number of iterations.

One complication of the calibration process is that both the real and imaginary parts of the transfer function $H_1(j\omega)$ of the bridge depend on R_1 and R_3 (eqn. (4.1)), which means any variations in the real or the imaginary parts, caused by R_1 or R_3, leads to changes in the other. Therefore, the adjustment of the real and imaginary parts must be repeated iteratively before the bridge is completely balanced, which raises the issue of *convergence* (see Appendix B). In practice, as described below, this is not a problem as the process converges to the required level of residual error after very few iterations.

Initially the system is set so that $R_1 = R_2$ and $R_3 = R_4$. To null the output to zero, with reference to eqn. (4.1) and the definition of terms given in the Appendix A, the following procedure was adopted (the flow chart for this procedure is shown in Fig 4.4):

1. Sweep the oscillator frequency until the phase angle of $H_1(j\omega)$ is 0° or 180º. This is the balance frequency of the system and sets the term *IMAG* in (1) to zero.
2. Adjust R_1 until the phase angle of $H_1(j\omega)$ is 90º or -90º. This sets the term *REAL* to zero.
3. Adjust R_3 until the phase angle of $H_1(j\omega)$ is 0° or 180º. This sets the term *IMAG* to zero.
4. Repeat steps 2 and 3 until the output is zero.

The calibration process is terminated when $|H_1(j\omega)| < 4.6 \times 10^{-5}$. The selection of the termination value for $|H_1(j\omega)|$ is discussed in Section 6.3.

In some cases, the calibration fails because the equations $REAL = 0$ or $IMAG = 0$ have no real solutions for R_1 and R_3. Conditions for successful calibration are discussed in Sections 6.2.1 and 6.2.2.

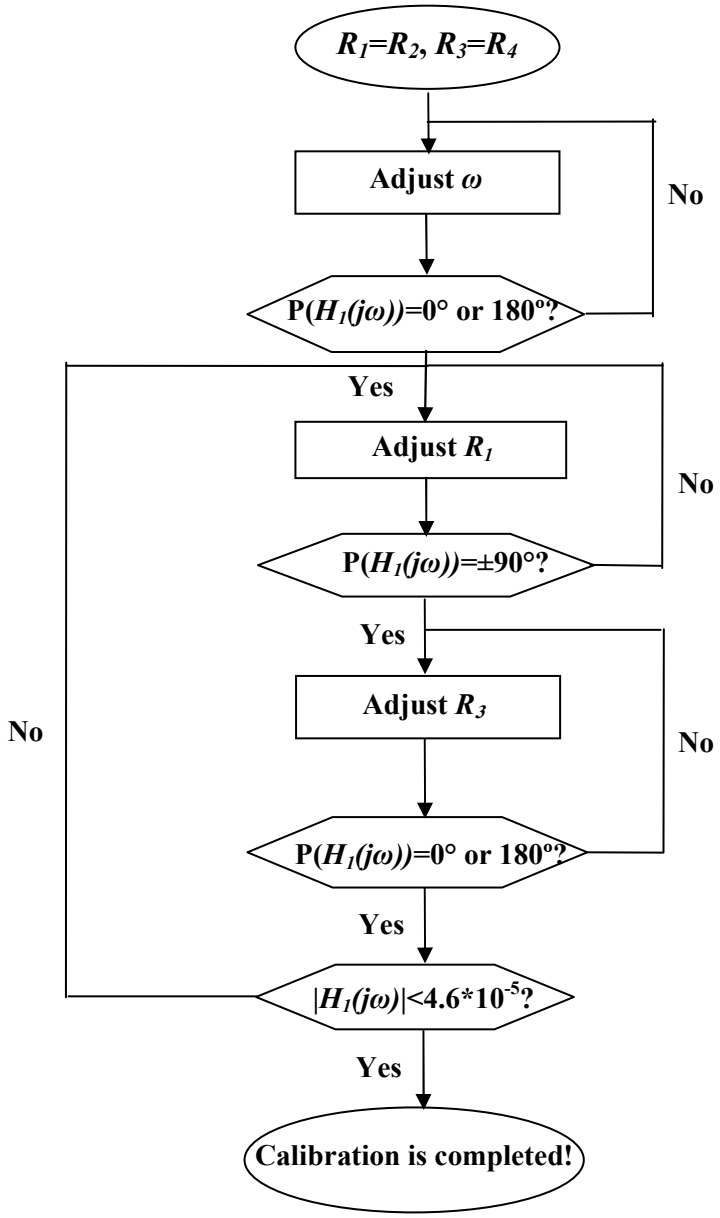

Fig 4.4 Flow chart for the calibration procedure advanced in Section 4.3.1

Once the calibration process is complete and the modified values of the resistors R_1', R_3' are known, the gross axial displacement (*migration*) of the implant since the last calibration phase can be calculated. A 1-to-1 mapping relationship between the values

of R_1', R_3' and the implant *migration* exists and hence the *migration* value can be conveniently found using a look-up table.

4.3.2 Automated Implementation

In this section the automatic hardware realization of the calibration procedure proposed in Section 4.3.1 is described, with the mechanism for each part of the self-calibration device detailed.

4.3.2.1 Overview

The nature of the calibration algorithm described in Section 4.3.1 and the simple adjustments which are required to implement it lends itself well to an automated realization using a microcontroller. This could be integrated with the rest of the electronics or alternatively kept separate and mounted on a small board.

The main circuits/subsystems (in addition to the microcontroller) required in the design are (i) a voltage controlled oscillator (VCO), (ii) a preamplifier, (iii) a phase detector, (iv) a phase *quadrature* detector and (v) two fixed resistors (total value is 500 Ω) and two variable resistors variable within the approximate range 100 Ω – 1 kΩ, all of which are detailed in Sections 4.3.2.2 to 4.3.2.4. The choice of the sum of the two fixed resistors values are explained in Appendix D. Measurements indicate that variations of the variable resistor values with a step of 0.1 Ω are sufficient to achieve residual transfer function amplitude of 2×10^{-5} after calibration. This resolution can be obtained using a 16-bit A/D converter, which would be inexpensive and readily available.

Test structures based on all the required subsystems have been fabricated, using 0.35 μm CMOS technology, and are in the process of being tested. So far, tests have been completed on the ±90° phase detector and the variable resistors. The outline block diagram of a possible automated version of the system is shown in Fig 4.5, with typical values of parameters shown in Table 4.1.

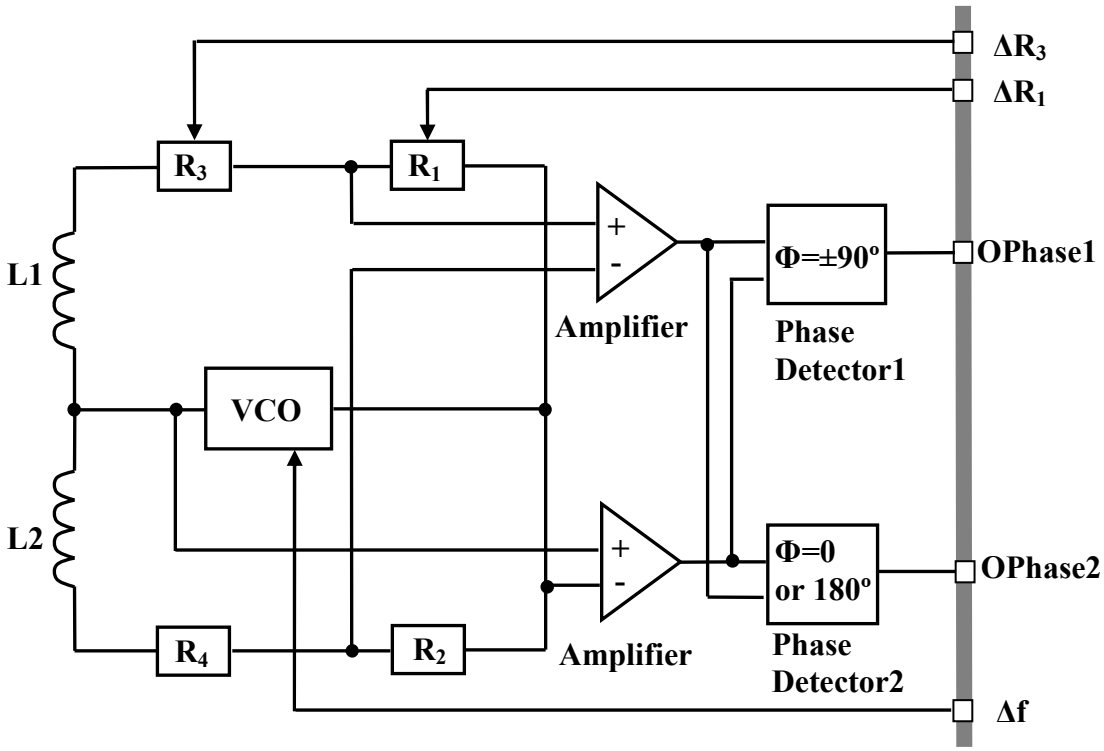

Fig 4.5 Proposed hardware realisation of the device. The component references correspond to Fig 4.2 while the connections to the right of the figure are the microcontroller inputs and outputs.

4.3.2.2 Variable Resistors

Fig 4.6a is the schematic diagram of the variable resistor, with its parameters shown in Table 4.2. As shown in Fig 4.6a, the integrated variable resistor involved in the automatic calibration process has been designed by using the linearity of an enhancement mode NMOS transistor. The I-V characteristics of a NMOS transistor given in eqn. (4.3) in the linear region and the saturation region respectively indicate that the drain current I_D is proportional to the drain-to-source voltage V_{DS} when $V_{DS} < V_{GS} - V_T$. Thus the device acts as a resistance whose value is determined by V_{GS}, with $V_{GS} > V_T$ and a small V_{DS} applied. Based on these properties, a variable resistor can be realised by operating an NMOS transistor in its ohmic region with an adjustable voltage V_{GS} controlling the resistance value, i.e. the slope of I-V curve as presented in eqn. (4.4). Note that a more sophisticated model describing the transistor characteristics is

used in Cadence simulation, which causes differences between the simulated results and the calculated results of the resistance value.

$$I_D = \begin{cases} \frac{K_N}{2}\frac{W}{L}[2(V_{GS}-V_T)V_{DS}-V_{DS}^2] & V_{DS} \le V_{GS}-V_T \\ \frac{K_N}{2}\frac{W}{L}(V_{GS}-V_T)^2 & V_{DS} \ge V_{GS}-V_T \end{cases} \quad [99] \tag{4.3}$$

$$R_{DS} = \begin{cases} \dfrac{1}{\frac{K_N}{2}\frac{W}{L}[2(V_{GS}-V_T)-V_{DS}]} & for \quad V_{DS} < V_{GS}-V_T \\ \dfrac{1}{K_N\frac{W}{L}(V_{GS}-V_T)} & for \quad V_{DS} << V_{GS}-V_T \end{cases} \tag{4.4}$$

where:

I_D = drain current

V_{DS} = drain-to-source voltage

V_{GS} = gate-to-source voltage

V_T = threshold voltage

W, L = width and length of the NMOS transistor

$K_N = \mu_n C_{ox}$

μ_n = electron channel mobility

C_{ox} = gate capacitance per unit area

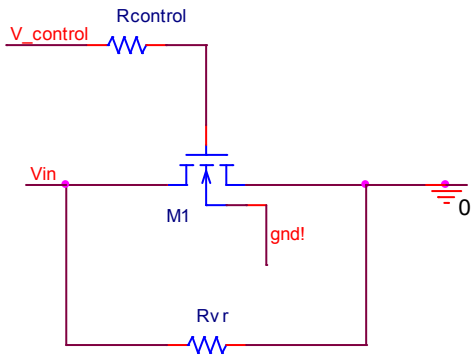

Fig 4.6a Schematic diagram for the variable resistor

From the simulation results shown in Table 5.1, the variable resistor is expected to operate in the range of 100 Ω to 1 kΩ. Provided that V_{GS} is below 1.5 V, V_T is approximately 0.7-0.8 V, the W/L is set to be 1000 in our design to ensure that the resistance of the NMOS transistor is about 10 Ω when V_{GS} = 1.5 V (in simulation). A 1 kΩ resistor is connected in parallel with the NMOS transistor as shown in Fig 4.6a, to give a maximum value for the total resistance of about 1 kΩ. One thing should be noted that the drain and the source of the NMOS transistor are both connected to the corresponding pins via a pad (the schematic diagram is shown in Fig 4.6b) with resistance of 62 Ω, which then produces a total resistance of 124 Ω in series with the NMOS transistor. Therefore, the maximum and minimum values of the packaged variable resistor are approximately 1100 Ω and 130 Ω.

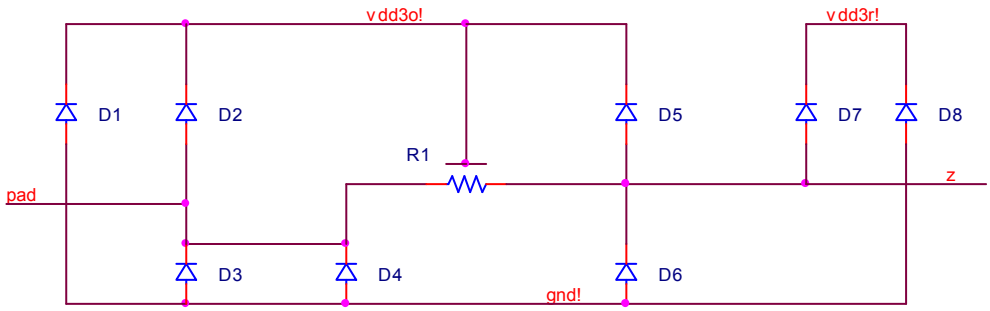

Fig 4.6b Schematic diagram for the pad. R_1 = 50 Ω. Nets named gnd!, vdd3o! and vdd3r! are the power nets. The port 'pad' is connected to the pin and 'z' to the variable resistor.

The expression of the total resistance can be written as:

$$R_{total} = \frac{1000 R_{DS}}{R_{DS} + 1000} + 2R_{pad} \qquad (4.5)$$

where R_{DS} is defined in eqn. (4.4), and R_{pad} is the resistance of the pad.

4.3.2.3 Preamplifier

According the properties of the ±90º phase detector presented in Section 4.3.2.4, a nonlinear or automatic gain-control (AGC) amplifier is required as a preamplifier, whose gain reduces with increasing input voltage, for proper operation of the following phase detectors. However, a common amplifier is used for both *migration* and *micromotion* measurements in this project as the calibration of the bridge has been carried out manually in our tests so far. The configuration of this amplifier is specified in Section 4.4.1. The properties of the AGC preamplifier are discussed in Section 6.2.2.

4.3.2.4 Phase Detector

The schematic and block diagram of the ± 90° phase detector realized with 0.35 μm process is shown in Figs 4.7-4.11, with relative parameter values shown in Tables 4.3 to 4.6. As shown in Fig 4.7, the detector consists of two channels with identical structure except for a capacitor C_p applied to produce 90° phase shift in one channel, and a resistor R_p applied to produce 0° phase shift in the other. Amplifiers and inverters are connected to both channels to convert the sine wave signals to square wave. Finally a D-type flip flop is connected to the output of both channels, with the data input connected to the capacitor channel and the clock input connected to the resistor channel. The D flip flop is an electronic circuit having two stable states as its output always follows the state of the data input at the moment of a rising clock edge. Therefore, the output remains a low level when the phase difference between the inputs of two channels is between -90º and 90º, and a high level when the phase difference between the two inputs is between -180 º and -90 º or between 90 º and 180 º. As a result, the ±90° phase difference at the inputs can be detected by means of level transition at the output of the flip flop.

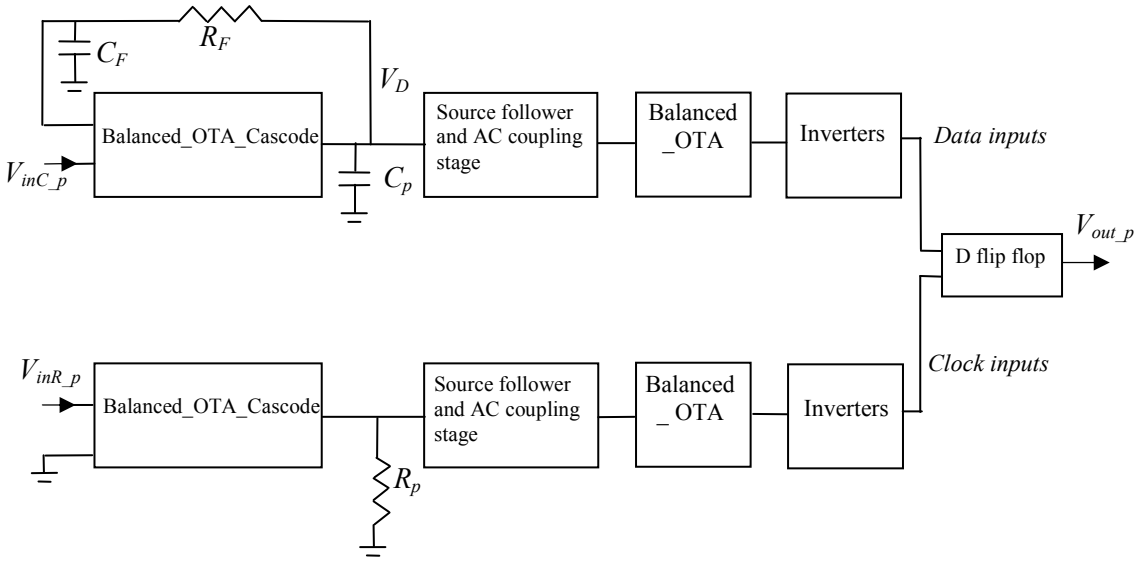

Fig 4.7 Block diagram of the ±90° phase detector realized in 0.35 μm technology. R_F and C_F constitute a feedback system for signal stabilization in the capacitor channel. V_{inR_p} and V_{inC_p} are both sine wave signals. The DC supply is ± 1.5 V. The total power is approximate 0.45 mW. Circuit schematics for each block are shown in Figs 4.8-4.11.

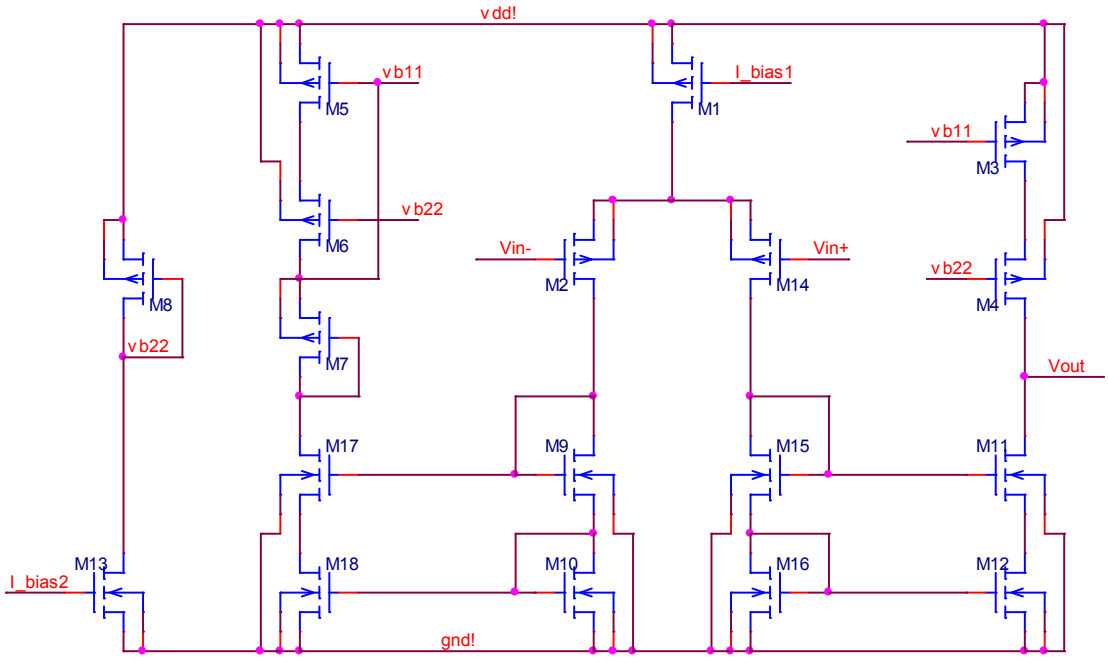

Fig 4.8 Schematic diagram of Balanced_OTA_Cascode. $I_{bias1} = I_{bias2} = 10$ μA.

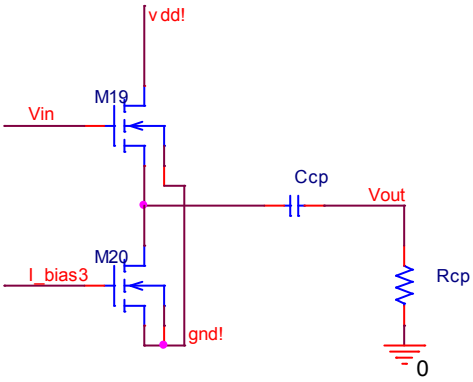

Fig 4.9 Schematic diagram of Follower-Coupling. I_{bias3} = 10 µA.

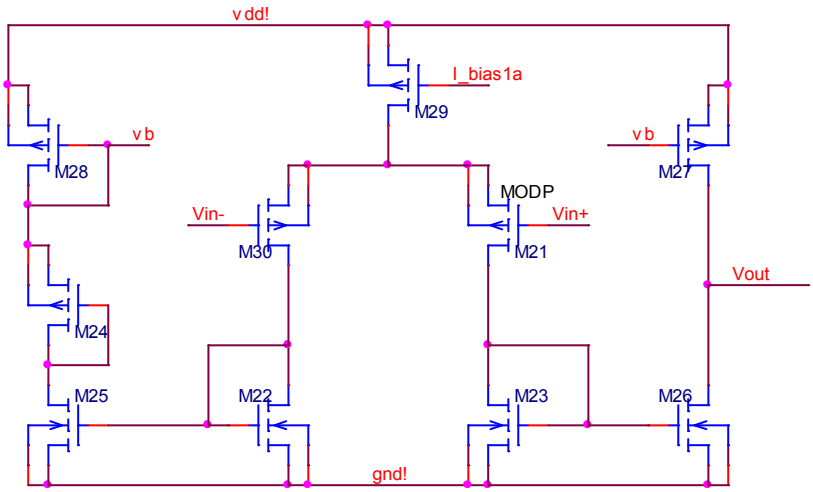

Fig 4.10 Schematic diagram of Balanced_OTA. I_{bias1a} = 10 µA.

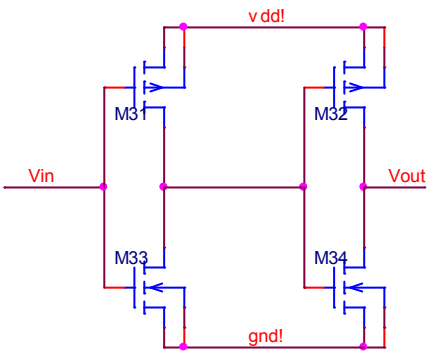

Fig 4.11 Schematic diagram of Inverters

The value of the capacitor C_p has been chosen to ensure that the output signal levels are equal, with the same signal amplitude at the inputs to both channels at 100 kHz, as shown in eqn. (4.6):

$$|V_{inC\_p} \cdot g_{mp} \cdot \frac{1}{j\omega C_p}| = |V_{inR\_p} \cdot g_{mp} \cdot R_p| \quad \Rightarrow \quad C_p = \frac{1}{\omega R_p} \tag{4.6}$$

where:

V_{inC_p} and V_{inR_p} = input voltages to the capacitor channel and the resistor channel

g_{mp} = transconductance of the balanced-OTA-cascode

C_p = capacitance connected to the output of the balanced-OTA-cascade in the capacitor channel

R_p = resistance connected to the output of the balanced-OTA-cascade in the resistor channel.

In our tests the capacitance is set to 15 pf and the resistance to 100 kΩ.

Additionally, an extra RC feedback circuit has been applied to the capacitor channel, to stabilize the DC conditions. Value settings for R_F and C_F are shown as below.

As shown in Fig 4.7, the transfer function of the balanced_OTA_cascode in the capacitor channel is:

$$H(j\omega) = \frac{V_D}{V_{inC\_p}} = \frac{G(1 + j\omega C_F R_F)}{j\omega C_p (1 + j\omega C_F R_F) + j\omega C_F + G} \tag{4.7}$$

where:

V_D = output voltage of the balanced_OTA_cascode in the capacitor channel

G = transconductance of the balanced_OTA_cascode

R_F and C_F = resistance and capacitance in the feedback circuit.

For $C_F R_F \rightarrow \infty$, $H(j\omega) \rightarrow G / j\omega C_p$, and the phase shift is about 90º. As a result, R_F and C_F must be large enough to provide a 90º phase shift at the capacitor channel, at f = 100 kHz with C_p = 15 pf and R_p = 100 kΩ. For this, the following conditions are required:

$$\begin{aligned} &\text{(a) } \omega C_F R_F >> 1; \\ &\text{(b) } \omega^2 C_p C_F R_F >> \omega(C_p + C_F); \\ &\text{(c) } \omega C_F R_F >> G \qquad \text{at } f = 100 \text{ kHz} \end{aligned} \tag{4.8}$$

As C_p = 15 pf, R_p = 100 kΩ and G = 40 μA/V, conditions in (4.8) can be satisfied when R_F = 10 MΩ and C_F = 1 μF at f = 100 kHz.

The 0° phase detector is comprised of a D-type flip flop connected to two identical resistor channels whose configurations are the same as in ±90° phase detector.

It should be noted that the phase detection process is very sensitive to changes in the waveform or period of the signals. As a result, there are minimum and maximum allowable input signal magnitudes needed to drive the phase detector properly; otherwise errors in the phase detection may occur. If the input signal level is too small, errors may occur due to the changes in the duty cycles of the signals to the inputs of the flip flop which is connected to the inverters, as the switching point of the inverters is approximately 10 mV. On the other hand, if the input signal level is too large, distortion may occur at the output of the Balanced_OTA_Cascode due to the finite supply levels, which will cause phase errors. Based on the simulation results, the phase detection errors increase significantly when the input signal amplitude is less than 1 mV or more than 150 mV. Such limitation will raise a requirement of a nonlinear or AGC preamplifier preceding the phase detector to generate signals with the amplitudes in a proper range. Such preamplifier is detailed in Section 6.2.2.

In addition, ± 90° phase detector realized with 0.8 µm technology is also designed and tested in this project. The 0.8 µm detector has the same structure as the 0.35 µm detector, except for the Balanced_OTA_Cascode. The schematic diagram and relative parameters of the Balanced_OTA_Cascode are shown in Fig 4.12 and Table 4.7. The phase detection errors increase significantly when the input signal amplitude is less than 20 mV or more than 120 mV, according to simulation.

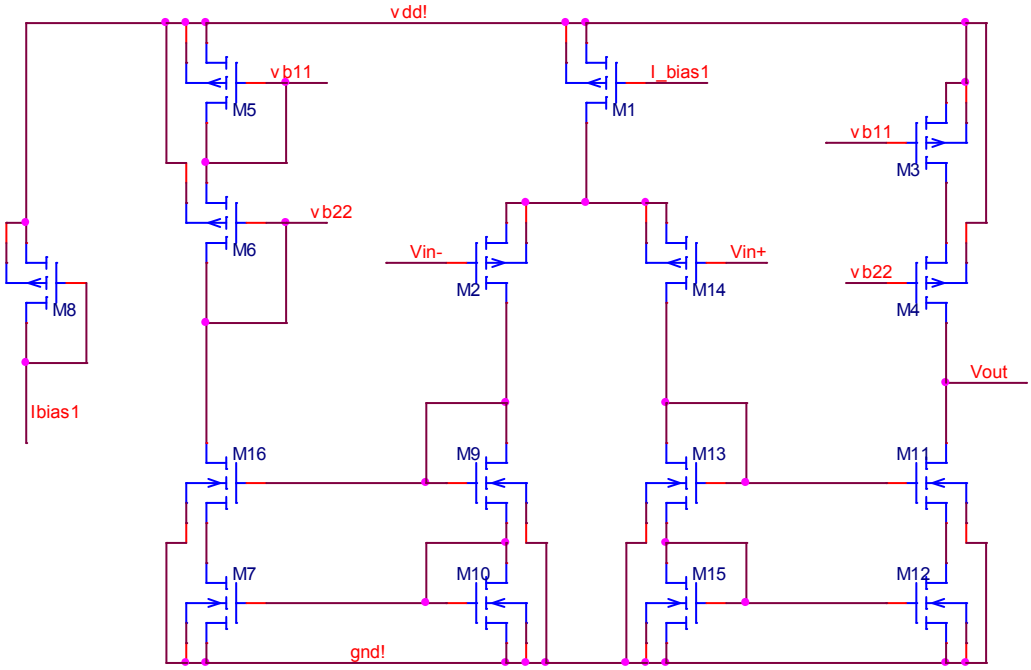

Fig 4.12 Schematic diagram of Balanced_OTA_Cascode in 0.8 µm phase detector. I_{bias1} = 10 µA.

4.4 Subsystem for *Micromotion* Measurement

In this section the mechanism and output functions of the subsequent amplifier, which is connected to the *RL* bridge for *micromotion* measurement, are described.

4.4.1 Amplifier

The block diagram of the amplifier used for *micromotion* testing is shown in Fig 4.13, which is a combination of an operational transconductance amplifier (OTA) and an operational amplifier (OPA), connected together via an AC coupling. The whole amplifier is realized using 0.35 CMOS technology, as shown in Figs 4.14 and 4.15 respectively. The relevant parameter values are listed in Tables 4.8 and 4.9. The total power of the amplifier is approximate 0.69 mW.

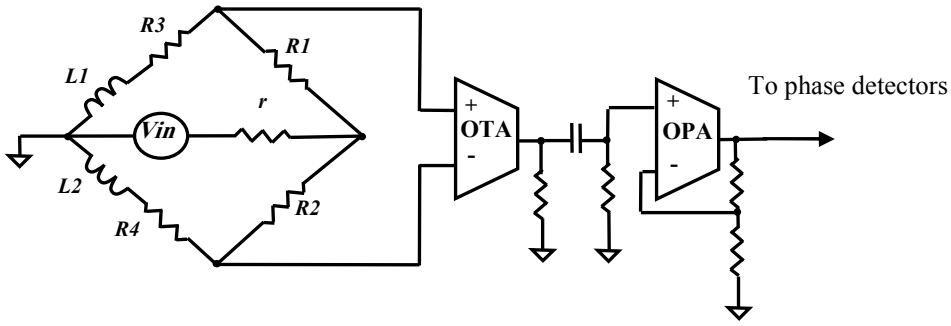

Fig 4.13 The block diagram of the amplifier used for micromotion testing.

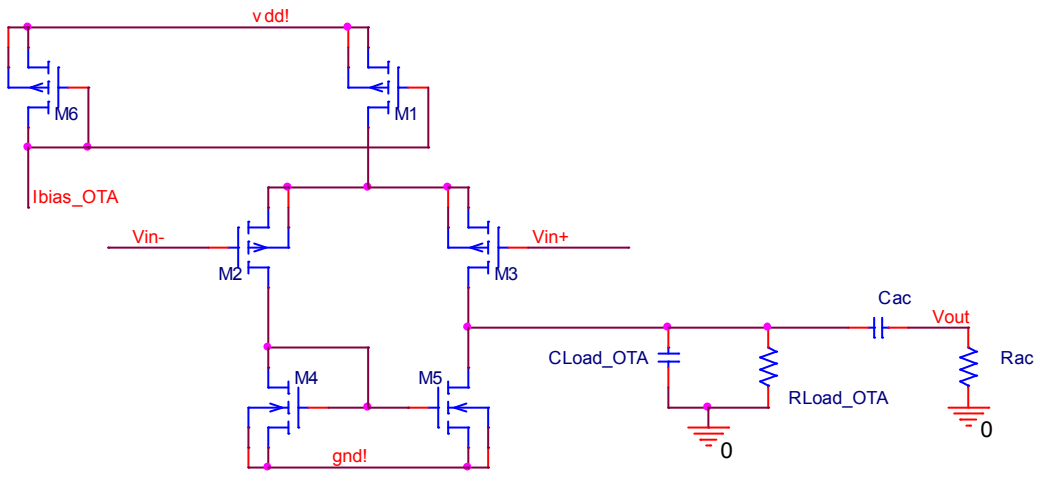

Fig 4.14 Schematic diagram of OTA (Operational Transconductance Amplifier). $I_{bias\_OTA} = 84\ \mu A$.

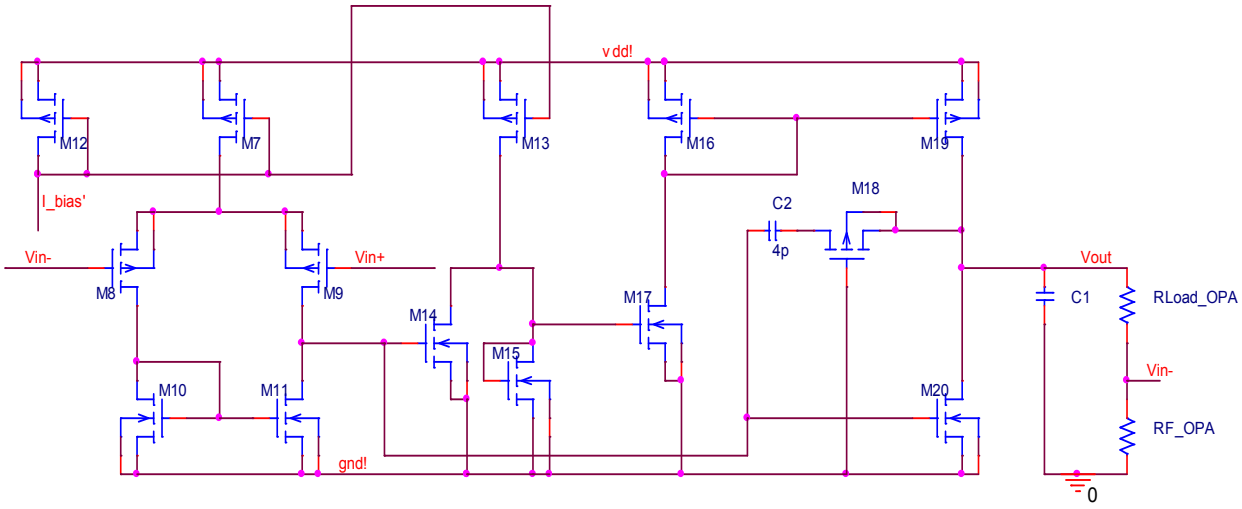

Fig 4.15 Schematic diagram of OPA (Operational Amplifier). $I_{bias\_OPA} = 10\ \mu A$.

The voltage gain of the OTA together with the AC coupling circuit can be written as:

$$A_{v\_OTA} = \sqrt{K_p \frac{W}{L} I_{bias\_OTA}} \cdot z_L \tag{4.9}$$

where:

z_L = the load impedance of the OTA in association with the AC coupling circuit

$$= \frac{\omega C_1 R_{Load\_OTA} R_{ac}}{X}$$

$$X = [(1 - \omega^2 R_{Load\_OTA} R_{ac} C_{Load\_OTA} C_{ac})^2 + \omega^2 (R_{Laod\_OTA} C_{ac} + R_{Load\_OTA} C_{Load\_OTA} + R_{ac} C_{Load\_OTA})^2]^{\frac{1}{2}} \quad (4.9a)$$

ω = the operating angular frequency

R_{Load_OTA}, R_{ac}, C_{Load_OTA} and C_{ac} = the load resistance and capacitance of OTA defined in Fig 4.12

W, L = width and length of the PMOS transistor

$K_P = \mu_n C_{ox}$

μ_n = electron channel mobility

C_{ox} = gate capacitance per unit area

I_{bias_OTA} = the bias current for OTA

Note: The eqn (4.9a) comes from a combination of the loads and the AC filter in Fig 4.14.

The voltage gain of the OPA can be written as:

$$A_{v\_OPA} = \frac{R_{Load\_OPA}}{R_{F\_OPA}} + 1 \quad (4.10)$$

where R_{Load_OPA} is the load resistance of the OPA and R_{F_OPA} is the feedback resistance of the OPA.

Based on eqns. (4.9) and (4.10), the total voltage gain of the preamplifier is:

$$A_v = A_{v\_OTA} \cdot A_{v\_OPA} \quad (4.11)$$

The values of the parameters in eqns. (4.9) and (4.10) are illustrated in Tables 4.8 and 4.9, and are calculated to produce an overall gain A_v of about 345 for the preamplifier.

This is sufficient for *micromotion* testing, given the component tolerances and environmental effects. The choice of the voltage gain is detailed in Section 6.3.

It should be noted that the amplifier is a band-pass circuit, as R_{load_OTA} and C_{load_OTA} (Fig 4.14) constitute a high-pass filter while OTA, OPA and AC coupling between OTA and OPA are all low-pass circuits.

The 3dB frequency of the low-pass RC filter (composed of R_{load_OTA} and C_{load_OTA}) is:

$$f_{H\_RC} = \frac{1}{2\pi R_{Load\_OTA} C_{load\_OTA}} \tag{4.12}$$

The 3dB frequency of OTA is [99]:

$$f_{H\_OTA} = \frac{1}{2\pi R_S [C_{gs} + C_{gd}(1 + g_{m\_OTA} R_{load\_OTA} + \frac{R_{load\_OTA}}{R_S})]} \tag{4.13}$$

where:

R_S = source resistance
C_{gs}, C_{gd} = gate-source capacitance and gate-drain capacitance
g_{m_OTA} = transconductance of OTA

The 3dB frequency of OPA is [99]:

$$f_{H\_OPA} = (1 + a_0 \frac{R_{F\_OPA}}{R_{load\_OPA} + R_{F\_OPA}}) \mid p_1 \mid \tag{4.14}$$

where:

a_0 = low-frequency gain of the basic amplifier
p_1 = basic-amplifier pole in radians per second

The 3dB frequency of AC coupling (composed of R_{ac} and C_{ac}) circuit is:

$$f_{L\_AC} = \frac{1}{2\pi R_{ac} C_{ac}} \tag{4.15}$$

With the parameters list in Tables 4.8 and 4.9, the bandwidth of the amplifier is 5 kHz to 150 kHz, as shown in simulations. It can be improved by increasing the bias current of OPA (I_{bias_OPA}) or reducing the load resistance of OTA and OPA (R_{Load_OTA} and R_{Load_OPA}) at the expense of reducing the total voltage gain (A_v).

However, due to the modeling problems, the measured bandwidth is much less than simulation results. It is detailed in Section 5.3.1.

4.4.2 Output Analysis of the System

After calibration, the new values of R_1, R_3 are R_1', R_3' respectively, and hence the new values of *REAL* and *IMAG* defined in eqn. (4.1) are *REAL*' and *IMAG*'. A key assumption in the theory which follows is that variations of L_1, L_2 and M caused by small axial displacements, z, of the rod can be represented by the following set of linear equations (This assumption is validated in Figs 5.2a and 5.2b):

$$\begin{aligned} L_1' &= L_1 + m_1 z \\ L_2' &= L_2 - m_2 z \\ M' &= M - m_3 z \end{aligned} \tag{4.16}$$

where m_1, m_2 and m_3 are all constants. Substituting eqn. (4.16) into eqn. (4.2) and differentiating with respect to z:

$$\frac{\partial V_o}{\partial z} = A_v V_{in} \left(\frac{\partial REAL'}{\partial z} + j \frac{\partial IMAG'}{\partial z} \right) \tag{4.17}$$

where $\partial REAL'/\partial z$ and $\partial IMAG'/\partial z$ are functions of $R_{1,3}'$, $R_{2,4}$, $L_{1,2}$, k, $m_{1,2,3}$ and ω, which are constants after calibration is complete. The derivation process is shown in Appendix C. Eqn. (4.17) can also be written in polar form:

$$\frac{\partial V_o}{\partial z} = A_v V_{in} \left\{ \sqrt{\left(\frac{\partial REAL'}{\partial z} \right)^2 + \left(\frac{\partial IMAG'}{\partial z} \right)^2} \right\} . e^{j\theta} \tag{4.18}$$

where $\theta = arg(\partial Vo/\partial z)$.

From eqn. (4.18), it is apparent that V_o, the output voltage of the system, is proportional to the rod displacement z if eqn. (4.16) is valid and A_V is constant, i.e., if a small-signal analysis can be applied (the validity of these two assumptions have been tested experimentally and are discussed in Sections 5.2.1 and 5.3.1). This allows the

micromotion of the rod to be predicted from changes in the observed output voltage V_o and the output gradient (see eqns. 4.17 and 4.18).

Tables in this chapter

Parameter		Value
R_1, R_3		100 Ω ~ 1 kΩ
R_2, R_4		400Ω,100 Ω
L_1, L_2		800 μH
Coupling coefficient k		0.2
Amplifier	central frequency	100 kHz
	3 dB bandwidth	> 100 kHz
VCO	tunable frequency range	50 kHz ~ 200 kHz
	output amplitude	0.1~0.3 V peak
	THD	<10%

Table 4.1 Typical values of parameters of the system shown in Fig 4.5.

Parameter	$R_{control}$	R_{vr}	W_{M1}	L_{M1}
Value	1 kΩ	1 kΩ	1000 μm	1 μm

Table 4.2 Parameter values of variable resistor shown in Fig 4.6a.

Parameter	W_{M1}	L_{M1}	W_{M2}	L_{M2}	W_{M3}	L_{M3}
Value (μm)	20	2	20	5	20	2
Parameter	W_{M4}	L_{M4}	W_{M5}	L_{M5}	W_{M6}	L_{M6}
Value (μm)	20	2	20	2	20	2
Parameter	W_{M7}	L_{M7}	W_{M8}	L_{M8}	W_{M9}	L_{M9}
Value (μm)	50	2	20	2	10	2
Parameter	W_{M10}	L_{M10}	W_{M11}	L_{M11}	W_{M12}	L_{M12}
Value (μm)	10	2	10	2	10	2
Parameter	W_{M13}	L_{M13}	W_{M14}	L_{M14}	W_{M15}	L_{M15}
Value (μm)	10	2	20	5	10	2
Parameter	W_{M16}	L_{M16}	W_{M17}	L_{M17}	W_{M18}	L_{M18}
Value (μm)	10	2	10	2	10	2

Table 4.3 Parameter values Balanced_OTA_Cascode shown in Fig 4.8.

Parameter	W_{M19}	L_{M19}	W_{M20}	L_{M20}	R_{cp}	C_{cp}
Value	10 µm	2 µm	10 µm	2 µm	100 kΩ	10 pF

Table 4.4 Parameter values of Follower-Coupling shown in Fig 4.9.

Parameter	W_{M21}	L_{M21}	W_{M22}	L_{M22}	W_{M23}
Value (µm)	200	5	5	5	5
Parameter	L_{M23}	W_{M24}	L_{M24}	W_{M25}	L_{M25}
Value (µm)	5	20	2	5	5
Parameter	W_{M26}	L_{M26}	W_{M27}	L_{M27}	W_{M28}
Value (µm)	5	5	20	2	20
Parameter	L_{M28}	W_{M29}	L_{M29}	W_{M30}	L_{M30}
Value (µm)	2	20	2	200	5

Table 4.5 Parameter values of Balanced_OTA shown in Fig 4.10.

Parameter	W_{M31}	L_{M31}	W_{M32}	L_{M32}
Value (µm)	8	2	8	2
Parameter	W_{M33}	L_{M33}	W_{M34}	L_{M34}
Value (µm)	2	2	2	2

Table 4.6 Parameter values of inverter shown in Fig 4.11.

Parameter	W_{M1}	L_{M1}	W_{M2}	L_{M2}	W_{M3}	L_{M3}
Value (µm)	20	2	20	2	20	2
Parameter	W_{M4}	L_{M4}	W_{M5}	L_{M5}	W_{M6}	L_{M6}
Value (µm)	20	2	20	2	20	2
Parameter	W_{M7}	L_{M7}	W_{M8}	L_{M8}	W_{M9}	L_{M9}
Value (µm)	10	2	20	2	10	2
Parameter	W_{M10}	L_{M10}	W_{M11}	L_{M11}	W_{M12}	L_{M12}
Value (µm)	10	2	10	2	10	2
Parameter	W_{M13}	L_{M13}	W_{M14}	L_{M14}	W_{M15}	L_{M15}
Value (µm)	10	2	20	2	10	2
Parameter	W_{M16}	L_{M16}				
Value (µm)	10	2				

Table 4.7 Parameter values Balanced_OTA_Cascode shown in Fig 4.12.

Parameter	W_{M1}	L_{M1}	W_{M2}	L_{M2}
Value (μm)	20	2	200	5
Parameter	W_{M3}	L_{M3}	W_{M4}	L_{M4}
Value (μm)	200	5	5	5
Parameter	W_{M5}	L_{M5}	W_{M6}	L_{M6}
Value (μm)	5	5	20	2
Parameter	R_{Load_OTA}	C_{Load_OTA}	R_{ac}	C_{ac}
Value	100 kΩ	2 pF	100 kΩ	150 pF

Table 4.8 Parameter values of OTA shown in Fig 4.14.

Parameter	W_{M7}	L_{M7}	W_{M8}	L_{M8}
Value (μm)	20	2	200	5
Parameter	W_{M9}	L_{M9}	W_{M10}	L_{M10}
Value (μm)	200	5	5	5
Parameter	W_{M11}	L_{M11}	W_{M12}	L_{M12}
Value (μm)	5	5	20	2
Parameter	W_{M13}	L_{M13}	W_{M14}	L_{M14}
Value (μm)	20	2	5	5
Parameter	W_{M15}	L_{M15}	W_{M16}	L_{M16}
Value (μm)	5	5	10	5
Parameter	W_{M17}	L_{M17}	W_{M18}	L_{M18}
Value (μm)	5	5	10	2
Parameter	W_{M19}	L_{M19}	W_{M20}	L_{M20}
Value (μm)	45	5	5	5
Parameter	R_{Load_OPA}	R_{F_OPA}	C_1	C_2
Value	11.5 kΩ	500 Ω	10 pF	4 pF

Table 4.9 Parameter values of OPA shown in Fig 4.15.

5. System Implementation and Results

This chapter describes the system implementation and experimental results of the bench tests carried out on the system.

5.1 System Implementation

There are two points that should be noted: a) although the system is intended ultimately for *in vivo* applications, all the tests described have been carried out *in vitro* (outside the body); b) as the system design is not yet complete, the calibration described in this project was carried out manually. The other sections of the self-calibration system, i.e. the variable resistors and the phase detectors were tested separately; c) the circuits were realized in 0.35 μm CMOS technology.

In our tests, the calibration, *migration* and *micromotion* measurements were undertaken using a common system. The system photograph is shown in Fig 5.1a. Two integrated circuits containing the phase detector and variable resistors described in Section 4.3 and an amplifier described in Section 4.4 were also employed for measurements, and their photographs are shown in Figs 5.1b and 5.1c. As shown in Fig 5.1a, a high precision micrometer head, with an accuracy of 1 μm was used in our tests for adjustments and measurements for both *migration* and *micromotion*. The micrometer head is combined with the pair of co-axial cylindrical coils forming the bridge by means of a nylon holder mounted on a steel base. The ferrite rod is connected to the micrometer gauge to monitor its displacement. The coil pair is connected to four manually-adjustable potentiometers to form a DVRT bridge, which is then connected to an amplifier system. The four potentiometers are multi-turn units variable between 0 and 1 kΩ.

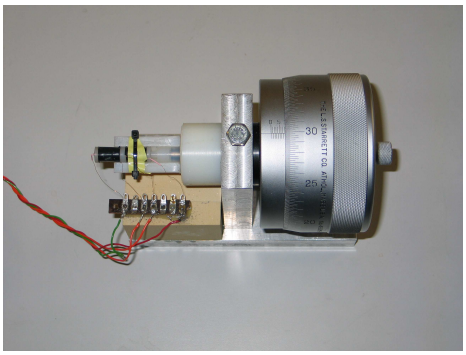

Fig 5.1a Arrangement for bench-testing. The co-axial bridge coils (scaled for *total hip arthroplasty* (THA); cf Figs 2.1a, 4.2 and 4.3) are on the left of the picture and the ferrite rod is connected to the micrometer gauge on the right. The limiting resolution of this micrometer is 1 μm. The dimension of the system is 15 mm × 12 mm × 10 mm.

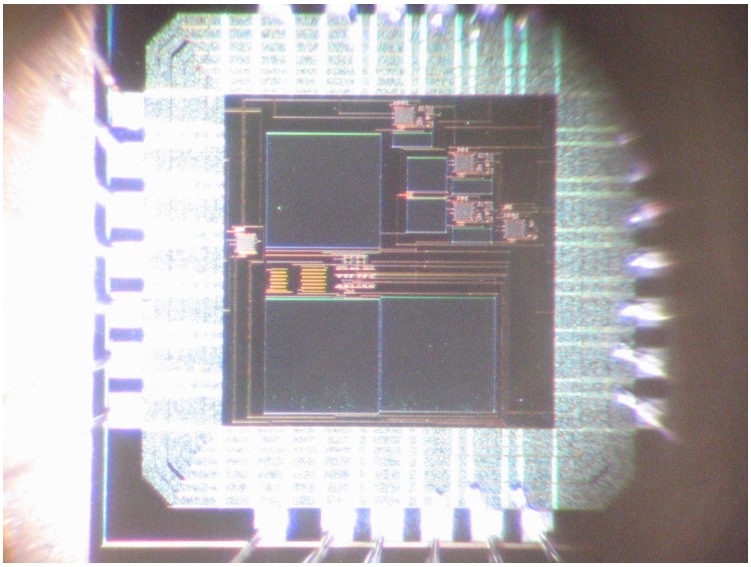

Fig 5.1b Photograph of the OTA-OPA chip; the schematic diagrams are shown in Figs 4.14 and 4.15. The area of the chip is 2.8 mm^2.

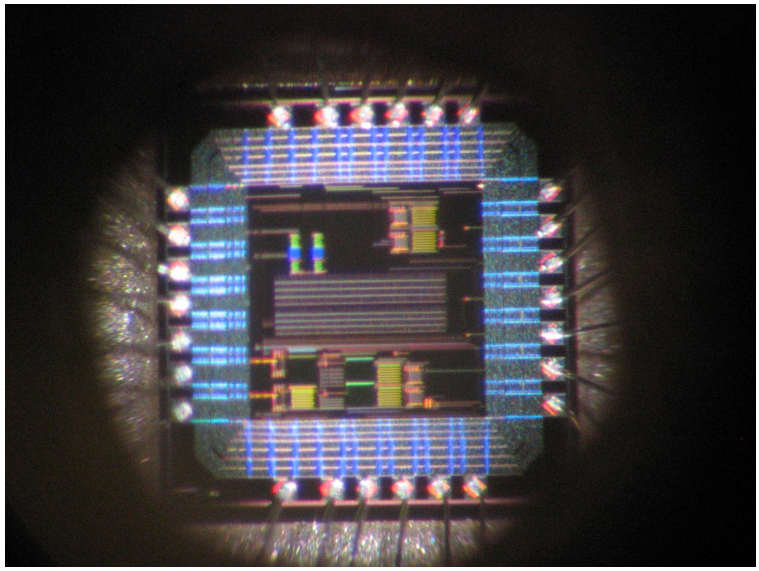

Fig 5.1c Photograph of the phase detector and variable resistors chip; the block and schematic diagrams are shown in Figs 4.6 - 4.11. The area of the chip is 2.8 mm^2.

The total gain of the amplifier is about 420 with a bandwidth of 120 kHz. A sine wave signal with 0.1 V amplitude and frequency of 100 kHz is applied to the input of the system and the output is monitored using an oscilloscope. The coil inductance and potentiometer values were measured using a high precision LCR meter with an accuracy of about 0.05%. The DC voltage supply for the system is ± 1.5 V.

5.2 Simulated and Measured Results for *Migration* Testing

Simulated and measured results for *migration* testing, including the coil inductance, large axial displacements (*migration*) of the rod and the characteristics of the variable resistors and the phase detectors are described in this section. The simulation tools used for the system design and algorithm modeling are Cadence and Matlab respectively.

5.2.1 Measured Results for Coil Inductance and Resistance at 100 kHz

Fig 5.2a and Fig 5.2b show the measured variation of self inductance and mutual inductance of the coils for small displacements of the rod (corresponding to *micromotion*). It is clear that a linear relationship between inductance L_1, L_2, M and displacement is preserved over a range of -500 µm to 500 µm even with initial gross

displacements of the rod (*migration*; 0 to 4 mm in Fig 5.2a and 5.2b). This validates the key assumption expressed by equation (4.9), allowing a linearised *small-signal* model to be employed to predict *micromotion* in a range of about ± 500 µm. Starting with the data in Figs 5.2a and 5.2b, curve fitting is used to determine the parameters of eqn. (5.1) (inductance values in µH) as a function of gross displacement, *D*:

$$
\begin{Bmatrix}
L_1^{'} = 762.69 + 0.0765z \\
L_2^{'} = 755.21 - 0.0712z \\
M = \begin{cases} 163.34 + 0.0009z & z \le 0 \\ 163.48 - 0.0026z & z > 0 \end{cases}
\end{Bmatrix} @\, D = 0
$$

$$
\begin{Bmatrix}
L_1^{'} = 845.25. + 0.0868z \\
L_2^{'} = 689.97 - 0.0581z \\
M = 159.77 - 0.0066z
\end{Bmatrix} @\, D = 1mm
$$

$$
\begin{Bmatrix}
L_1^{'} = 935.66 + 0.0943z \\
L_2^{'} = 639.08 - 0.0446z \\
M = 150.88 - 0.0115z
\end{Bmatrix} @\, D = 2mm
$$

$$
\begin{Bmatrix}
L_1^{'} = 1032.1 + 0.0975z \\
L_2^{'} = 601.12 - 0.0314z \\
M = 137.6 - 0.0148z
\end{Bmatrix} @\, D = 3mm
$$

$$
\begin{Bmatrix}
L_1^{'} = 1129.2 + 0.0952z \\
L_2^{'} = 575.39 - 0.0201z \\
M = 122.15 - 0.0159z
\end{Bmatrix} @\, D = 4mm
$$

(5.1)

Note: 1) M can be considered as a constant when D = 0; 2) All the data were collected at f = 100 kHz.

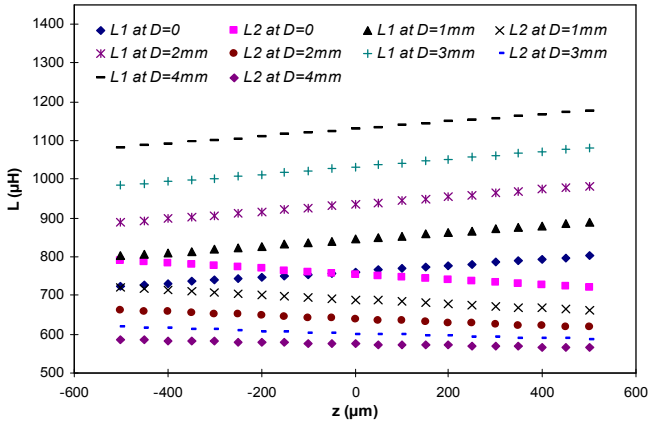

Fig 5.2a Coil self-inductance. Measured values of L_1, L_2 as a function of small axial displacements (*micromotion*) for five different values of initial position D (0,1,2,3,4 mm).

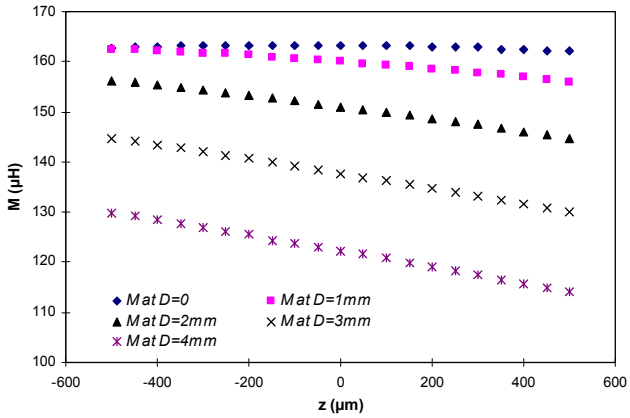

Fig 5.2b Mutual inductance between L_1, L_2 as a function of small axial displacements (*micromotion*) for five different values of the rod initial position D (0,1,2,3,4 mm).

As shown in eqn (5.1), the sensitivities of L_1, L_2 and M are: 76.5 µH/mm, 71.2 µH/mm and approximately 1 µH/mm at D = 0; 86.8 µH/mm, 56.1 µH/mm and 6.6 µH/mm at D =1 mm; 94.3 µH/mm, 44.6 µH/mm and 11.5 µH/mm at D = 2 mm; 97.5 µH/mm, 31.4 µH/mm and 14.8 µH/mm at D = 3 mm; 95.2 µH/mm, 20.1 µH/mm and 15.9 µH/mm at D = 4 mm, respectively.

The self resistance of the coils L_1 and L_2 (r_{L1}, r_{L2}) at 100 kHz is shown in Fig 5.2c. As described in Appendix B, these two parameters are factors associated with the calibrated values of R_1 and R_3.

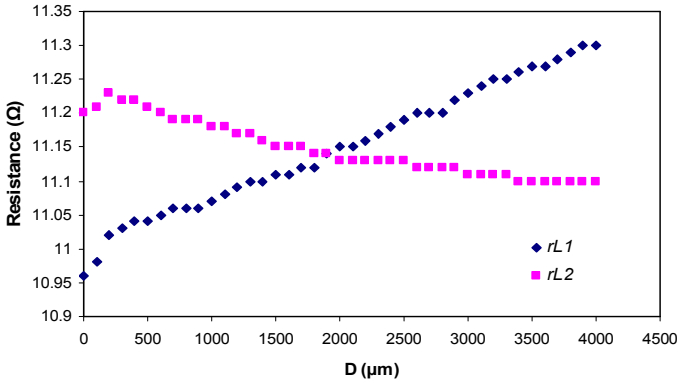

Fig 5.2c Self resistance of coils L_1 and L_2 at f = 100 kHz.

5.2.2 Results for *Migration* Measurements at 100 kHz

As explained in Section 5.1, all the data were collected for *migration* detection on the basis that the resistors R_1 and R_3 were implemented as multi-turn potentiometers which were adjusted by hand against the output which was monitored on an oscilloscope. Note that the operating frequency is fixed to 100 kHz as both the simulated and measured results show that the variations of the calibrated frequency are less than 10% around 100 kHz for all the tests, which can be ignored as the output voltage is insensitive to the frequency changes.

Tables 5.1 to 5.3 and Figs 5.3a-c show measured and calculated values of R_1, R_3 after calibration in relation to gross displacement of the rod (*migration*), with different ratios of R_2 and R_4 (R_2 + R_4 = 500 Ω as explained in Section 4.3.2.1), at 100 kHz. The measured results have 3 significant figures reflecting the precision of the test equipment

and the calculation results were truncated to the nearest ohm to be consistent with the measured results. This data illustrates the 1-to-1 mapping between the values of R_1, R_3 and rod *migration* (*D*), which has already been alluded to and which enables *migration* to be calculated given knowledge of either R_1 or R_3. The calculated results in the tables are from Matlab, using the analytical expression relating these variables which is derived in Appendix B. In practice, it is more convenient to construct a look-up table based on Tables 5.1 to 5.3 to estimate the value for *D* (this approach lends itself well to an automated version of the system).

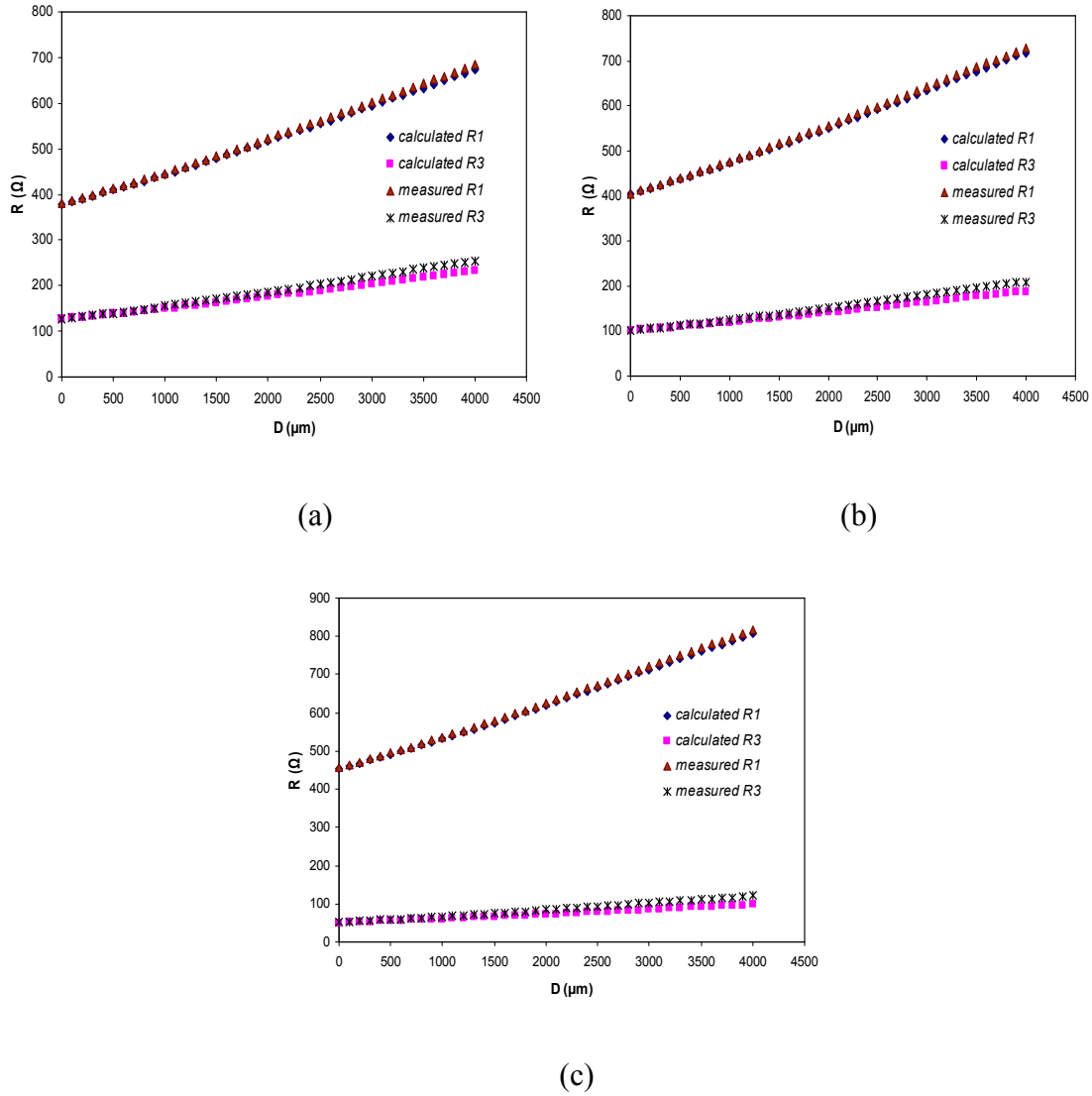

Fig 5.3 The relationship between calibrated values of R_1 and R_3 and the initial gross displacement D (*migration*). The initial values of R_2 and R_4 are: (a) 375 Ω and 125 Ω; (b) 400 Ω and 100 Ω; (c) 450 Ω and 50 Ω. V_{in} = 0.1 V, f = 100 kHz.

The range of *migration* prediction available is about 0 ~ 4 mm (the range can be extended to 0~± 4mm due to the symmetry of the coil pair), with a limiting resolution of about 15 μm, as indicated in the table. This value is calculated from the limiting resolution of the instrument used to measure R_1 (1 Ω). This resolution can further reduce to 1.5 μm if a 16 bits A/D converter is used giving a minimum step of 0.1 Ω for the variable resistors. For 0.1 Ω resistance resolutions, the size of a look-up table is about

64k bits. The error sources are truncation errors in the calculated results, accuracy limitation of test equipment and modeling errors. Note that, as shown in Figs 5.4 and 5.5, the errors between the measured and calculated values of R_1, R_3, in particularly for R_3, increase rapidly with the rod *migration*, contributing to the errors in *migration* and subsequent *micromotion* measurement. Furthermore, it can be noted from Fig 5.4 that errors in R_1 are always less than 2% over the full range of *migration* regardless of the value of R_2/R_4. The error levels of R_3 are much larger than R_1, and increase rapidly with R_2/R_4 (from 8.68% with $R_2/R_4 = 3$ to 18.71% with $R_2/R_4 = 9$, at $D = 4$mm), as shown in Fig 5.5. Therefore, it is better to use the calibrated values of R_1 to estimate the rod *migration* D.

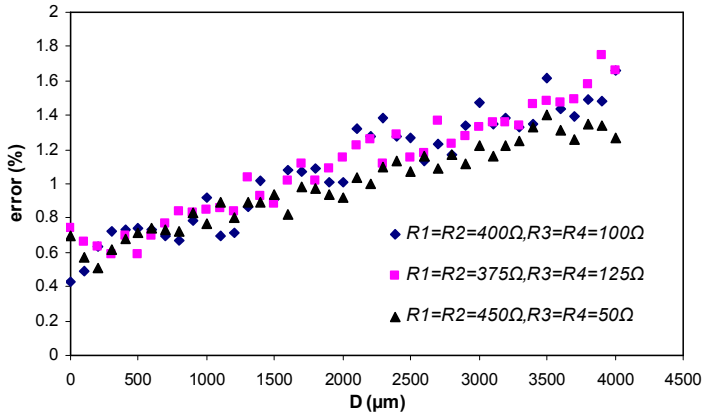

Fig 5.4 Errors between calculated and measured values of R_1 as a function of gross displacement (*migration*) D with different initial values of R_1, R_2, R_3 and R_4 at 100 kHz (see also Tables 5.1 to 5.3).

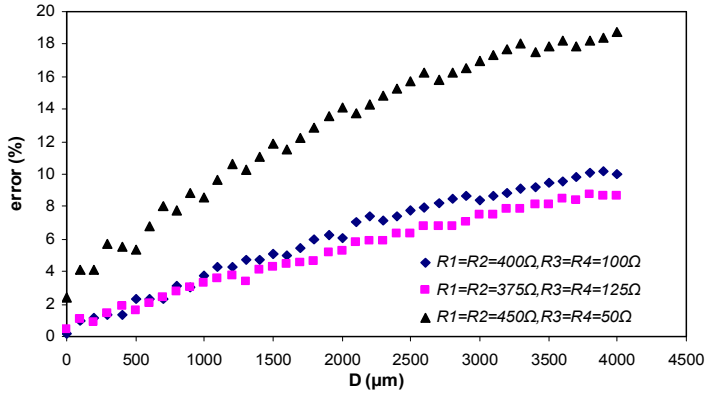

Fig 5.5 Errors between calculated and measured values of R_3 as a function of gross displacement (*migration*) D with different initial values of R_1, R_2, R_3 and R_4 at 100 kHz (see also Tables 5.1 to 5.3).

5.2.3 Results for the Self-Calibrating Subsystem

The variable resistor and the ±90° phase detector were tested separately as part of the automatic calibration system, and the results are shown in this section. Note that the test results for the preamplifier are shown in section 5.3.1 as this amplifier is used for both *migration* and *micromotion* testing.

5.2.3.1 Simulated and Measured Results for the Variable Resistors

In this section, test results are presented for two identical variable resistors (Resistor 1 and Resistor 2) whose schematic is shown in Fig 4.6a. All the symbols and expressions used in this section are defined in Section 4.3.2.2.

Simulated and measured resistance values as a function of the control voltage V_{GS} are shown in Figs 5.6 and 5.7. As noted in these two figures, the resistance values vary approximately between 1.15 kΩ and 244 Ω for Resistor 1 and between 1.25 kΩ and 256 Ω for Resistor 2. These values are higher than the minimum resistance values for R_3 (should be 100 Ω as shown in Table 5.1) and also the simulation results (the minimum value is approximately 133 Ω in simulations) which is attributed to modeling errors. Another source of error is the limit on the resolution of the current measurement (~1 μA). Take Resistor 1 as an example, the resolution constraint of the current can contribute an error between ± 80 Ω with V_{GS} = 0.7 V, and ± 6 Ω with V_{GS} = 1.6 V. As shown in Fig 5.6, the gradient of the control voltage V_{GS} versus the resistance is approximately 0.267 mV/ Ω at 0.7 V < V_{GS} < 0.8 V, 0.256 mV/ Ω at 0.8 V < V_{GS} < 0.9 V, and 2.53 mV/ Ω at 0.9 V < V_{GS} < 1.2 V.

In practice three identical resistors could be connected in parallel, or the value of W/L could be scaled, to get a small value below 100 Ω to represent R_3. Test results for the parallel variable resistors are shown in Fig 5.8 where a total resistance ranging between 80 Ω and 400 Ω is presented.

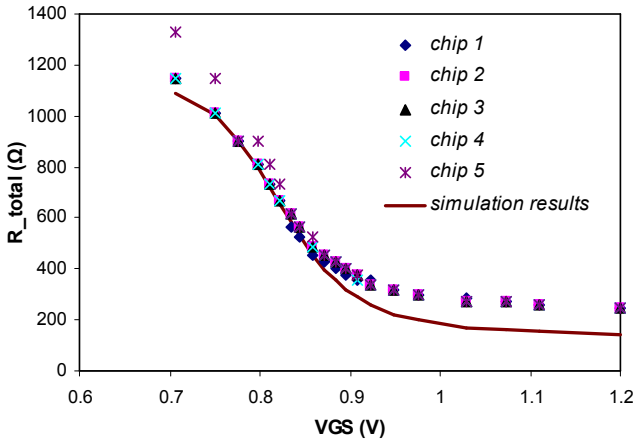

Fig 5.6 Simulated and measured resistance values for Resistor 1 as a function of V_{GS} in five different chips. V_{DS} = 10 mV.

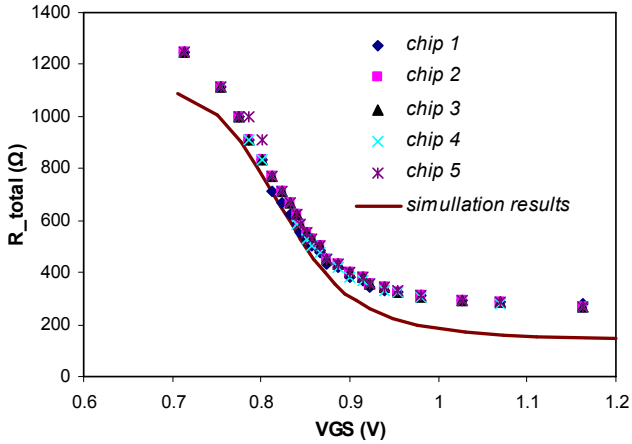

Fig 5.7 Simulated and measured resistance values for Resistor 2 as a function of V_{GS} in five different chips. V_{DS} = 10 mV.

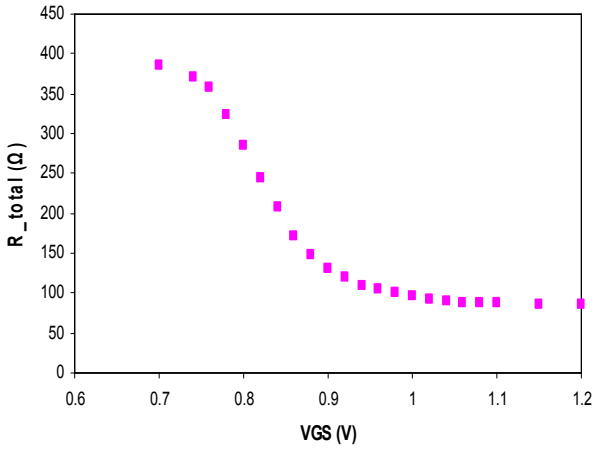

Fig 5.8 Measured resistance values for the three-parallel-connected resistors as a function of V_{GS}. V_{DS} = 10 mV.

The *I-V* characteristic curves at different values of V_{GS} for Resistors 1 and 2 are shown in Figs 5.9 and 5.10. The upper limits of V_{DS} for the linear region of Resistor 1 and Resistor 2 are list in Table 5.4. It is apparent that the ranges of the linear regions in both resistors go up with V_{GS}, which agrees with eqn. (4.3). In practice, V_{DS} = 10 mV was chosen so that the CMOS transistors can always operate in their linear regions, providing a voltage-controlled resistor. Figs 5.11a and 5.11b show the linear regions of the transistor.

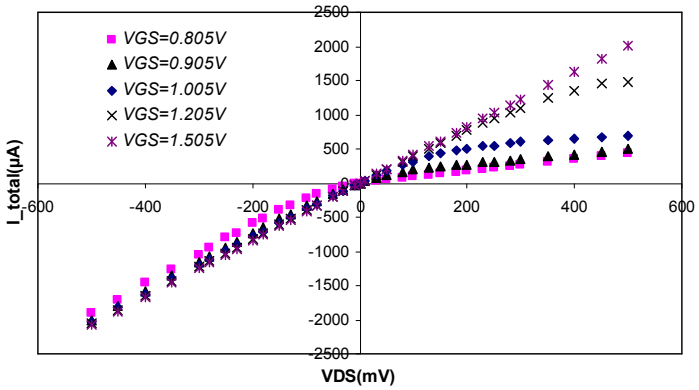

Fig 5.9 The characteristic curves I_{total}-V_{DS} for Resistor 1 with different V_{GS}. I_{total} is the current flowing through the resistor. The threshold voltage to turn on the transistor is about 0.738 V.

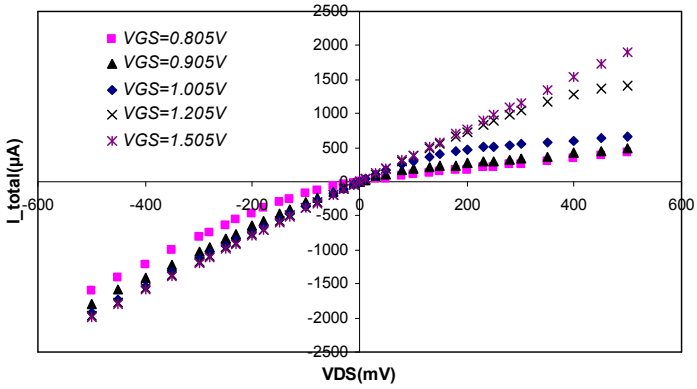

Fig 5.10 The characteristic curves I_{total}-V_{DS} for Resistor 2 with different V_{GS}. The threshold voltage to turn on the transistor is about 0.734 V.

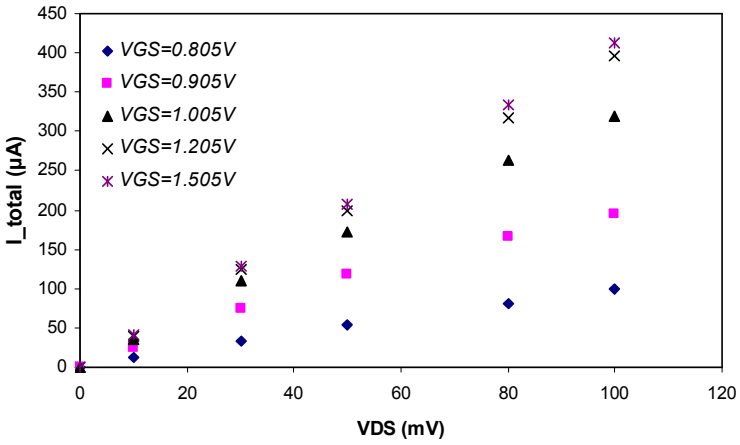

Fig 5.11a The linear region of the characteristic curves I_{total}-V_{DS} for Resistor 1 shown in Fig 5.9.

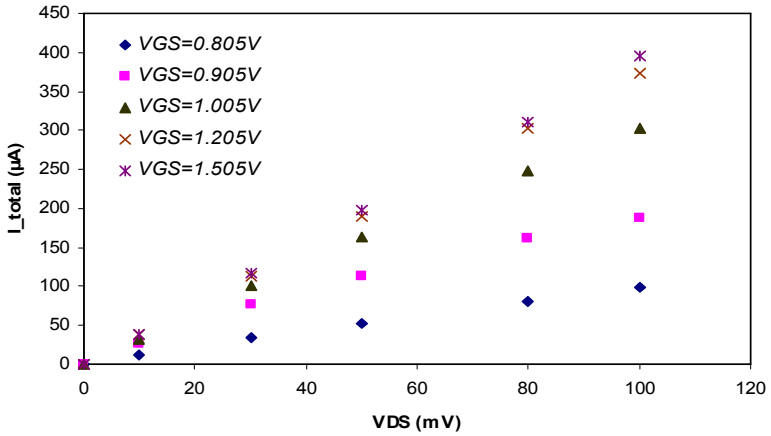

Fig 5.11b The linear region of the characteristic curves I_{total}-V_{DS} for Resistor 2 shown in Fig 5.10.

5.2.3.2 Results for the Phase Quadrature Detector

Measured results of the 0.35 μm and 0.8 μm CMOS phase quadrature detectors described in Chapter 4 are both shown in this section.

5.2.3.2.1 Results for the 0.35 μm Phase Detector

Bench test results show that the 0.35 μm phase detector has a problem of stability in spite of its good performance in the simulation – periodic oscillation at about 350 kHz was always observed in the resistor channel (with an peak amplitude of 175 mV) and 260 kHz in the capacitor channel (with an peak amplitude of 200 mV), which reduces the accuracy of the phase detection as the *D*-type flip-flop is very sensitive to such input fluctuations. The phase detection process may even fail completely at low frequencies due to the increasing number of cycles of oscillation in one period of the input signal. Such performance is described in detail in Table 5.5. However, the phase detector works well at high frequencies, as the results presented below indicate.

As shown in Fig 5.12, the phase shift difference between two channels increases with the operating frequency and achieves a level of about 83º at around 100 kHz when the two input signals are in phase. The error of 7º between the practical and theoretical results may increase the iteration numbers needed for the calibration and influence the

operating frequency adjusted for calibration. The impacts of the phase detection errors on calibration and *migration* measurement are described in Section 6.2.2.

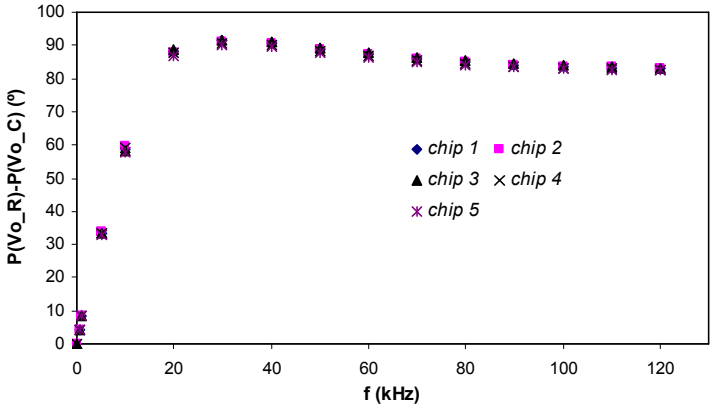

Fig 5.12 Phase differences between the outputs of the source followers of two channels as a function of the operating frequency in 0.35 μm phase detector. $P(V_{o\_R})$ is the phase of the output signal in the resistor channel, and $P(V_{o\_C})$ is the phase of the output signal in the capacitor channel. The input signals for both channels are in phase, with an amplitude of 100 mV for each. Five identical chips are tested separately.

The relationship of the phase differences between two inputs of the flip-flop and the phase difference between the inputs for two channels is shown in Fig 5.13, where five linear curves with a gradient of unit and an intercept of -83º are presented in the range between -180º and 180º. As a result, the phase shift difference between two channels remains -83º over the full phase band of the input.

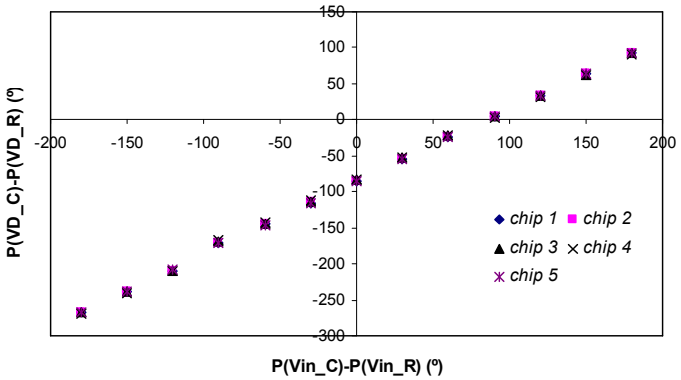

Fig 5.13 Phase differences between two inputs of the flip-flop as a function of the phase differences between two inputs of the 0.35 μm phase detector. $P(V_{D\_R})$ and $P(V_{D\_C})$ are the phases at the input of the flip-flop in the resistor channel and capacitor channel respectively; $P(V_{in\_R})$ and $P(V_{in\_C})$ rare the phases of the input signal of the phase detector in the resistor channel and capacitor channel respectively. f = 100 kHz, V_{in_R} = V_{in_C} = 100 mV. Five identical chips were tested separately.

The performance of the DC level transition at the output of the *D* flip-flop is strongly influenced by the input signal oscillation. As a result, signals appearing at the output of the *D*-type have three states: high DC level (1.5 V), low DC level (-1.5 V) and square waves at the frequency of the input oscillation. Results show that the phase detection fails at frequencies lower than 80 kHz, but improves as the frequency is increased. Values for the input phase differences when the transition occurs between three states at the output are shown in Table 5.5. In practice, this problem can be solved by setting the transition between the low DC level state and the onset of oscillation at the outputs as point at which of the input phase difference is ±90º. In that case, to take Chip 5 as an example, the errors between simulated and measured results for phase detection vary between 0.3° and 5.7° with input signal frequencies between 90 kHz and 200 kHz, as shown in Table 5.5.

Besides unexpected oscillation in the circuit, metastability of d flip flop also contributes to the generation of the square waves at the output, which causes errors in phase detection. One way to suppress it is to use a chain of flip flops with a common clock, so that the probability of the metastability event can be reduced.

The instability of the phase detector also raises a requirement for the minimum allowable amplitude of the input signal, as the phase detection can be interrupted when the oscillating pulses are dominant in the signal. The minimum allowable values (with which an error less than 10º is preserved) of the input signal in the resistor channel with respect to the frequencies are shown in Table 5.6. This value is inversely related to frequency due to the impact of the AC coupling in the phase detector. As a result, a preceding nonlinear amplifier may need to provide signals with sufficient amplitudes at the inputs of the phase detector, which is discussed in Section 6.2.2.

5.2.3.2.2 Results for the 0.8 μm Phase Detector

Measured results for the 0.8 μm phase detector are shown in Figs 5.14-5.15 and Table 5.7. Unlike the 0.35 μm phase detector, there is no oscillation in this case and thus the working bandwidth is larger (60 kHz – 200 kHz) and the accuracy of phase detection is higher (0.1° to 3.6° for Chip 5). The measured lower and upper limits for the input signal amplitude are 20 mV and 150 mV at 100 kHz, to maintain a detection error less than 10º.

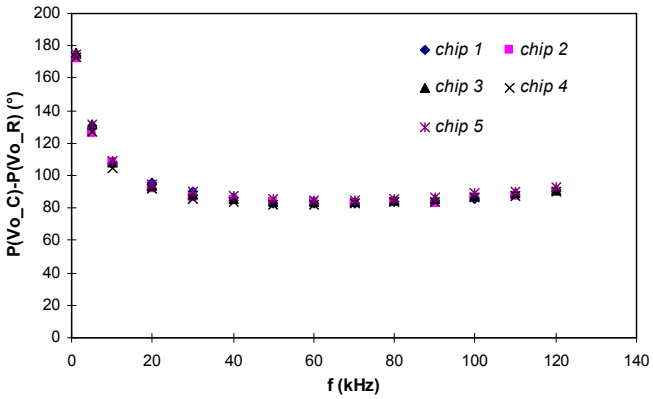

Fig 5.14 Phase differences between the outputs of the source followers of the two channels as a function of the operating frequency in 0.8 µm phase detector. $P(V_{o\_R})$ represents the phase of the output signal in the resistor channel and $P(V_{o\_C})$ represents the phase of the output signal in the capacitor channel. The input signals for the two channels are in phase, with amplitudes of 10 mV for each. Five identical chips were tested.

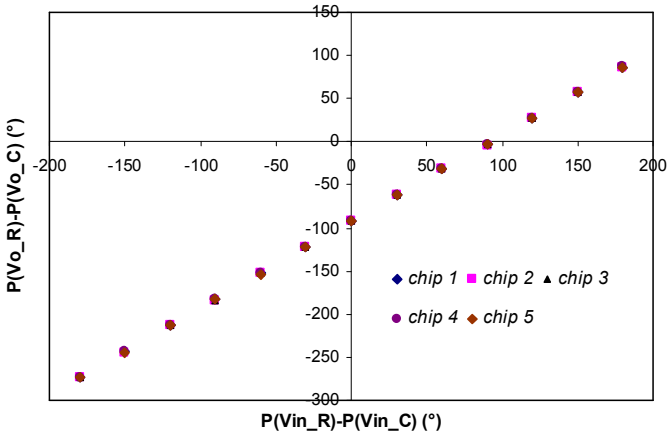

Fig 5.15 Phase differences between the outputs of the source followers of two channels as a function of the phase differences between two inputs of the 0.8 µm phase detector. $P(V_{in\_R})$ and $P(V_{in\_C})$ represent the phase of the input signal of the phase detector in the resistor channel and capacitor channel respectively, f = 100 kHz, $V_{in\_R} = V_{in\_C}$ = 100 mV. Five identical chips were tested.

5.3 Simulated and Measured Results for *Micromotion* Testing

The *micromotion* measurements at 100 kHz, with different bridge parameters, are described in this section. Test results for the amplifier used for both *migration* and *micromotion* measurements are also presented.

5.3.1 Results for the Amplifier

An external source follower (Fig 5.16) is connected to the output of the OTA during the testing of the frequency response of the OTA in order to minimize the influence of the probe capacitance. All the data are collected with single-ended inputs.

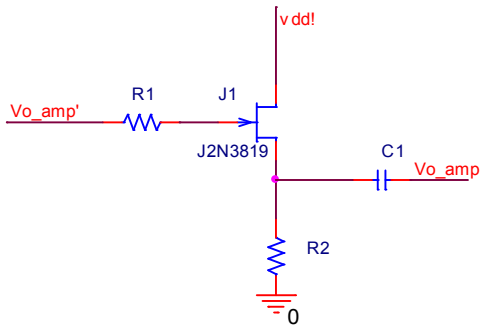

Fig 5.16 The schematic diagram of the JFET source follower connected to the output of the amplifier for testing. *vdd!* = 2.5V, R_1 = 10 kΩ, R_2 = 2 kΩ and C_1 = 1 μF. V_{o_amp}' is the output of the amplifier and V_{o_amp} is the output of the follower.

Figs 5.17 and 5.18 show the output frequency response of the amplifier in terms of gain and the phase shift respectively, with the amplifier parameters shown in Tables 4.8 and 4.9. The 3dB bandwidth is about 5 kHz to 120 kHz. The phase shift of the amplifier is about -225º at 100 kHz, thus two identical preamplifiers should be both connected to the output of the VCO and the output of the bridge in order to cancel the extra phase shift. A voltage divider is connected between the input of the bridge and the preamplifier in order to avoid the distortion at the preamplifier output.

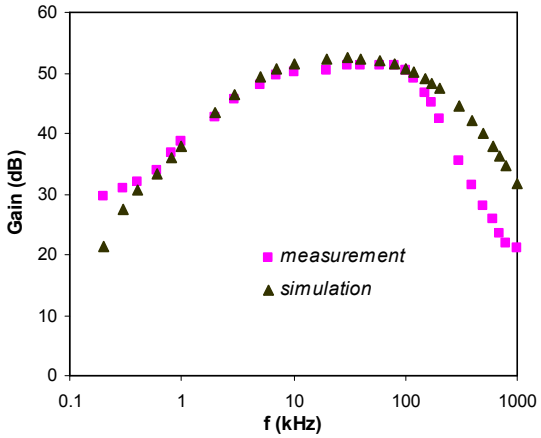

Fig 5.17 The amplitude – frequency response for the amplifier. The amplifier parameters are shown in Tables 4.8 and 4.9. The input voltage V_{in_amp} = 0.4 mV.

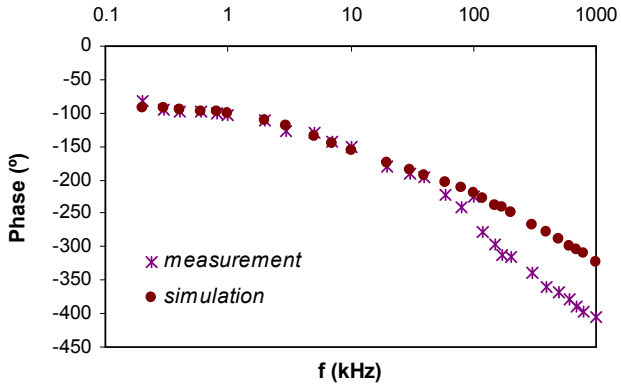

Fig 5.18 The phase – frequency response of the amplifier. The amplifier parameters are shown in Tables 4.8 and 4.9. The input voltage V_{in_amp} = 0.4 mV.

The measured 3dB bandwidth, however, is less than the simulation results (5 kHz to 150 kHz) due to the parasitical capacitance in the circuit board. Figs 5.19 and 5.20 show the simulated and measured amplitude-frequency responses of OTA and OPA respectively. The measured cut-off frequencies of the OTA and the OPA are 200 kHz and 80 kHz, while the simulated cut-off frequencies of the OTA and the OPA are 1.5 MHz and 120 kHz, both of which are higher than the measured results. It indicates that

the value of the parasitical capacitance at the output of the OTA and OPA are approximately 8 pF and 50 pF, respectively.

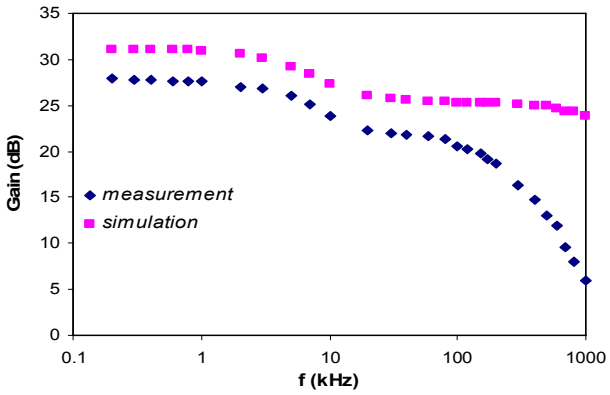

Fig 5.19 Amplitude–frequency response for the OTA. The input voltage V_{in_amp} = 4 mV.

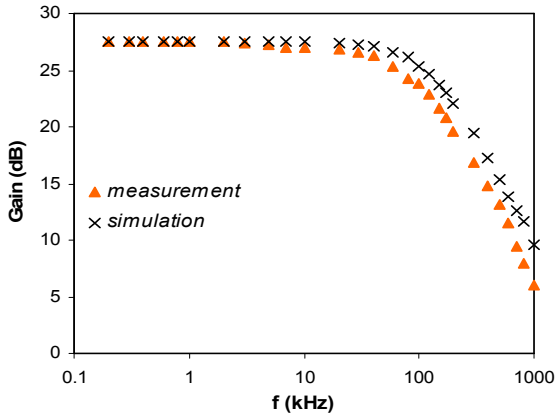

Fig 5.20 Amplitude–frequency response for the OPA. The input voltage V_{in_amp} = 4 mV.

As explained in Section 4.4.1, the bandwidth of the amplifier can be improved by decreasing the load resistance of the OPA (R_{load_OTA}) at the expense of reducing the total voltage gain, and so reducing the resolution of the *micromotion* measurement. However this problem can be solved by increasing the input voltage to the bridge. The new

amplitude-frequency response of the amplifier, tested with R_{load_OPA} = 2.37 kΩ, is shown in Fig 5.21. The 3dB bandwidth is about 5 kHz to 200 kHz, and the total voltage gain at 100 kHz now is about 85. Such gain with V_{in} = 0.3 V still satisfies the minimum required gain (≈ 220 with V_{in} = 0.1 V as discussed in Section 6.3) for *micromotion* testing with 1 μm resolution.

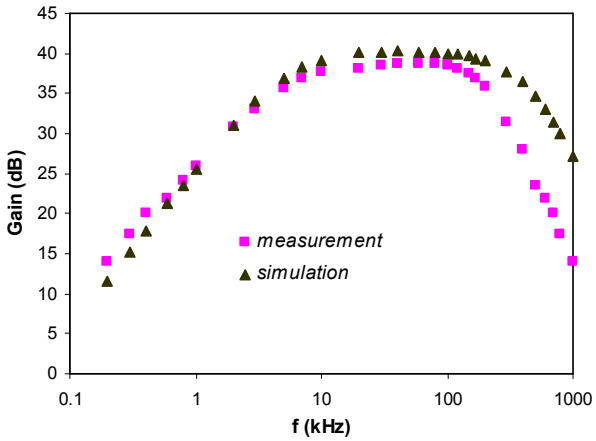

Fig 5.21 The amplitude – frequency response for the amplifier. R_{load_OPA} = 2.37 kΩ. The input voltage V_{in_amp} = 0.4 mV.

The relationship between output and input voltage at 100 kHz is shown in Fig 5.22. The output linearity is preserved (less than 1% distortion) with the input voltage amplitude between 0 and 1.2 mV. The voltage gain is about 420 in the linear region, fitting the requirements for both *micromotion* and *migration* measurements provided that calibration is carried out manually, which is explained in Section 6.3. The amplitude of the output voltage is clamped at about 800 mV by the supply voltage (~1.5V). Note that the tests are made with single-ended inputs, for the differential inputs, the output linearity is preserved with the input voltage less than 400 mV.

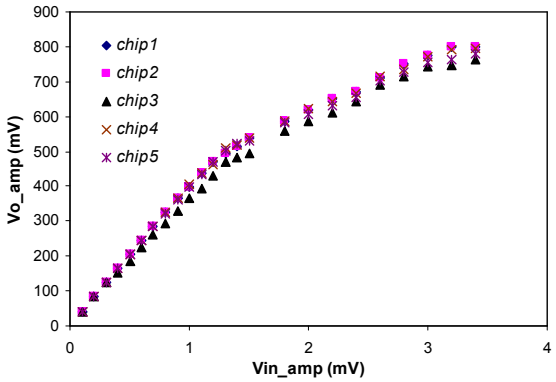

Fig 5.22 The relationship between the output voltage V_{o_amp} and input voltage V_{in_amp}. Five chips have been tested separately. f = 100 kHz. The amplifier parameters are shown in Tables 4.8 and 4.9.

The common mode gain of the OTA is about 0.03 while the differential gain is 15 at 100 kHz, so the CMRR (common-mode-rejection ratio) of the OTA is about 54 dB. On the other hand, the CMRR of the OPA is about 46 dB.

5.3.2 Results for *Micromotion* Measurements at 100 kHz

Once the self-calibration process is completed, the output voltage can be measured with the rod displacement adjusted by the micrometer head with an increment of 1 μm. (The micromotion of the implant is simulated by turing the micrometer by hand, so there is no dynamic measurement of micromotion available). The effect of implementing this procedure is shown in Figs 5.23a-c to 5.24a-c, with different bridge parameters (i.e. initial values of R_2 and R_4, which is explained in Appendix D), at V_{in} = 0.1 V and f = 100 kHz. Note that the amplifier parameters are set with values shown in Tables 4.8 and 4.9. Figs 5.23a to 5.23c show that the output is zero at z = 0 and that the resolution is about 1 μm which is adequate for *micromotion* measurement. Figs 5.24a to 5.24c show the measured variation of the system output as a function of rod *micromotion* under the same input conditions as in Figs 5.23a to 5.23c, but with an extended range of axial displacement (-500 μm to 500 μm). Note that the output gradient and linear range both vary slightly with *migration D* and bridge parameters, due to the changes in resistor values and coil inductance inherent in the process. The linear range of the output voltage as a function of *migration D* and initial values of R_2 and R_4 is shown in Table 5.8.

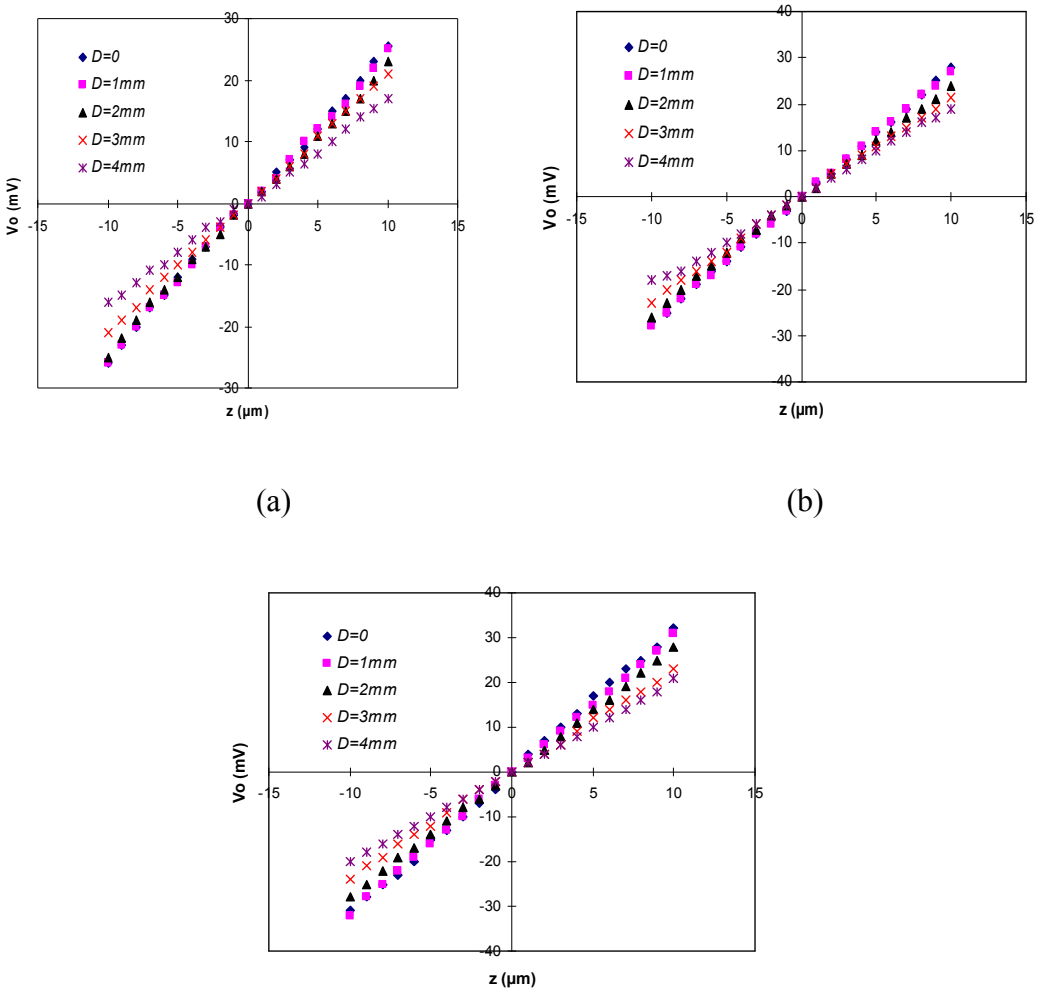

Fig 5.23 Measured system output V_o as a function of small axial displacements (*micromotion*) (-10 µm to 10 µm) for different values of the initial offset D. The initial values of R_2 and R_4 are: (a) 375 Ω and 125 Ω; (b) 400 Ω and 100 Ω; (c) 450 Ω and 50 Ω. All the cases show the response after calibration. V_{in} = 0.1 V, f = 100 kHz.

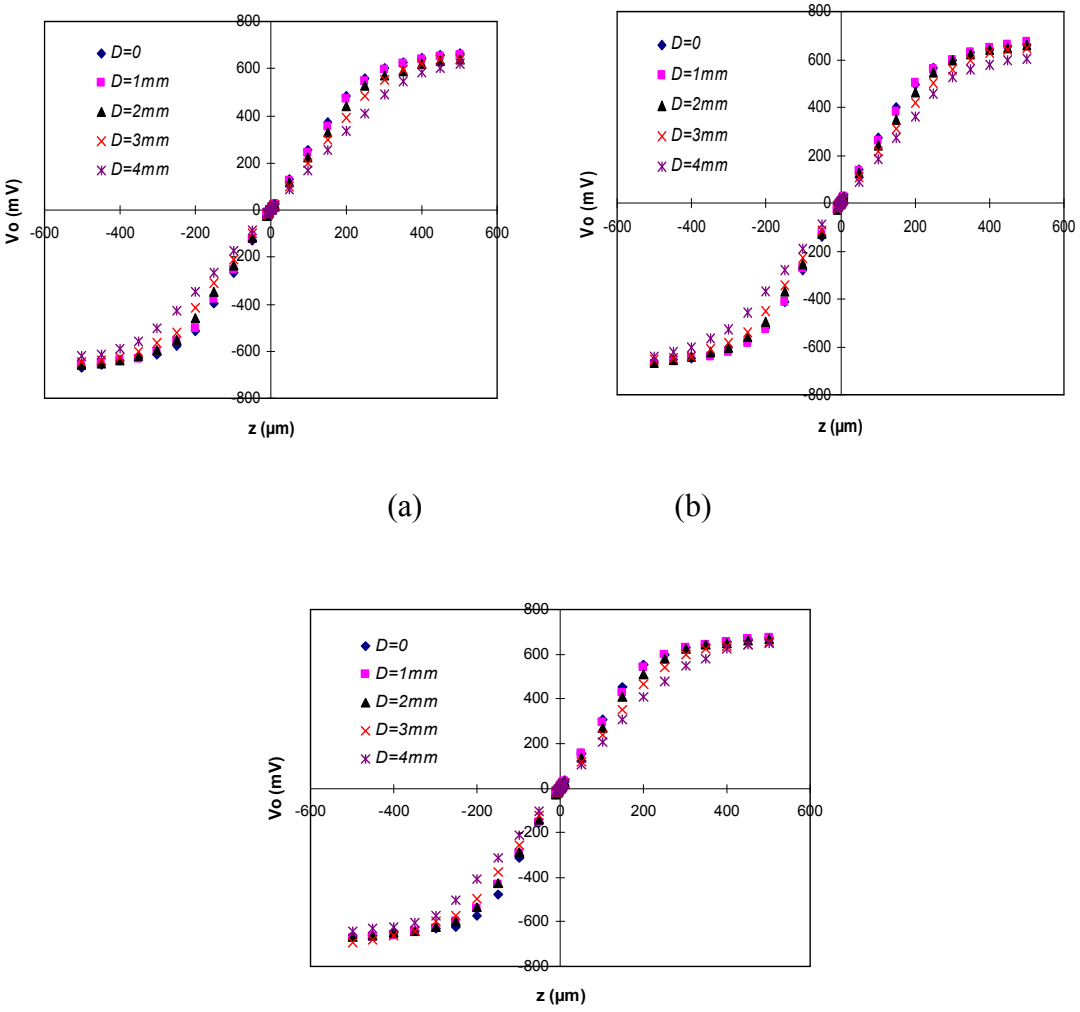

Fig 5.24 Measured system output V_o as a function of small axial displacements (*micromotion*) (-500 µm to 500 µm) for different values of the initial offset D. The initial values of R_2 and R_4 are: (a) 375 Ω and 125 Ω; (b) 400 Ω and 100 Ω; (c) 450 Ω and 50 Ω. All the cases show the response after calibration. V_{in} = 0.1 V, f = 100 kHz.

It is shown in Table 5.8 that output nonlinearity begins to appear at offsets beyond about ± 150 µm, due mostly to the onset of clipping in the amplifiers following the bridge. This suggests that implant *micromotion* can be detected and measured using this system in a range of at least -150 µm to 150 µm, which is adequate for most clinical applications. This value is in excess of the experimentally established lower limit of *micromotion* that, when exceeded, leads to the formation of connective tissue at the bone-implant interface.

This is known to compromise the stability of fixation, and, ultimately, leads to implant loosening [97].

It is important to highlight that the gain of the amplifier following the bridge reduces gradually with the increase of the input voltage beyond a certain level, as shown in Table 5.9. In order to improve the accuracy of the measured gradient, the gradient was referred to the input of the amplifier by dividing the gradient of the bridge at the amplifier output by the amplifier gain. Table 5.10 provides a comparison between the measured and calculated gradients of the output voltage of the bridge as a function of axial displacement, z, with different bridge parameters. These results indicate that the system can estimate *micromotion* with an accuracy varying from 6% to over 10%, depending on initial gross displacement (*migration*), as well as the initial values for R_2 and R_4. The main error source is modeling error originating from the signal generator source impedance and flux leakage in the bridge coils. The noise analysis is discussed in Section 6.3.2.

5.4 Measurements at Lower Frequency (50 kHz)

In this section results for *migration* and *micromotion* measurements at f = 50 kHz are presented. As described in Appendix D, the initial values for R_2 and R_4 are set to 200 Ω and 50 Ω.

5.4.1 Results for *Migration* Measurements

Table 5.11 and Fig 5.25 show measured and calculated values of R_1 and R_3 after calibration with respect of the rod *migration*, at 50 kHz, where a 1-to-1 mapping between the values of R_1 and R_3 and rod *migration* (D) is illustrated, as at 100 kHz. The range of *migration* prediction available is about 0 ~ 4 mm, with a limiting resolution of about 30 μm, as indicated in the table. This is estimated from the limiting resolution of the instrument used to measure R_1 (1 Ω).

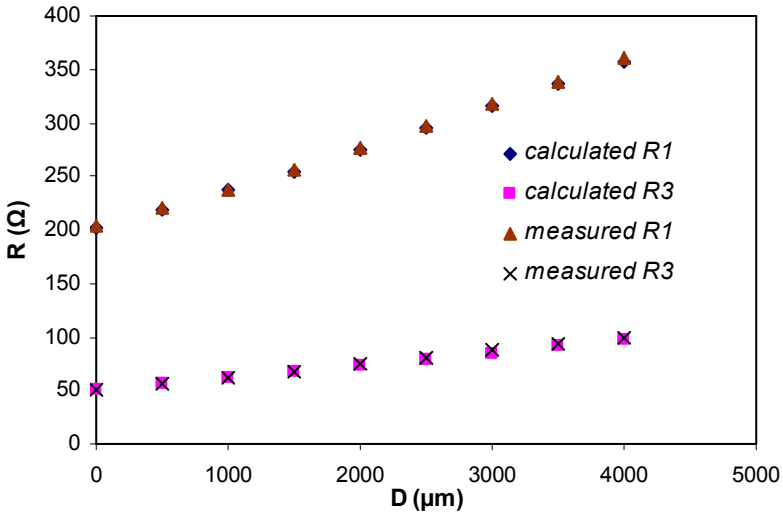

Fig 5.25 Relationship between the calibrated values of R_1 and R_3 and the initial gross displacement D. The initial values of R_2 and R_4 are 200 Ω and 50 Ω. V_{in} = 0.1 V, and f = 50 kHz.

5.4.2 Results for *Micromotion* Measurements

The output voltage with respect to the rod *micromotion* at 50 kHz, in the range between ± 10 μm and ± 500 μm, is shown in Figs 5.26 and 5.27. It is apparent that 1 μm resolution can be achieved with different initial offsets of the rod (0, 2 and 4 mm). The linear range and the comparison between calculated and measured output gradient, as a function of the initial offset of the rod (*migration*), are shown in Table 5.12. Note that the output gradient is the gradient of the output voltage of the *RL* bridge. The error for the gradients is from 8.6% to 17.9%, and the linear range is more than ± 150 μm. The error and linear range for *micromotion* measurements both vary with initial offset of the rod.

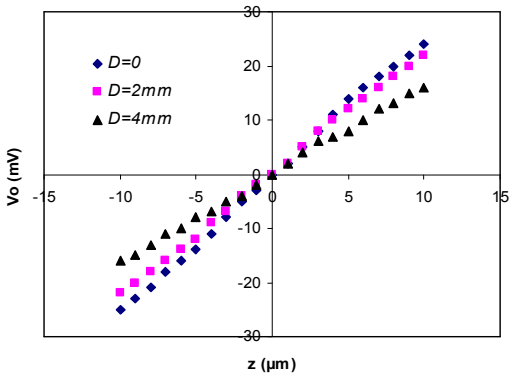

Fig 5.26 Measured system output V_o as a function of small axial displacements (*micromotion*) (-10 µm to 10 µm) for different values of the initial offset D. The initial values of R_2 and R_4 are 200 Ω and 50 Ω. All the cases show the response after calibration. V_{in} = 0.1 V, f = 50 kHz.

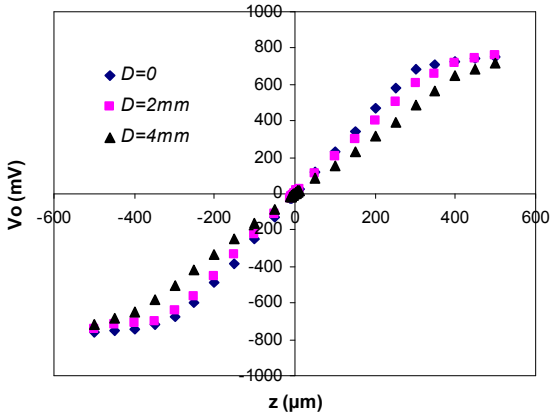

Fig 5.27 Measured system output V_o as a function of small axial displacements (*micromotion*) (-500 µm to 500 µm) for different values of the initial offset D. The initial values of R_2 and R_4 are 200 Ω and 50 Ω. All the cases show the response after calibration. V_{in} = 0.1 V, f = 50 kHz.

The errors between the calculated and measured gradient shown in Table 5.12 are much larger than those at 100 kHz, especially when *migration D* is small. This is because the calibrated values for R_1 and R_3 at 50 kHz (about 250 Ω at D = 0) are much lower than that at 100 kHz (about 500 Ω at D = 0), which increases the impact of the source

impedance (50 Ω) on the output gradient. This factor was not included in the current model.

Measurements at higher frequencies (more than 100 kHz) are beyond the scope of this thesis due to the limitation of the LCR meter, whose maximum testing frequency is 100 kHz.

Tables in this chapter

D (µm)	Calculated R_1, R_3 (Ω/ Ω)	Measured R_1, R_3 (Ω/ Ω)	R_1 error (%)	R_3 error (%)
0	403/101	405/101	0.49	0
100	410/103	412/104	0.49	0.96
200	416/105	419/106	0.71	0.94
300	423/107	426/108	0.70	0.93
400	430/108	433/110	0.69	1.82
500	437/110	440/113	0.68	2.65
600	444/112	447/115	0.67	2.61
700	451/114	454/117	0.66	2.56
800	458/116	461/120	0.65	3.33
900	465/118	469/122	0.85	3.28
1000	472/120	477/125	1.05	4.00
1100	481/123	484/128	0.62	3.91
1200	487/124	491/130	0.81	4.62
1300	496/127	500/133	0.80	4.51
1400	503/129	508/135	0.98	4.65
1500	511/131	516/138	0.97	5.07
1600	518/133	524/140	1.15	5.00
1700	526/135	532/143	1.13	5.59
1800	534/137	540/146	1.11	6.16
1900	542/140	548/149	1.09	6.04
2000	550/142	556/151	1.08	5.96
2100	559/144	566/155	1.24	7.10
2200	567/146	574/158	1.22	7.59
2300	575/149	583/160	1.37	6.88
2400	583/151	591/163	1.35	7.36
2500	591/153	599/166	1.34	7.83
2600	600/156	607/169	1.15	7.69
2700	608/158	616/172	1.30	8.14
2800	616/160	624/175	1.28	8.57
2900	626/163	634/178	1.26	8.43
3000	634/165	643/180	1.40	8.33
3100	642/167	651/183	1.38	8.74
3200	651/170	660/186	1.36	8.60
3300	659/172	668/189	1.35	8.99

3400	668/174	677/192	1.33	9.38
3500	676/177	687/195	1.60	11.3
3600	685/179	695/198	1.44	9.60
3700	693/181	703/201	1.42	9.95
3800	701/183	712/204	1.53	10.3
3900	710/186	721/207	1.52	10.1
4000	718/188	730/209	1.64	10.0

Table 5.1 Comparison of calculated and measured values for R_1, R_3 after calibration as a function of rod *migration D* at 100 kHz. All calculations and measurements are for $R_1 = R_2 = 400\ \Omega$ and $R_3 = R_4 = 100\ \Omega$ initially.

D (μm)	Calculated R_1, R_3 (Ω/ Ω)	Measured R_1, R_3 (Ω/ Ω)	R_1 error (%)	R_3 error (%)
0	378/126	381/127	0.79	0.79
100	384 /129	387/130	0.77	0.77
200	391/131	393/132	0.51	0.75
300	397/133	399/135	0.50	1.48
400	403/135	406/138	0.74	2.17
500	410/138	412/140	0.49	2.43
600	416/140	419/143	0.72	2.10
700	423/142	426/146	0.70	2.74
800	429/145	433/149	0.92	2.68
900	436/147	440/152	0.91	3.29
1000	443/150	447/155	0.89	3.23
1100	450/152	454/158	0.88	3.80
1200	457/155	461/161	0.87	3.73
1300	464/157	469/164	1.07	4.27
1400	472/160	476/167	0.84	4.19
1500	479/163	483/170	0.83	4.12
1600	486/165	491/173	1.02	4.62
1700	493/168	499/176	1.20	4.55
1800	501/171	506/179	0.99	4.47
1900	508/173	514/183	1.17	5.46
2000	516/176	522/186	1.15	5.38
2100	524/179	530/190	1.13	5.79
2200	531/182	538/193	1.30	5.70
2300	539/184	545/196	1.10	6.12

2400	547/187	554/200	1.26	6.50
2500	555/190	561/203	1.07	6.40
2600	562/193	569/207	1.23	6.76
2700	570/196	578/210	1.38	6.67
2800	578/199	585/213	1.20	6.57
2900	586/202	594/217	1.35	6.91
3000	594/204	602/221	1.33	7.69
3100	602/207	610/224	1.31	7.59
3200	610/210	618/228	1.29	7.89
3300	618/213	626/231	1.28	7.79
3400	626/216	635/235	1.42	8.09
3500	633/219	643/238	1.56	7.98
3600	641/222	651/242	1.54	8.26
3700	649/224	659/245	1.52	8.57
3800	657/227	668/249	1.65	8.84
3900	665/230	677/252	1.77	8.73
4000	673/233	684/255	1.61	8.63

Table 5.2 Comparison of calculated and measured values for R_1, R_3 after calibration as a function of rod *migration D* at 100 kHz. All calculations and measurements are for $R_1 = R_2 = 375\ \Omega$ and $R_3 = R_4 = 125\ \Omega$ initially.

D (μm)	Calculated R_1, R_3 (Ω/ Ω)	Measured R_1, R_3 (Ω/ Ω)	R_1 error (%)	R_3 error (%)
0	454/51	457/52	0.66	1.92
100	461/52	464/54	0.65	3.70
200	469/53	471/55	0.42	3.64
300	476/54	479/57	0.63	5.26
400	484/55	487/58	0.62	5.17
500	491/56	495/59	0.81	5.08
600	499/57	503/61	0.80	6.56
700	507/58	511/63	0.78	7.94
800	515/59	519/64	0.77	7.81
900	523/60	528/66	0.95	9.09
1000	532/61	536/67	0.75	8.96
1100	540/62	545/69	0.92	10.1
1200	549/63	553/71	0.72	11.3
1300	557/65	562/72	0.89	9.72

1400	566/66	571/74	0.88	10.8
1500	575/67	580/76	0.86	11.8
1600	583/68	588/77	0.85	11.7
1700	592/69	598/79	1.00	12.7
1800	601/71	607/81	0.99	12.3
1900	610 /72	616/83	0.97	13.3
2000	619/73	625/85	0.96	14.1
2100	628/74	635/86	1.10	14.0
2200	637/75	644/88	1.09	14.8
2300	647/76	654/90	1.07	15.6
2400	656/78	664/92	1.20	15.2
2500	666/79	673/94	1.04	16.0
2600	675/80	683/96	1.17	16.7
2700	684/82	692/97	1.16	15.5
2800	694/83	702/99	1.14	16.2
2900	704/84	712/101	1.12	16.8
3000	713/86	722/103	1.25	16.5
3100	722/87	731/105	1.23	17.2
3200	732/88	741/107	1.21	17.8
3300	742/89	751/109	1.20	18.3
3400	751/91	761/110	1.31	17.3
3500	760/92	771/112	1.43	17.9
3600	770/93	780/114	1.28	18.4
3700	779/95	789/115	1.27	17.4
3800	788/96	799/117	1.38	17.9
3900	798/97	809/119	1.36	17.6
4000	808/98	818/121	1.22	19.0

Table 5.3 Comparison of calculated and measured values for R_1, R_3 after calibration as a function of rod *migration D* at 100 kHz. All calculations and measurements are for $R_1 = R_2 = 450\ \Omega$ and $R_3 = R_4 = 50\ \Omega$ initially.

V_{GS} (V) / Resistor Index	0.805	0.905	1.005	1.205	1.505
1	30mV	30mV	50mV	100mV	500mV
2	30mV	30mV	50mV	100mV	400mV

Table 5.4 The upper limit of V_{DS} for the linear range of Resistor 1 and 2 with different control voltage V_{GS}.

f (kHz)	State transition	$P(V_{in\_C})$ - $P(V_{in\_R})$ (°)				
		Chip 1	Chip 2	Chip 3	Chip 4	Chip 5
90	High level to square waves	-119.8	-120.6	-116.3	-117.4	-118
	Square waves to low level	-94.4	-94.0	-92.0	-90.5	-92.8
	Low level to square waves	84.2	78.9	83.2	74.2	85.3
	Square waves to high level	95.5	93.7	93.8	90.8	95.7
100	High level to square waves	-115.6	-117.0	-113.0	-110.0	-114.2
	Square waves to low level	-93.9	-93.5	-91.4	-89.8	-92.3
	Low level to square waves	85.0	85.1	84.0	81.8	85.8
	Square waves to high level	98.1	101.1	104.0	100.4	97.8
110	High level to square waves	-93.2	-92.9	-90.5	-93.2	-91.7
	Square waves to low level	-92.6	-91.9	-90.0	-92.6	-90.9
	Low level to square waves	86.1	86.2	84.6	86.1	86.8
	Square waves to high level	86.6	86.8	85.1	86.6	87.3
120	High level to square waves	-94.3	-92.7	-91.6	-89.8	-92.7
	Square waves to low level	-93.5	-91.9	-90.8	-89.0	-91.9
	Low level to square waves	86.2	86.8	84.5	82.5	86.8
	Square waves to high level	86.7	87.3	85.0	83.2	87.3
130	High level to square waves	-94.1	-93.8	-91.4	-89.4	-92.6
	Square waves to low level	-93.4	-92.9	-90.5	-88.5	-91.7
	Low level to square waves	86.8	86.8	85.0	83.0	87.4
	Square waves to high level	87.4	87.4	85.6	83.7	87.8
140	High level to square waves	-94.3	-94.0	-91.3	-89.2	-92.5
	Square waves to low level	-93.6	-93.3	-90.6	-88.5	-91.9
	Low level to square waves	87.3	87.3	85.4	83.4	87.7
	Square waves to high level	87.8	87.8	85.9	84.1	88.3
150	High level to square waves	-94.7	-94.5	-91.4	-89.3	-93.2
	Square waves to low level	-94.0	-93.7	-90.7	-88.4	-92.2
	Low level to square waves	87.7	87.7	85.7	83.7	88.1
	Square waves to high level	88.3	88.3	86.3	84.3	88.7
	High level to square waves	-89.9	-90.1	-87.2	-84.9	-90

200	Square waves to low level	-89.5	-89.8	-86.8	-84.4	-89.7
	Low level to square waves	97.1	96.9	93.9	89.3	95.7
	Square waves to high level	97.5	97.5	94.5	89.7	96.1

Table 5.5 Values of the phase differences between two inputs for output level transition with different frequencies in the 0.35 μm phase detector. $V_{in\_C} = V_{in\_R} = 100$ mV.

f (kHz)	90	100	110	120	130	140	150
Minimum V_{in_R} (mV)	80	70	60	65	60	60	45

Table 5.6 Minimum allowable amplitudes for the input signal of the resistor channel (V_{in_R}) with respect to the operating frequencies. $V_{in\_C} = 100$ mV.

f (kHz)	State transition	$P(V_{in\_R}) - P(V_{in\_C})$ (°)				
		Chip 1	Chip 2	Chip 3	Chip 4	Chip 5
50	Low level – High level	-117.2	-119.2	-114.9	-114.7	-108.7
	High level – Low level	90.2	98.4	83.2	86.2	82.0
60	Low level – High level	-93.0	-89.0	-88.7	-93.6	-89.4
	High level – Low level	92.6	98.6	84.5	87.2	85.3
70	Low level – High level	-87.4	-83.9	-82.9	-87.1	-89.9
	High level – Low level	94.6	98.6	85.5	88.8	85.1
80	Low level – High level	-88.8	-85.8	-84.5	-87.4	-90.5
	High level – Low level	95.8	99	86.1	90.1	88.3
90	Low level – High level	-88.9	-85.8	-85.5	-88.3	-91.1
	High level – Low level	97.0	99.0	86.6	90.9	91.8
100	Low level – High level	-94.1	-93.0	-91.0	-91.8	-87.7
	High level – Low level	97.0	98.3	86.2	90.9	92.1
120	Low level – High level	-89.7	-86.8	-86.1	-88.9	-91.0
	High level – Low level	93.6	93.2	90.3	91.6	87.8
200	Low level – High level	-92.8	-89.9	-88.5	-91.8	-92.5
	High level – Low level	91.6	90.7	88.4	89.3	85.7

Table 5.7 Values of the phase differences between two inputs for output level transition with different frequencies in the 0.8 μm phase detector $V_{in\_C} = V_{in\_R} = 100$ mV.

Migration (mm)	Initial R_2 and R_4 (Ω)	Linear range (μm)
0	R_2=375, R_4=125	-200 to 200
	R_2=400, R_4=100	-200 to 200
	R_2=450, R_4=50	-150 to 150
4	R_2=375, R_4=125	-300 to 300
	R_2=400, R_4=100	-250 to 250
	R_2=450, R_4=50	-250 to 250

Table 5.8 Linear range of the output voltage of the amplifier as a function of *migration D* and initial values of R_2 and R_4. V_{in} = 100 mV. f = 100 kHz.

V_{in} (mV)	0.1	0.2	0.3	0.4	0.5	0.6	0.7	0.8
gain	420.0	415.0	410.0	410.0	412.0	410.0	408.6	407.5
V_{in} (mV)	0.9	1.0	1.1	1.2	1.3	1.4	1.5	2.0
gain	406.7	399.0	396.4	390.4	381.5	368.6	489.5	298.0

Table 5.9 The relationship between the gain and the input magnitude of the amplifier (OTA-OPA) at f = 100 kHz. Circuit parameter values are shown in Tables 4.8 and 4.9.

Migration (mm)	Initial R_2 and R_4 (Ω)	Calculated gradient (μV/μm)	Measured gradient (μV/μm)	Error (%)
0	R_2=375, R_4=125	7.1114	6.4975	8.63
	R_2=400, R_4=100	7.5906	6.7761	10.7
	R_2=450, R_4=50	8.5247	7.7702	8.85
1	R_2=375, R_4=125	6.8034	6.1489	9.62
	R_2=400, R_4=100	7.2588	6.5865	9.26
	R_2=450, R_4=50	8.1507	7.3975	9.24
2	R_2=375, R_4=125	6.2567	5.6146	10.3
	R_2=400, R_4=100	6.6687	5.9569	10.7
	R_2=450, R_4=50	7.4811	6.9310	7.35
3	R_2=375, R_4=125	5.4883	5.1515	6.14
	R_2=400, R_4=100	5.8459	5.4323	7.08
	R_2=450, R_4=50	6.5636	6.1038	7.01
4	R_2=375, R_4=125	4.5653	4.2663	6.55
	R_2=400, R_4=100	4.8865	4.5841	6.19
	R_2=450, R_4=50	5.4854	5.1341	6.40

Table 5.10 Comparison between calculated and measured gradients of the output voltage of bridge as a function of *migration D* and initial values of R_2 and R_4. V_{in} = 100 mV. f = 100 kHz.

D (μm)	Calculated R_1, R_3 (Ω/ Ω)	Measured R_1, R_3 (Ω/ Ω)	R_1 error (%)	R_3 error (%)
0	202/51	203/51	0.49	0
500	219/56	220/56	0.45	0
1000	237/61	238/62	0.42	1.61
1500	255/67	256/67	0.39	0
2000	275/73	276/74	0.36	1.35
2500	295/79	297/80	0.67	1.25
3000	316/85	318/87	0.63	2.30
3500	337/91	339/93	0.59	2.15
4000	357/97	360/100	0.83	3.00

Table 5.11 Comparison of calculated and measured values for R_1, R_3 after calibration as a function of rod *migration D* at 50 kHz. All calculations and measurements are for $R_1 = R_2 = 200$ Ω and $R_3 = R_4 = 50$ Ω initially.

Migration (mm)	Calculated gradient (μV/μm)	Measured gradient (μV/μm)	Error (%)	Linear range (μm)
0	7.3298	6.0860	16.9	-150 to 150
2	6.4240	5.5785	13.2	-200 to 200
4	4.7496	4.3407	8.61	-300 to 300

Table 5.12 Linear range and comparison between calculated and measured gradients of the output voltage of bridge as a function of *migration D*. $V_{in} = 100$ mV. $f = 50$ kHz.

6. Discussion

In this section the following issues are discussed:

1. Overview of the device and its operation.

2. Impacts of the bridge parameters on the calibration algorithm.

3. Properties of the preamplifier for *micromotion* measurement with 1 μm resolution.

4. Error analysis of both *migration* and *micromotion* measurements.

5. Practical applications of the device.

6.1 Overview of the Device and Its Operation

In this thesis an *RL* bridge-based technique has been described which enables small axial displacements (≈ 1 μm) of a rod to be measured about a pre-determined zero reference point. The zero reference point can have an axial displacement of about 0 to ±4 mm with respect to the global reference, which is the geometrical centre of the device. The process is analogous to large- and small-signal analysis in conventional analogue circuit theory, since whilst the gross axial displacement requires a nonlinear description, the small displacements can be characterised using linear models.

The bridge consists of a pair of coaxial cylindrical coils into which a ferrite core is inserted. The core is attached to a rod which links the bridge to the external system whose axial displacement is to be measured. It has been shown that the coils can be miniaturised to the point where the complete system (which also includes signal processing and telemetry subsystems) is of a dimension suitable for use in clinical applications such as *total hip arthroplasty* (THA) and *total knee arthroplasty* (TKA), although other, non- clinical applications are possible.

A very important feature of the device is that measurement accuracy for small displacements is preserved across the prescribed range of gross axial displacement, relaxing the constraints on component tolerances and surgical assembly. This is possible due to a self-calibration algorithm which automatically adjusts certain parameters of the device (operating frequency, two variable resistors R_1 and R_3), automatically nulling the output of the bridge to a predetermined limit (see Section 4.3.1) and setting the 'operating point' for the measurement of small displacements. The measured voltages

are converted into axial displacements using the gradient of the output voltage at the operating point defined by the gross displacement D. The value of D can be found from the new values of the variable resistors R_1 and R_3 after the completion of the calibration process. Although the values of these resistors relate uniquely to the gross displacement D, the relationship between them is nonlinear and it is suggested that the use of a look-up table is an effective way of performing this calculation.

The significance of this process is that large and small displacements are accessible separately, leading naturally to the recording of *migration* and *micromotion* in orthopedic prostheses, which is the principal application suggested here. The properties of the calibration algorithm are described in some detail in Section 6.2.

The calculation of both the large and small signal displacements requires analysis which relies on certain assumptions and approximations. A natural consequence of this is that the measurement accuracy is limited. The sources of potential error are listed in Section 6.4 below.

The resolution of the *migration* measurement is approximately 15 μm as shown in Section 5.2.2. This value can be reduced to 1.5 μm, which is quite close to the resolution of the *micromotion* measurement (1 μm), with the use of a 16 bit microcontroller in the future. However, the subsystem for *migration* testing cannot replace the subsystem for *micromotion* testing because: a) the look-up table will take up too much space for a resolution up to 1 μm; b) the self-calibration process is time-consuming, so it may not be able to catch up with the *micromotion* changes.

The resolution of the migration and micromotion measurement will both be improved with the use of a better LCR meter and a better AC voltage meter.

6.2 Properties of the Calibration Algorithm

In this section, the influence of the coupling coefficient k between the coils $L_{1,2}$ and the phase shift of the system (preamplifier and phase detectors) on the number of iterations and convergence of the calibration algorithm are discussed. The optimized bridge parameters are also presented.

6.2.1 Influence of the coupling coefficient *k*

In Section 4.3.1 it was noted that the calibration algorithm consists of *four* steps. For this process to be successful, it is necessary for the equations $REAL = 0$ and $IMAG = 0$ to have real solutions (see eqns. (4.1), (A.9) and (A.10)). In addition, the algorithm must converge in the sense that the termination criterion is ultimately satisfied after N iterations, where N is finite. Table 6.1 shows the number of iterations N required for different values of the coupling coefficient k and the initial value of ΔL, the difference between L_1 and L_2, where $L_1 = L_0 + \Delta L/2$, $L_2 = L_0 - \Delta L/2$, $L_0 = 800$ μH and $R_{1,3}$ lie in the range 100 ~ 1 kΩ. All the data are collected from Matlab-based simulations.

Note: the coils L_1 and L_2 can be connected in anti-phase or in-phase. These are referred to as Type I and Type II respectively. In Table 6.1, negative values of k represent a Type I connection and positive values of k represent Type Π (see also Appendix A).

Table 6.1 illustrates that when k is positive, the number of iterations N increases monotonically with both k and ΔL. With k negative, N increases more slowly. Furthermore, for k positive and with certain values of ΔL, the calibration fails when k exceeds a threshold value. In this case, the maximum allowable values of k (k_{max}) for successful calibration are shown in Table 6.2. It can be seen that there is an inverse correlation between k_{max} and ΔL.

As a result of this observation, in our system the coils are connected so that $k < 0$ and the so bridge can always be calibrated. Using our present measuring system it is difficult to measure N with high precision. This is due to the fact that all adjustments are carried out manually using multi-turn potentiometers. The collection of accurate values of N could be much facilitated by the use of an automatic calibration system employing a microcontroller.

6.2.2 Influence of Preamplifier Phase Shift and Phase Detection Errors

The block diagram of the calibration procedure in the tests is shown in Fig 6.1. According to Matlab simulation results, the phase shift of the preamplifier and errors of the phase detection process can both affect the calibration algorithm in terms of the convergence and the calibrated values of R_1, R_3 and f, which are described as follows (The derivation process is detailed in Appendix E):

1. Phase shifts in the preamplifier and errors of the phase detection process both affect the resonant frequency of the system significantly.
2. Phase shifts in the preamplifier and errors of the phase detection process both affect convergence of the calibration procedure, i.e. the number of the iterations, slightly (by approximately ±1). However the calibration may actually failure with some particular values of the preamplifier phase shift or phase detection errors.
3. Neither the phase shifts of the preamplifier nor the errors of the phase detection process affect the final values for R_1 and R_3, as long as calibration is successful.
4. Errors in phase detection process depend on the input signal amplitudes (Section 4.3.2.4), so an AGC system is needed to stabilize the input signal amplitudes of the phase detectors in order to reduce the phase detection errors and limit the resonant frequency within the working bandwidth of the system.

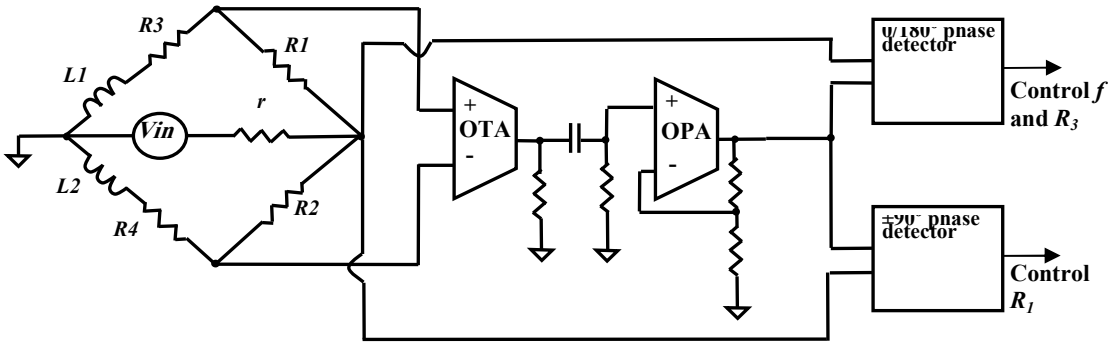

Fig 6.1 Block diagram of the calibration procedure in the tests

The phase shift of the preamplifier can be canceled by planning another identical preamplifier between the input of the bridge and the inputs of the phase detectors. A voltage divider at the input is also needed to avoid overload and large distortion at the

output of the preamplifier. The modified block diagram of the system, including the AGC system and the voltage divider, is shown in Fig 6.2.

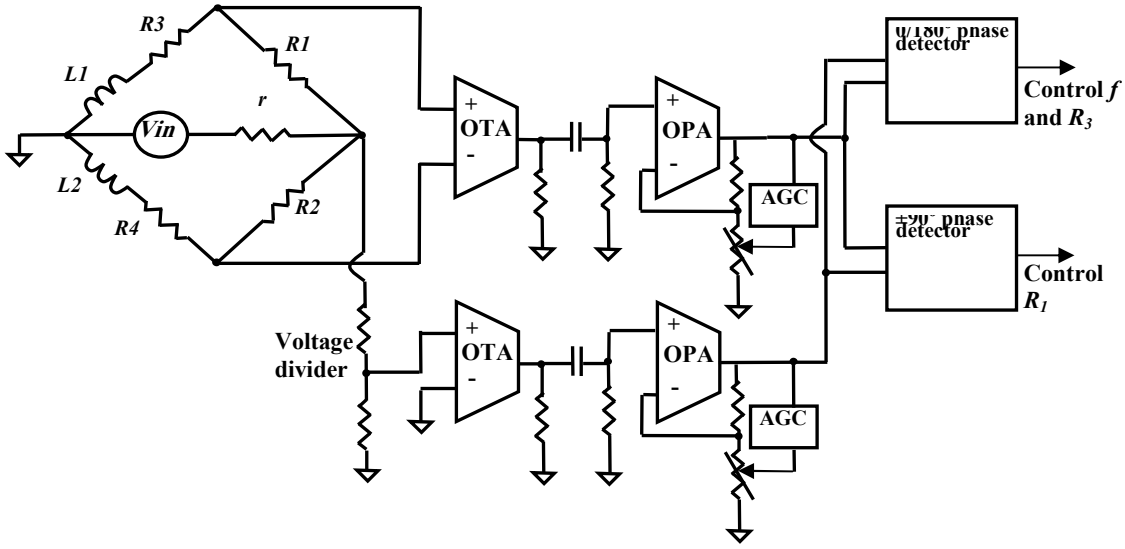

Fig 6.2 Modified block diagram of the system including the AGC system and the voltage divider

6.2.3 Optimized Bridge Parameters

According to the analysis in Appendices A, B and C, the optimized bridge parameters can be characterised in three aspects: number of the iterations of the calibration, resolution and detectable range of the *micromotion* measurement.

Table 6.3 presents the convergence of the system as a function of the initial ratio R_2/R_4 and gross displacement, D, at 100 kHz. This indicates that there is a shallow minimum in the number of iterations required with different values of R_2/R_4 as a function of the gross displacement D (*migration*). However, the variations in the number of iterations caused by the bridge parameters are very small (± 1), as indicated in the table. As a result, the

bridge parameters don't have a significant effect on the calibration convergence at a given frequency.

On the other hand, to achieve a resolution of 1 μm for the *micromotion* measurement, the value of R_2/R_4 should be no less than 0.5 so that the output gradient is greater than 1 mV/μm (the minimum detectable voltage value of the oscilloscope is 1 mV), according to the simulation results in Matlab. Furthermore, Tables 5.9 and 5.11 indicate that the output gradient increases with R_2/R_4, while the output linear range decreases with R_2/R_4. Since the resolution of the *micromotion* measurement is proportional to the output gradient, there is a compromise between the resolution and the detectable range for *micromotion* testing, with different bridge parameters (R_2/R_4). For example, as shown in Tables 5.9 and 5.11, the minimum resolution is 0.4 μm and the maximum detectable range is -200 μm to 200 μm with $R_2/R_4 = 3$, while the minimum resolution is 0.3 μm and the maximum detectable range is -150 μm to 150 μm with $R_2/R_4 = 9$, at $D = 0$. For these reasons, the middle value, $R_2/R_4 = 4$, is chosen for most of the analysis in this thesis. Since $R_2 + R_4 = 500\ \Omega$ at 100 kHz (explained in Appendix D), $R_2 = 400\ \Omega$ and $R_4 = 100\ \Omega$ are chosen.

6.3 Properties of Amplifier for *Micromotion* Measurement

In this section, the principles used to choose the pass-band voltage gain of the amplifier used for *micromotion* measurement with a resolution of 1 μm are discussed. Noise analysis of this amplifier is also presented.

6.3.1 Choice of Voltage Gain in the Passband

All the discussion in this section is based on $R_2 = 400\ \Omega$, $R_4 = 100\ \Omega$, $V_{in} = 0.1$ V and $f =$ 100 kHz, where V_{in} and f are the amplitude and frequency of the input voltage of the bridge.

As shown in Table 5.11, the minimum measured value of the output gradient of the bridge is 4.6×10^{-6} V/μm, which occurs at $D = 4$ mm. As the minimum detectable voltage of the oscilloscope is 1 mV, the gain of the amplifier should be no less than 220 ($\approx 1/(4.6 \times 10^{-3})$) to achieve a resolution of 1 μm for *micromotion* measurement. This value may change with the parameters of the *RL* bridge (k, $L_{1,2}$, $R_{1\text{-}4}$). In our tests the gain of the amplifier was set to 420.

Since the output gradient should be greater than 1 mV/ μm, the output voltage should be less than 1 mV at the balanced point (z = 0). As a result, the value of the transfer function $|H(j\omega)|$ defined in Section 4.3.1 should be less than 4.6×10^{-5} after calibration.

In our tests the *migration* and *micromotion* measurements use a common amplifier for simplicity. However, as explained in Section 6.2.2, a separate AGC preamplifier for calibration as well as *migration* measurements is needed.

6.3.2 Noise Analysis

The noise floor of the amplifier is mainly determined by the transistors in the first step, which is a long tail pair differential amplifier. The equivalent circuit of an FET transistor including noise sources is shown in Fig 6.3. The definitions of the parameters in Fig 6.3 are shown in Table 6.4.

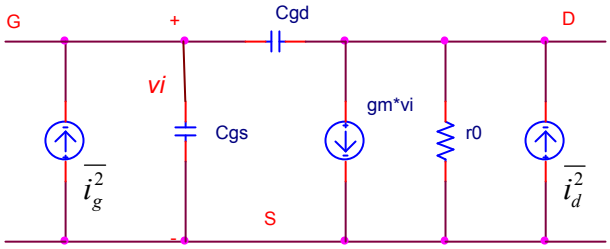

Fig 6.3 FET small-signal equivalent circuit with noise generators

The input noise voltage of the OTA, which consists of the thermal noise and the flicker noise, can be written as (The noise-current generator $\overline{i_g^2}$ can be ignored [99]):

$$\overline{v_{ni\_OTA}^2} = \frac{\overline{i_d^2}}{g_m^2} \approx 2(4kT\frac{2}{3g_m} + K_F\frac{I_D^{af}}{g_m^2 f}) \tag{6.1}$$

As g_m of the OTA is about 2×10^{-4}, according to eqn. (6.1), the input noise voltage spectral density of the amplifier decreases with frequency, and approaches 10 $nV/(Hz)^{0.5}$ ultimately, where the flicker noise can be ignored. As for the output noise, it reaches a peak between 10 kHz and 100 kHz due to the band-bass effect of the amplifier. The simulated input and output noise voltage spectral density are shown in Figs 6.4 and 6.5.

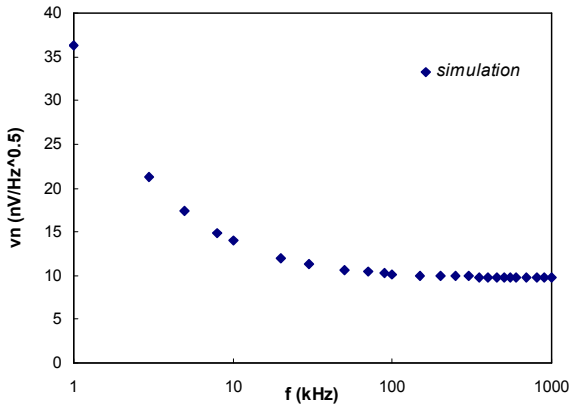

Fig 6.4 Simulated noise voltage spectral density at the input of the amplifier

Assume that:

1. The average power of the output signal amplitude at a frequency of f_0 is $S(f_0)$.
2. The noise spectral density at the output is $n(f)$.
3. The gain of the amplifier is $A(f)$.

The output rms signal-to-noise ratio can be written as:

$$SNR_{out} = \frac{S(f_0)}{\int_0^{\infty} n(f)df} \tag{6.2}$$

And the input rms signal-to-noise ratio can be written as:

$$SNR_{in} = \frac{S(f_0)}{(A(f_0))^2 \cdot \int_0^{\infty} \frac{n(f)}{(A(f))^2} df} \tag{6.3}$$

As the amplifier is a band-pass circuit (explained in Section 4.4.1), $A(f)$ is not constant in the whole frequency band. As a result, the rms SNR at the output of the amplifier is quite different from the rms SNR at the input. In the following section only the output SNR is discussed, as it affects the accuracy of the *micromotion* measurement.

According to the data shown in Fig 6.5, a total rms noise voltage of about 1.96 mV is achieved. As the simulated gain is about 345, the simulated rms SNR at the output is approximately 0.89 with z = 1 μm (*micromotion*) and D = 0 (*migration*). However, the measured noise voltage is much higher than the simulated result, perhaps due to the modeling problems. Fig 6.5 shows a comparison of the noise voltage spectral density between simulated and measured results at the output of the amplifier. Note that only the noise spectral density at frequencies lower than 1 MHz are measured, as the noise voltage in the range of 10 kHz to 1 MHz constitutes most of the total noise, according to the simulation results. It can be seen that the measured noise voltage levels are higher than the simulated noise levels between 1 kHz and 150 kHz. The measured total rms noise voltage floor at the output is approximately 3 mV, and thus the measured SNR at the output is about 0.45 with z = 1 μm (*micromotion*) and D = 0 (*migration*). Note that the measured amplifier gain is 420. The low SNR may influence the accuracy of the *micromotion* measurement.

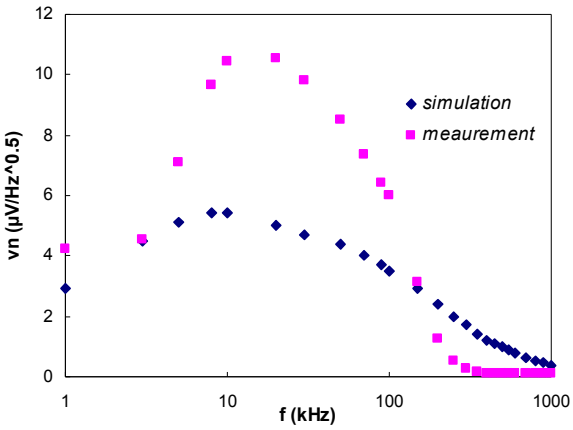

Fig 6.5 Simulated and measured noise voltage spectral density at the output of the amplifier

The measured SNR at the output can be increased to 0.45 × 9 = 4.05 by increasing the input signal level to the bridge from 100 mV to 300 mV, which is desirable.

6.4 Error Analysis

Gross displacement (*migration*) measurements:

Instrument errors: the LCR meter used to determine L_1 and L_2 is accurate to approximately 1%;

Off axis errors which can be ignored, as 1 μm displacement in other two directions only cause 1 nm measurement error in distal direction.

Small displacement (*micromotion*) measurements:

Amplifier nonlinearity: for the largest values considered (± 500 μm) the amplifier output exceeded 600 mV and the onset of clipping was becoming noticeable;

Output impedance of the input signal (50 Ω) which invalidates the model equations for the bridge;

Errors affecting both measurements:

Flux leakage from L_1 and L_2 which is dependent on the position of the ferrite core, invalidating the model equations for the bridge;

VCO output harmonic distortion: although the range of tuning of the VCO is relatively small (approximately 50 kHz – 200 kHz) the resulting harmonic distortion will be larger than for an optimized fixed-frequency unit. However, simulations indicate that the presence of levels of 2^{nd} and 3^{rd} harmonic distortion as high as 1% had no noticeable effect on the calibration algorithm.

Component temperature variation: the system employs several types of components (resistors, inductors, etc) with significant temperature coefficients.

However, since body temperature is very stable (≤ ±1°C, in the absence of infection) this is unlikely to be a problem. In addition, any changes could be immediately corrected by running an extra calibration process.

It is also worth noting that since the small displacement measurements were made using an oscilloscope with a maximum resolution of ± 1 mV, with an amplifier gain of 420 the maximum axial resolution is about ± 0.5 μm.

6.5 Practical Application

Patients will be assessed postoperatively during a clinic visit, in accordance with normal patient follow-up protocols. The automatic calibration algorithm implemented within the device allows *migration* and *micromotion* measurements to be made over an extended period of time. Follow-up assessment dates can be interspaced by a few days in the immediate postoperative period, to a few months in the medium term, usually within one year of the surgical procedure, and annually, biannually or at longer intervals thereafter [97]. At the beginning of each assessment visit, the system would be calibrated enabling the gross axial displacement (*migration)* since the last calibration to be recorded. Since body temperature is very stable (≤ ±1°C, in the absence of infection) the measured change recorded at the time of each calibration is a reliable measurement of gross axial shift (*migration*). During the clinic visit *micromotion* would be measured during, for example, walking and many samples could be collected during each gait cycle.

Tables in this chapter

k \ ΔL(μH)	0	20	100	200	300	400	500	600
-0.9	0	3	4	4	5	5	6	6
-0.8	0	2	3	4	4	4	5	5
-0.7	0	2	3	3	4	4	4	5
-0.5	0	2	2	3	3	3	4	4
-0.2	0	2	2	2	2	3	3	4
0	0	1	2	3	3	3	3	4
0.2	0	2	2	3	3	3	3	N/A
0.5	0	2	3	4	4	N/A	N/A	N/A
0.7	0	3	4	6	N/A*	N/A	N/A	N/A
0.8	0	4	6	N/A	N/A	N/A	N/A	N/A
0.9	0	7	N/A	N/A	N/A	N/A	N/A	N/A

*N/A means the calibration algorithm does not converge.

Table 6.1 The number of iterations (N) required for successful bridge calibration as a function of k and ΔL (N/A means the algorithm does not converge and so calibration is impossible); all calculations are for $L_1 + L_2 = 1600$ μH**.** $R_1 = R_2 = 400$ Ω, $R_3 = R_4 = 100$ Ω and $f = 100$ kHz.

ΔL(μH)	20	100	200	300	400	500	600
k_{max}	0.970	0.855	0.713	0.572	0.430	0.284	0.13

Table 6.2 The maximum values of coupling coefficient (k_{max}) that allows successful calibration of the bridge. All calculations are for $L_1 + L_2 = 1600$ μH**.** $R_1 = R_2 = 400$ Ω, $R_3 = R_4 = 100$ Ω and $f = 100$ kHz.

D(mm) / R_2/R_4	0	1	2	3	4
0.1	1	2	2	3	3
0.5	2	2	3	4	4
1	2	2	3	4	4
2	2	2	3	3	3
3	2	2	3	3	3
4	2	2	3	2	3
5	2	2	2	3	3
6	2	2	2	3	3
7	2	2	2	3	3
8	2	2	2	3	3
9	2	2	2	3	3
10	1	2	2	3	3

Table 6.3 Relationship between the number of iterations required by the calibration process for convergence and the initial choice of resistors ($R_1 = R_2$ and $R_3 = R_4$; $R_1 + R_3 = 500\ \Omega$, $f = 100$ kHz). The dependence on gross displacement D is also shown.

Parameter	Definition
i_g	noise current generator at gate
i_d	noise current generator at drain
g_m	transconductance
v_i	input voltage
r_0	output resistance
C_{gs}	gate-to-source capacitance
C_{gd}	gate-to-drain capacitance

Table 6.4 Definitions of the parameters shown in Fig 6.3.

7. Conclusions and Future Directions

7.1 Conclusions

An implantable motion sensor, which allows the remote *in-vivo* measurement of both large (*migration*) and small (*micromotion*) axial displacements of an implant in applications of THA or TKA, is described in this thesis.

7.1.1 System Properties

The essential part of the sensor is a modified form of DVRT, consisting of two pair of variable resistors and a pair of cylindrical inductive coils attached to the bone, with a ferrite rod attached to the implant and moving along the axis of the coils. The system configuration is described in Chapter 4. The DVRT bridge is driven by a sinusoidal signal. The axial *micromotion* of the implant then can be sensed by the differential output voltage of the bridge due to a linear relationship between the output voltage and the implant displacement. A high-gain amplifier realized in 0.35 μm CMOS technology is connected to the bridge output for signal amplification, with its properties described in Chapters 4 and 6.

7.1.2 Automatic Calibration Method

An automatic calibration method is also proposed in Chapter 4, to set the null-point of the system before the measurements are carried out. The method is based on the convergence of the bridge differential output by adjusting the electrical parameters of the bridge (operating frequency and values of two resistors) alternatively, and is validated by the mathematical analysis proposed in the appendices. The self calibration process not only maximizes the accuracy of the *micromotion* measurements in spite of significant imprecision in initial placement, but also allows the axial gross displacement (*migration*) to be recorded every time after automatically resetting the system, due to a 1-to-1 mapping between the implant *migration* and the calibrated resistance values. The hardware realization of the automatic calibration method requires a VCO, two fixed resistors, two variable resistors, two phase detectors and one AGC preamplifier. The

process is monitored using a 16-bit microcontroller. All the required subsystems are fabricated using 0.35 μm CMOS technology.

7.1.3 *In-vitro* Measured Results

Good agreements between simulated and measured results on *in-vitro* bench tests are reported in Chapter 5, showing that the calibration works correctly absorbing component tolerances and initial set-up errors. The device is shown to measure the *micromotion* with a resolution of 1 μm in the range from -200 μm to 200 μm, and *migration* with a resolution of 15 μm in the range from 0 to ±4 mm. The total power of the system is approximately 3 mW excluding the VCO and the microcontroller.

Although the system is intended initially for the measurement of *micromotion* and *migration* in hip (THA) or knee (TKA) prostheses, there are many other potential applications (e.g. structural measurements within buildings, wear out rate of components).

7.2 Future Directions

At present an integrated version of the system is being developed for *in vitro* testing in the laboratory, which requires a higher level of integration than is currently available to us. A two-chip solution is being considered for this, consisting of a full-custom design containing all the electronic components and subsystems except the microcontroller and realised in 0.35 μm CMOS technology. The full-custom chip together with the microcontroller will be mounted on a small board.

For future *in vivo* evaluations and eventual clinical application, a telemetry system will also be required, although this aspect is not considered in this thesis. The telemetry system will use a pair of coils as the transmitter and receiver, so additional circuit design including a power supply and communications will be required to implement this extra functionality. The whole system will be constructed on a hybrid integrated circuit or miniaturized PCB.

Calibration of the device will be conducted in a composite bone. Using an existing high accuracy micrometer, the effects of misalignment of the sensor will be established to define the sensitivity of the device.

Finally an *in-vitro* validation of the device performance is performed under simulated clinical conditions with the benchmark of RSA data. The sensor will be implanted in composite bone which has received THA or TKA. Following an established protocol, each implant will be subject to cyclic loading conditions simulating activities like single-leg stance or stair climbing. *Migration* and *micromotion* both will be acquired by the remotely-queried sensor and RSA radiographs simultaneously for comparison.

Although currently only axial displacements are measured by our system, rotation is also sometimes significant (e.g. during stair climbing). Extension of the capacity of the device to include rotation is necessary, and will be analyzed in the future study.

References

[1] "History of Total Hip Replacement," http://www.thehipdoc.com/history.htm.

[2] "Hip Replacement: Introduction," http://www.nhs.uk/conditions/Hip-replacement/Pages/Introduction.aspx.

[3] "Knee Replacement: Introduction," http://www.nhs.uk/Conditions/Knee-replacement/Pages/Kneereplacementexplained.aspx.

[4] G. Hawker, et al. **"**Health-related Quality of Life After Knee Replacement," *J Bone Joint Surg Am*, Vol. 80-A, pp. 163-173, 1998.

[5] O. Robertsson, M. Dunbar, T. Pehrsson, K. Knutson and L. Lidgren, "Patient Satisfaction After Knee Arthroplasty: A Report on 27,372 Knees Operated on Between 1981 and 1995 in Sweden," *Acta Orthop Scand*, Vol. 71, pp. 262-267, 2000.

[6] C. Y. Ng, J. A. Ballantyne and I. J. Brenkel, "Quality of Life and Functional Outcome After Primary Total Hip Replacement: A Five-Year Follow-up," *J Bone Joint Surg Br*, Vol. 89-B, pp. 868-873, 2007.

[7] R. D. Ramiah, A. M. Ashmore, E. Whitley and G. C. Bannister, "Ten-year Life Expectancy After Primary Total Hip Replacement," *J Bone Joint Surg Br*, Vol. 89-B, pp. 1299-1302, 2007.

[8] G. Garellick, H. Malchau, P. Herberts, E. Hansson, H. Axelsson and T. Hansson, "Life Expectancy and Cost Utility After Total Hip Replacement," *Clin Orthop*, Vol. 346, pp. 141-151, 1998.

[9] R. Chang, J. M. Pelligier and G. B. Hazen, "A Cost-effectiveness Analysis of Total Hip Arthroplasty for Osteoarthritis of the Hip," *JAMA*, Vol. 275, pp. 858-865, 1996.

[10] M. Nixon, G. Talor, P. Sheldon, S. J. Iqbal and W. Harper, "Does Bone Quality Predict Loosening of Cemented Total Hip Replacements?" *J. Bone and Joint Surg Br*, Vol. 89-B, pp. 1303-1308, 2007.

[11] D. M. Dall, I. D. Learmonth and M. Solomon, "A Scoring System to Determine Rradiological Loosening in Cemented Total Hip Arthroplasty," *International Orthopaedics (SICOT)*, Vol. 16, pp. 339-343, 1992.

[12] K. Hirakawa, J.J. Jacobs, R. Urban and T. Saito, "Mechanisms of Failure of Total Hip Replacements: Lessons Learned from Retrieval Studies," *Clinical Orthopaedics and Related Research*, Vol. 420, pp. 10-17, 2004.

[13] J. R. Moreland, "Mechanism of Failure in Total Knee Arthroplasty," *Clinical Orthopaedics and Related Research*, Vol. 226, pp. 49-64, 1988.

[14] P. Ducheyne, A. Kagan and J. A. Lacey, "Failure of Total Knee Arthroplasty Due to Loosening and Deformation of the Tibial Component," *J Bone Joint Surg Am.*, Vol. 60, pp. 384-391, 1978.

[15] W. Görtz, U. V. Nagerl, H. Nagerl and M. Thomsen, "Spatial Micromovements of Uncemented Femoral Components after Torsional Loads", *Journal of Biomechanical Engineering*, Vol. 124(6), pp. 706-713, 2002.

[16] J. R. Britton, C. G. Lyons and P. J. Prendergast, "Measurement of the Relative Motion between an Implant and Bone under Cyclic Loading," *Strain*, Vol. 40(4), pp. 193-202, 2004.

[17] D. W. Burke, D. O. O'Connor, E. B. Zalenski, M. Jasty and W. H. Harris, "Micromotion of Cemented and Uncemented Femoral Components," *J Bone Joint Surg Br*., Vol. 73, pp. 33-37, 1991.

[18] J. Karrholm, H. Malchau, F. Snorrason and P. Herberts, "Micromotion of Femoral Stems in Total Hip Arthroplasty. A Randomized Study of Cemented, Hydroxyapatite-coated, and Porous-coated Stems with Roentgen Stereophotogrammetric Analysis," *J Bone Joint Surg Am*., Vol. 76, pp. 1692-1705, 1994.

[19] R. D. Mulroy, W. H. Harris, "The Effect of Improved Cementing Techniques on Component Loosening in Total Hip Replacement: An 11-year Radiographic Review," *J Bone Joint Surg Br,* Vol. 72, pp. 757-760, 1990.

[20] C. Laurencin and L. Nair, *Nanotechnology and Tissue Engineering: The Scaffold*, CRC Press, 2008.

[21] C. A. Jones, D. C. Voaklander, D. W. Johnston and M. E. Suarez-Almazor, "Health related Quality of Life Outcomes after Total Hip and Knee Arthroplasties in A Community Based Population," *J Rheumatol.*, Vol. 27, pp. 1745–1752, 2000.

[22] J. J. Callaghan, A. G. Rosenberg and H. E. Rubash, "The Adult Hip," 2nd Ed. Lippincott Williams & Wilkins, 2006.

[23] Hans Hyldahl, Lars Regnér, Lars Carlsson, Johan Kärrholm *and* Lars Weidenhielm, "All-polyethylene vs. Metal-backed Tibial Component in Total Knee Arthroplasty—A Randomized RSA Study Comparing Early Fixation of Horizontally and Completely Cemented Tibial Components: Part 2. Completely Cemented Components: MB Not Superior to AP Components," *Acta Orthopaedica*, Vol. 76, pp. 778-784, 2005.

[24] J. Karrbolm, G. Garellick, C. Rogmark and P. Herberts, "Swedish Hip Registry: Annual Report 2007," http://www.jru.orthop.gu.se, 2008.

[25] J. J. Callaghan, et al., "Results of Charnley Total Hip Arthroplasty at a Minimum of Thirty Years. A Concise Follow-up of a Previous Report," *J Bone Joint Surg Am,* Vol. 86(4), pp. 690-695, 2004.

[26] M. H. Huo and B. S. Brown, "What's New in Hip Arthroplasty," *J Bone Joint Surg Am,* Vol. 85 (9), pp. 1852-1864, 2003.

[27] M. J. Hall and M. F. wings, "2000 National Hospital Discharge Survey," *Adv Data*, 2002.

[28] S. Kurtz, F. Mowat, K. Ong, N. Chan, E. Lau and M. Halpern, "Prevalence of Primary and Revision Total Hip and Knee Arthroplasty in the United States From 1990 Through 2002," *J Bone Joint Surg Am,* Vol. 87 (7), pp. 1487-1497, 2005.

[29] NHS Centre for Reviews and Dissemination and Nuffield Institute for Health, "Total Hip Replacement," *Effective Health Care*, Vol. 2, No. 7, pp. 1-12, 1996.

[30] "Hip Replacement Demand 'to Double'," http://news.bbc.co.uk/1/hi/health/439617.stm, Sep 1999.

[31] A. S. Shanbhag, D. May, C. Cha, C. Kovach, C.T. Hasselman and H.E. Rubash, "Enhancing Net Bone Formation in Canine Total Hip Components with Bisphosphonates," *45th Annual Meeting, Orthopaedic Research Society, California*, pp. 255, 1999.

[32] "History of Total Joint Replacement," http://www.utahhipandknee.com/history.htm.

[33] C. G. Moran and T. C. Horton, "Total Knee Replacement: The Joint of the Decade," *British Medical Journal*, Vol. 320, pp. 820, 2000.

[34] D. R. Diduch, J. N. Insall, W. N. Scott, G. R. Scuderi and D. Font-Rodriguez, "Total Knee Replacement in Young Active Patients: Long-term Follow-up and Functional Outcome," *J Bone Joint Surg Am*, Vol. 79, pp. 575-582, 1997.

[35] G. S. Gill, K. C. Chan, and D. M. Mills, "5- to 18-year Follow-up Study of Cemented Total Knee Arthroplasty for Patients 55 Years Old or Younger," *J Arthroplasty*, Vol. 12, pp. 49-54, 1997.

[36] J. K. Seon, E. K. Song and J. Y. Lee, "Comparison of Range of Motion of High-flexion Prosthesis and Mobile-bearing Prosthesis in Total Knee Arthroplasty," *Orthopedics*, Vol. 28, No. 10, Supplement, pp. s1247-s1250, 2005.

[37] Brad Appleton, "Stretching and Flexibility - Normal Ranges of Joint Motion," http://www.cmcrossroads.com/bradapp/docs/rec/stretching/stretching_8.html.

[38] F. H. Fahey, R. L. Webber, F. S. Chew and B. K. Dickerson, "Application of TACT to the Evaluation of Total Joint Arthroplasty," *Medical Physics*, Vol. 30(3), pp. 454-460, 2003.

[39] J. Patel and K. Bozic, "Computer-navigated Joint-replacement Surgery," *Future Rheumatology*, Vol. 3, No.4, pp. 329-333, 2008.

[40] "Arthritis of the Hip Joint," http://www.hipsandknees.com/hip/hipimplants.htm.

[41] I. D. Learmonth, "Total Hip Replacement and the Law of Diminishing Returns," *J Bone Joint Surg Am,* Vol. 88(7), pp. 1664-1673, 2006.

[42] A. Laupacis, R. Bourne, C. Rorabeck, D. Feeny, P. Tugwell and C. Wong, "Comparison of Total Hip Arthroplasty Performed with and without Cement: A Randomized Trial," *J Bone Joint Surg Am,* Vol. 84 (10), pp. 1823-1828, 2002.

[43] Y-H. Kim, S.-H. Oh, J.-S. Kim and K.-H. Koo, "Contemporary Total Hip Arthroplasty with and without Cement in Patients with Osteonecrosis of the Femoral Head," *J Bone Joint Surg Am*, Vol. 85(4), pp. 675-681, 2003.

[44] H. D. Williams, G. Browne, G. A. Gie, R. S. Ling, A. J. Timperley and N. A. Wendover, "The Exeter Universal Cemented Femoral Component at 8 to 12 years: A Study of the First 325 Hips," *J Bone Joint Surg B,* Vol. 84, pp. 324 -334, 2002.

[45] H. Malchau, P. Herberts, G. Garellick, P. Soderman and T. Eisler, "Prognosis of Total Hip Replacement. Update of Results and Risk-Ratio Analysis for Revision and Rerevision from the Swedish National Hip Arthroplasty Register 1979-2000," *Scientific exhibition presented at the Sixty-Ninth Annual Meeting of the American Academy of Orthopaedic Surgeons*; pp. 13-17, 2002.

[46] R. L. Barrack, R. D. Mulroy and W. H. Harris, "Improved Cementing Techniques and Femoral Component Loosening in Young Patients with Hip Arthroplasty: A 12-year Radiographic Review," *J Bone Joint Surg Br,* Vol. 74, pp. 385-389, 1992.

[47] R. D. Mulroy, D. M. Estok, W. H. Harris, "Total Hip Arthroplasty with Use of So-called Second-generation Cementing Techniques: A Fifteen-year-average Follow-up Study," *J Bone Joint Surg Br,* Vol. 77, pp. 1845-1852, 1995.

[48] A. Valle, A. Zoppi, M. Peterson and E. A. Salvati, "Clinical and Radiographic Results Associated with a Modern, Cementless Modular Cup Design in Total Hip Arthroplasty," *J Bone Joint Surg Am,* Vol. 86(9), pp. 1998-2003, 2004.

[49] "Hip Replacement Implant Loosening," http://orthopedics.about.com/cs/hipreplacement/a/implantissues_2.htm.

[50] "Life Expectance: More Aged 70 and 80 Than Ever Before," http://www.statistics.gov.uk/cci/nugget.asp?id=881, 2004.

[51] L. Labey, et al., "Bone Ingrowth in Total Knee Arthroplasty: the Impact of HA-Coatings and the Relation with Mechanical Stability," *Journal of Biomechanics*, Vol. 31, Supplement 1, pp. 26, 1998.

[52] A. Eskelinen, I. Helenius, V. Remes, P. Ylinen, K. Tallroth and T. Paavilainen, "Cementless Total Hip Arthroplasty in Patients with High Congenital Hip Dislocation," *J Bone Joint Surg Am,* Vol. 88(1), pp. 80-91, 2006.

[53] J. J. Yoo, Y-M. Kim, K.S. Yoon, K-H. Koo, W.S. Song and H. J. Kim, "Alumina-on-Alumina Total Hip Arthroplasty. A Five-Year Minimum Follow-up Study," *J Bone Joint Surg Am,* Vol. 87(3), pp. 530-535, 2005.

[54] M. J. Archibeck, et al. “Second-Generation Cementless Total Hip Arthroplasty : Eight to Eleven-Year Results,” *J Bone Joint Surg Am,* Vol. 83(11), pp. 1666-1673, 2001.

[55] K. S. Keisu et al., “Primary Cementless Total Hip Arthroplasty in Octogenarians : Two to Eleven-Year Follow-up,” *J Bone Joint Surg Am,* Vol. 83(3), pp. 359-363, 2001.

[56] R. A. Berger, L. R. Kull, A. G. Rosenberg and J. O. Galante, “Hybrid Total Hip Arthroplasty: 7- to 10-year Results,” *Clin. Orthop.,* Vol. 333, pp. 134-146, 1996.

[57] V. M. Goldberg, J. Ninomiya, G. Kelly and M. Kraay, “Hybrid Total Hip Arthroplasty: A 7- to 11-year Follow up,” *Clin. Orthop.,* Vol. 333, pp. 147-154, 1996.

[58] Y-H. Kim, H. K. Kook and J. S. Kim, “Total Hip Replacement with a Cementless Acetabular Component and a Cemented Femoral Component in Patients Younger than Fifty Years of Age,” *J Bone Joint Surg Am,* Vol. 84(5), pp. 770-774, 2002.

[59] W. H. Harris and W. J. Maloney, “Hybrid Total Hip Arthroplasty,” *Clin. Orthop.,* Vol. 249, pp. 21-29, 1989.

[60] Ruzanna Harutyunyan, “Total Knee Replacement is Cost-effective,” http://www.emaxhealth.com/2/24/31907/total-knee-replacement-cost-effective.html, 2009.

[61] R. Preidt, “Total Knee Replacement Safe for Most Patients,” http://abcnews.go.com/Health/Healthday/story?id=4509364&page=1.

[62] J. Espigares and E. H. Torres, “Cost-Outcome Analysis of Joint Replacement: Evidence from a Spanish Public Hospital,” *Gaceta Sanitaria*, Vol. 22, No. 4, pp. 337-343, Jul/Aug 2008.

[63] D. M. Albert, “A Physician's Guide to Health Care Management,” Blackwell Publishing, 2002.

[64] V. C. Lansingh, M. J. Carter and M. Martens, “Global Cost-effectiveness of Cataract Surgery,” *Ophthalmology*, Vol. 144(9), pp. 1670-1678, 2007.

[65] P. Hamilton, M. Lemon and R. Field, “Cost of Total Hip and Knee Arthroplasty in the UK. A Comparison with the Current Reimbursement System in the NHS,”

European Federation of National Associations of Orthopaedics and Traumatology (8th Congress), 11-15 May 2007.

[66] "Cost-Effectiveness and Resource Allocation," *Wisconsin Public Health and Health Policy Institute*, 26th May 2005.

[67] I. D. Learmonth and C. P. Case, "Metallic Debris from Orthopaedic Implants," *The Lancet*, Vol. 369, pp. 542-544, 2007.

[68] G. Easton, "Surgery Notes," http://www.bbc.co.uk/health/surgerynotes/geaston/eye_problems.shtml, 2008.

[69] C. S. Ranawat, J. Insall and J. Shine, "Duo-Condylar Knee Arthropiasty. Hospital for Special Surgery Design," *Clin. Orthop.*, vol. 120, pp. 76-82,1976.

[70] M. D. Skolnick, M. B. Coventry and D. M. Ilstrup, "Geomtric Total Knee Arthroplasty. A Two-Year Follow-up Study," *J. Bone and Joint Surg.*, vol. 58-A, pp. 749-753, 1976.

[71] E. Losina, J. Barrett, N. N. Mahomed, J. A. Baron and J. N. Katz, "Early Failures of Total Hip Replacement: Effect of Surgeon Volume," *Arthritis & Rheumatism*, vol. 50, pp. 1338-1343, 2008.

[72] Janie T. Best, "Revision Total Hip and Total Knee Arthroplasty," *Orthopaedic Nursing,* Vol. 24, No. 3, pp. 174-179, 2005.

[73] H. U. Cameron and G. A. Hunter, "**Failure in Total Knee Arthroplasty**: Mechanisms, Revisions, and Results," *Clin Orthop Relat Res.*, No. 170, pp. 141-146, 1982.

[74] Hans Lindahl et al., "Three Hundred and Twenty-one Periprosthetic Femoral Fractures," *J Bone Joint Surg Am,* 88(6), pp. 1215-1222, Jun. 2006.

[75] Andrea E. Buckwalter, "Results of Charnley Total Hip Arthroplasty with Use of Improved Femoral Cementing Techniques. A Concise Follow-up, at a Minimum of Twenty-five Years, of a Previous Report," *J Bone Joint Surg Am,* 88(7), pp. 1481-1485, Jul. 2006.

[76] R. J. Friedmen, P. Hirst, R. Poss, K. Kelley and C. B. Sledge, "Results of Revision Total Knee Arthroplasty Performed for Aseptic Loosening," *Clin Orthop Relat Res.*, No. 255, pp. 235-241, 1990.

[77] S. Breusch and H. Malchau, "The Well-Cemented Total Hip Arthroplasty: Theory and Practice," Springer, 2005.

[78] D. E. Brown and R. D. Neumann, "Orthopedic Secrets," Hanley & Belfus, 2003.

[79] "SMART PLUG: An Implantable Hip Micromotion Sensor."

[80] PS Walker et al., "Prediction of Clinical Outcome of THR from Migration Measurements on Standard Radiographs. A Study of Cemented Charnley and Stanmore Femoral Stems," *J Bone Joint Surg Br,* 77(B), pp. 705-714, 1995.

[81] A. Kobayashi et al, "Early Radiological Observations May Predict the Long-Term Survival of Femoral Hip Prosthesis," *J Bone Joint Surg Br,* 79(B), pp. 583-589, 1997.

[82] S. Gheduzzi and A. W. Miles, "A Review of Pre-clinical Testing of Femoral Stem Subsidence and Comparison with Clinical Data," Proc. IMechE Part H: J. Engineering in Medicine, vol. 221(1), pp. 39-46, 2007.

[83] D.W. Burke, et al. "Dynamic Measurement of Interface Mechanics In Vivo and the Effect of Micromotion on Bone Ingrowth into a Porous Surface Device under Controlled Loads In Vivo (abstract)," *Trans. Orthopaedic Research Society*, Vol. 16, pp. 103, 1991.

[84] R. M. Pilliar, J. M. Lee and C. Maniatopoulos, "Observations on the Effect of Movement on Bone Ingrowth into Porous-surfaced Implants," *Clin Orthop Relat Res.*, No. 208, pp. 108-113, 1986.

[85] S. A. Maher and P. J. Prendergast, "Discriminating the Loosening Behaviour of Cemented Hip Prostheses Using Measurements of Migration and Inducible Displacement," *Journal of Biomechanics*, Vol. 35, pp. 257-265, 2002.

[86] S. Arana, E. Castaño and F.J. Gracia, "High Sensitivity Linear Pposition Sensor Developed Using Granular Ag–Co Giant Magnetoresistances," *Sensors and Actuators A*, Vol. 123, pp. 116-121, 2005.

[87] J. Corda and J. K. Al-Tayie, "Enhanced Performance Variable-reluctance Transducer for Linear-position Sensing," *IEE Proceedings - Electric Power Applications*, pp. 623-628, 2003.

[88] J. Kosel, H. Pfützner, L. Mehnen, E. Kaniusas, T. Meydan, M. Vázquez, M. Rohn, A.M. Merlo and B. Marquardt, "Non-contact Detection of Magnetoelastic Bilayer Position Sensors," *Sensors and Actuators A*, pp. 349-353, 2005.

[89] P. A. Passeraub, P.-A. Besse, S. Hediger, C. d. Raad, and R. S. Popovic, "High-resolution Miniaturized Inductive Proximity Sensor Characterization and Application for Step-motor Control," *Sensors and Actuators A*, vol. 68, pp. 257-262, 1998.

[90] G. Vertesy, J. Szollosy and A. Lovas, "Magnetoinductive Position Sensor," *Magnetics, IEEE Transactions on*, Vol. 26, pp. 2026-2028, 1990.

[91] D. W. Bühler, T. R. Oxland and L. -P. Nolte, "Design and Evaluation of a Device for Measuring Three-Dimensional Micromotions of Press-fit Femoral Stem Prostheses," *Medical Engineering & Physics,* Vol. 19, pp. 187-199, March 1997.

[92] M. A. Freeman and P Plante-Bordeneuve, "Early Migration and Late Aseptic Failure of Proximal Femoral Prostheses," *J Bone Joint Surg Br,* 76(3), pp. 432-438, May 1994.

[93] J Karrholm, "Does Early Micromotion of Femoral Stem Prostheses Matter? 4-7-year Stereoradiographic Follow-up of 84 Cemented Prostheses," *J Bone Joint Surg Br,* 76(6), pp. 912-917, Nov. 1994.

[94] P. Fleming, "Strain on the Human Sciatic Nerve In Vivo During Movement of the Hip and Knee," *J Bone Joint Surg Br*, Vol. 85, pp. 363-365, Apr. 2003.

[95] Chih-Kuo Liang et al., "An Implantable Bi-directional Wireless Transmission System for Transcutaneous Biological Signal Recording," *Physiological Measurement*, Vol. 26, pp. 83-97, 2005.

[96] C. Milgrom, "In Vivo Strain Measurements to Evaluate the Strengthening Potential of Exercises on the Tibial Bone," *J Bone Joint Surg Br*, Vol. 82, pp. 591-594, May 2000.

[97] H. Kienapfel, C. Sprey, A. Wilke and P. Griss, "Implant fixation by bony ingrowth," *The Journal of Arthroplasty*, vol. 14, pp. 355-368, 1999.

[98] S. Hao, J. T. Taylor, A. W. Miles and C. R. Bowen, "An Implantable System for the In Vivo Measurement of Hip and Knee Migration and Micromotion," *Signals*

and Electronic Systems, 2008. ICSES '08. International Conference on, pp. 445-448, 2008.

[99] P. R. Gray, P. J. Hurst, S. H. Lewis and R. G. Meyer, "Analysis and Design of Analog Integrated Circuits," John Wiley & Sons, Inc., 2001.

[100] S. Glyn-Jones, K. Polgar, J. Hicks, D. W. Murray and H. S. Gill, "RSA-measured Inducible Micromotion and Interface Modeling with Finite Element Methods," *Clinical Orthopaedics and Related Research*, No. 448, pp. 98-104, 2006.

[101] E. H. Garling, E. R. Valstar and R. Nelissen, "Comparison of Micromotion in Mobile Bearing and Posterior Stabilized Total Knee Prostheses," *Acta Orthop.*, Vol. 76, pp. 353-361, 2005.

[102] A. Skwara, J. Figiel, T. Knott, J. Paletta, S. Fuchs-Winkelmann and C. Tibesku, "Primary Stability of Tibial Components in TKA: In Vitro Comparison of Two Cementing Techniques," *Knee Surgery, Sports Traumatology, Arthroscopy*, Vol. 17, pp. 1199-1205, 2009.

[103] P. Moonot, M. Shang, G. Railton, R. Field and S. Banks, "In Vivo Weight-Bearing Kinematics with Medial Rotation Knee Arthroplasty," *The Knee*, Article in Press, doi:10.1016/j.knee.2009.06.009.

[104] P. F. Gomez and J. A. Morcuende, "Early Attempts at Hip Arthroplasty: 1700s to 1950s," *Iowa Orthop J.*, Vol. 25, pp. 25-29, 2005.

[105] Luis H. Toledo-Pereyra, "John Charnley—Father of Modern Total Hip Replacement," *Journal of Investigative Surgery*, Vol. 17, pp. 299-301, 2004.

[106] Tucker Cummings, "The History of Hip Replacement," http://www.ehow.com/about_5444826_history-hip-replacement.html.

[107] Jesse Josefsson, "Definition of Total Hip Arthroplasty," http://www.ehow.com/about_5457557_definition-total-hip-arthroplasty.html.

[108] B. Beksac, D. Bek, A. N. Miller and E. A. Salvati, "Thompson Hip Hemiarthroplasty: Asymptomatic after 44 Years a Case Report," *Injury Extra*, Vol. 39, pp. 264-266, 2008.

[109] R. J. Heitmann, "Hip Replacement Surgery From Amputation to Minimally Invasive: A Brief Historical Review*," for Undergraduate Writing in the History of Surgery*, 2007.

[110] J. Install, C. S. Ranawat, W. N. Scott and P. Walker, "Total Condylar Knee Replacement: Preliminary Report," *Clin Orthop*, Vol. 120, pp. 149-154, 1976.

[111] "What is a Total Hip Replacement?" http://www.recoverdiscover.com/hip_replacement.php

[112]"Total Hip Replacement (Total Hip Arthroplasty)," http://www.the-health-pages.com/topics/education/thr.html

Appendices

A. Transfer Function of the Bridge Shown in Fig 4.2

In this section the derivation of the bridge transfer function shown in eqn. (4.1) is presented, based on an idealised (i.e. first-order) model of the coupled inductors L_1 and L_2 (mutual inductance M).

As $M \neq 0$, the voltages appearing across L_1, L_2 are[2]:

$$\begin{cases} V_{L_1} = j\omega L_1 I_1 - j\omega M I_2 \\ V_{L_2} = j\omega L_2 I_2 - j\omega M I_1 \end{cases} \tag{A.1}$$

The input voltage of the bridge, V_{in}, is therefore:

$$V_{in} = (R_1 + R_3) I_1 + V_{L_1} = (R_2 + R_4) I_2 + V_{L_2} \tag{A.2}$$

where the parasitic resistances of the coils, r_{L1} and r_{L2}, are absorbed into the values of R_3 and R_4.

Substitute (A.1) into (A.2) and eliminate V_{L1} and V_{L2}:

$$\begin{aligned} I_2 &= \frac{R_1 + R_3 + j\omega(L_1 + M)}{R_2 + R_4 + j\omega(L_2 + M)} I_1 \\ &= U I_1 = (a + jb) I_1 \end{aligned} \tag{A.3}$$

where:

$$\begin{aligned} U(j\omega) &= \frac{R_1 + R_3 + j\omega(L_1 + M)}{R_2 + R_4 + j\omega(L_2 + M)} \\ &= a + jb \end{aligned} \tag{A.4}$$

Hence eqn. (A.2) can be written as:

$$V_{in} = [R_1 + R_3 + j\omega(L_1 - UM)] I_1 \tag{A.5}$$

[2] The negative signs in eqn. (A.1) relate to M and k negative, i.e, a Type I connection of the coils in which the effect of coupling is to reduce the voltages across L_1 and L_2. In a Type II connection M and k are positive and the signs in the equation are inverted. In practice, as discussed in Section 6.2.1 of the thesis, a Type I connection generally ensures more rapid and reliable convergence of the self-calibration process.

Using eqns. (A.3) and (A.5), the output voltage of the bridge can be calculated:

$$V_{o-bridge} = R_1 I_1 - R_2 I_2 = V_{in} \frac{R_1 - UR_2}{R_1 + R_3 + j\omega(L_1 - UM)} \tag{A.6}$$

Substitute (A.4) into (A.6), the transfer function of the bridge is:

$$H_1(j\omega) = REAL + j.IMAG \tag{A.7}$$

and the output voltage of the bridge (including the amplifier), V_0 is:

$$V_o = A_v.H_1(j\omega).V_{in} = A_v.(REAL + j.IMAG).V_{in} \tag{A.8}$$

where A_v is amplifier gain (assumed to be frequency independent).

and

$$REAL = \frac{(R_1 - aR_2)(R_1 + R_3 + \omega bM) - bR_2\omega(L_1 - aM)}{(R_1 + R_3 + \omega bM)^2 + \omega^2(L_1 - aM)^2} \tag{A.9}$$

$$IMAG = \frac{-bR_2(R_1 + R_3 + \omega bM) - \omega(R_1 - aR_2)(L_1 - aM)}{(R_1 + R_3 + \omega bM)^2 + \omega^2(L_1 - aM)^2} \tag{A.10}$$

where:

$$a = \frac{(R_1 + R_3)(R_2 + R_4) + \omega^2(L_1 + M)(L_2 + M)}{(R_2 + R_4)^2 + \omega^2(L_2 + M)^2} \tag{A.11}$$

$$b = \frac{\omega[(R_2 + R_4)(L_1 + M) - (R_1 + R_3)(L_2 + M)]}{(R_2 + R_4)^2 + \omega^2(L_2 + M)^2} \tag{A.12}$$

B. Convergence Analysis for the Calibration Process Shown in Section 4.3.1

In this section the convergence of the self-calibration algorithm (see Section 4.3.1) is analyzed.

As shown in eqns (A.9) and (A.10), the transfer function is a function of R_1, R_3 and ω. Therefore, the bridge can be balanced (i.e. the transfer function is set to zero) by adjusting these three factors.

The first step, as shown in Section 4.3.1, is to adjust ω to make $IMAG = 0$. The main purpose of this step is to increase the convergence speed. The value of ω after this step is called balanced frequency.

The second step is to adjust the potentiometers R_1 and R_3 alternatively in each iteration to make *REAL* or *IMAG* zero until $|H_1(j\omega)|$ approaches zero. Note that although the value of the balanced frequency will change during this process, it is not necessary to adjust ω again, because the purpose of the calibration process is to set $|H_1(j\omega)|$ to zero other than setting ω to the balanced value finally. Simulated and measured results in Section 5.2.2 as well as eqn (B.9) indicate that it is sufficiently enough to balance the bridge by adjusting R_1 and R_3.

Let $R_{1,n}$ and $R_{3,n}$ represent the calibrated values of R_1 and R_3 at nth iteration, which means $R_{1,n}$ and $R_{3,n-1}$ produces result of zero for *REAL*, while $R_{1,n}$ and $R_{3,n}$ produces result of zero for *IMAG*.

That is,

$$\begin{aligned} REAL(R_{1,n}, R_{3,n-1}) &= 0 \\ IMAG(R_{1,n}, R_{3,n}) &= 0 \end{aligned} \tag{B.1}$$

Substituting (A.9) and (A.10) into (B.1), the relationships between $R_{1,n}$ and $R_{3,n}$ then can be written as::

$$\begin{aligned} R_{1,n} &= \frac{1}{2A_1}[A_3 - A_2 R_{3,n-1} + (A_7 {R_{3,n-1}}^2 + A_8 R_{3,n-1} + A_9)^{\frac{1}{2}}] \\ R_{3,n} &= \frac{1}{2B_1}[B_3 - B_2 R_{1,n} + (B_7 {R_{1,n}}^2 + B_8 R_{1,n} + B_9)^{\frac{1}{2}}] \end{aligned} \tag{B.2}$$

where:

$$A_1 = \frac{R_4(R_2+R_4)+\omega^2 L_2(L_2+M)}{(R_2+R_4)^2+\omega^2(L_2+M)^2}$$

$$A_2 = \frac{(R_4-R_2)(R_2+R_4)+\omega^2 L_2(L_2+M)}{(R_2+R_4)^2+\omega^2(L_2+M)^2}$$

$$A_3 = \frac{R_2\omega^2(L_2+M)M-\omega^2 M(R_2+R_4)(L_1+M)}{(R_2+R_4)^2+\omega^2(L_2+M)^2}$$

$$A_4 = \frac{R_2(R_2+R_4)}{(R_2+R_4)^2+\omega^2(L_2+M)^2}$$

$$A_5 = \frac{R_2\omega^2 M(L_2+M)}{(R_2+R_4)^2+\omega^2(L_2+M)^2}$$

$$A_6 = \frac{R_2\omega^2 L_1(R_2+R_4)(L_1+M)}{(R_2+R_4)^2+\omega^2(L_2+M)^2}$$

$$A_7 = A_2{}^2 + 4A_1A_4$$

$$A_8 = 4A_1A_5 - 2A_2A_3$$

$$A_9 = A_3{}^2 + 4A_1A_6 \qquad \text{(B.3)}$$

and

$$B_1 = \frac{R_2\omega L_2}{(R_2+R_4)^2+\omega^2(L_2+M)^2}$$

$$B_2 = \omega \bullet \frac{2R_2L_2+M(R_2+R_4)}{(R_2+R_4)^2+\omega^2(L_2+M)^2}$$

$$B_3 = \frac{\omega R_2(R_2+R_4)M}{(R_2+R_4)^2+\omega^2(L_2+M)^2}$$

$$B_4 = -\omega \bullet \frac{L_2R_2+M(R_2+R_4)}{(R_2+R_4)^2+\omega^2(L_2+M)^2}$$

$$B_5 = \omega(L_1 - \frac{\omega^2(L_1+M)(L_2+M)-R_2(R_2+R_4)}{(R_2+R_4)^2+\omega^2(L_2+M)^2} \bullet M)$$

$$B_6 = -\omega^3 R_2(L_1+M) \bullet \frac{L_1L_2-M}{(R_2+R_4)^2+\omega^2(L_2+M)^2}$$

$$B_7 = B_2{}^2 + 4B_1B_4$$

$$B_8 = 4B_1B_5 - 2B_2B_3$$

$$B_9 = B_3{}^2 + 4B_1B_6 \qquad \text{(B.4)}$$

The two equations in (B.2) can be simplified by expanding $(A_7R_{3,n-1}^2+A_8 R_{3,n-1}+A_9)^{1/2}$ and $(B_7R_{1,n}^2+B_8 R_{1,n}+B_9)^{1/2}$ using a Taylor series expansion about the real numbers E_1 and E_2, if E_1 and E_2 are sufficiently close to $R_{3,n-1}$ and $R_{1,n}$:

$$
\begin{aligned}
&(A_7 R_{3,n-1}{}^2 + A_8 R_{3,n-1} + A_9)^{\frac{1}{2}} \\
&= (A_7 E_1{}^2 + A_8 E_1 + A_9)^{\frac{1}{2}} + \frac{1}{2}(A_7 E_1{}^2 + A_8 E_1 + A_9)^{-\frac{1}{2}}(2A_7 E_1 + A_8)(R_{3,n-1} - E_1) + Rm_1 \\
&\textit{and} \\
&(B_7 R_{1,n}{}^2 + B_8 R_{1,n} + B_9)^{\frac{1}{2}} \\
&= (B_7 E_2{}^2 + B_8 E_2 + B_9)^{\frac{1}{2}} + \frac{1}{2}(B_7 E_2{}^2 + B_8 E_2 + B_9)^{-\frac{1}{2}}(2B_7 E_2 + B_8)(R_{1,n} - E_2) + Rm_2
\end{aligned}
\tag{B.5}
$$

where Rm_1 and Rm_2 are remainder terms.

To simply (B.5), the following two assumptions are made based on analysis above:

i) $E_1 = R_4 + (d/d_{max})*((R_{3,\infty})_{dmax} - R_4)$, $E_2 = R_2 + (d/d_{max})*((R_{1,\infty})_{dmax} - R_2)$ with $0<n<\infty$, where d is the initial gross displacement (*migration*), d_{max} is maximum allowable *migration* (in our test it is 4 mm), and $(R_{1,\infty})_{dmax}$ and $(R_{3,\infty})_{dmax}$ are values for $R_{1,3}$ when n approaches infinity at $D = d_{max}$.

ii) Rm_1 and Rm_2 can both be ignored.

Based on these two assumptions, (B.2) can be reduced as follows by substituting (B.5) to (B.2):

$$
\begin{aligned}
R_{1,n} &\approx X_0 + X_1 R_{3,n-1} \qquad n \geq 1 \\
R_{3,n} &\approx Y_0 + Y_1 R_{1,n} \qquad n \geq 1
\end{aligned}
\tag{B.6}
$$

where:

$$X_0 = \frac{A_3}{2A_1} + \frac{1}{2A_1}(A_7E_1^{\,2} + A_8E_1 + A_9)^{\frac{1}{2}} - \frac{E_1}{4A_1}(A_7E_1^{\,2} + A_8E_1 + A_9)^{-\frac{1}{2}}(2A_7E_1 + A_8);$$

$$X_1 = \frac{1}{4A_1}[(A_7E_1^{\,2} + A_8E_1 + A_9)^{-\frac{1}{2}}(2A_7E_1 + A_8) - 2A_2];$$

$$Y_0 = \frac{B_3}{2B_1} + \frac{1}{2B_1}(B_7E_2^{\,2} + B_8E_2 + B_9)^{\frac{1}{2}} - \frac{E_2}{4B_1}(B_7E_2^{\,2} + B_8E_2 + B_9)^{-\frac{1}{2}}(2B_7E_2 + B_8);$$

$$Y_1 = \frac{1}{4B_1}[(B_7E_2^{\,2} + B_8E_2 + B_9)^{-\frac{1}{2}}(2B_7E_2 + B_8) - 2B_2]$$

(B.7)

Substitute the expression of $R_{3,n}$ into the expression of $R_{1,n}$ in (B.6), therefore the expression of $R_{1,n}$ as a function of $R_{1,0}$ is:

$$R_{1,n} \approx \begin{cases} X_0 + X_1R_{3,0}; & n = 1 \\ \sum_{m=0}^{n-2}(X_1Y_1)^m(X_0 + X_1Y_0) + (X_1Y_1)^{n-1}R_{1,1}; & n > 1 \end{cases}$$

$$R_{3,n} \approx \sum_{m=0}^{n-1}(X_1Y_1)^m(Y_0 + X_0Y_1) + (X_1Y_1)^nR_{3,0}; \qquad n \geq 1 \tag{B.8}$$

It is apparent that $R_{1,n}$ and $R_{3,n}$ converge towards a limiting value as n approaches infinity if $|X_1Y_1| < 1$. This limit corresponds to zeros of the functions *REAL* and *IMAG* (B.1) and hence the null point of the bridge. To show convergence, it is *sufficient* (but not *necessary*) to show that $|X_1Y_1| < 1$.

The plots of individual inductance of L_1, L_2 and coupling coefficient k as a function of *migration* (D) are shown in Figs B.1 and B.2. The expression of $|X_1Y_1|$, however, is a high-order function of L_1, L_2 and k, which varies with the initial displacement of the rod (*migration*). Here we examine the inequality $|X_1Y_1| < 1$ using a graphical method. The plot of $|X_1Y_1|$ as a function of the initial *migration* with different bridge parameters (Figs B.3a – B.3c) at f = 100 kHz shows that the value of $|X_1Y_1|$ is always less than 1 with the initial *migration* between 0 to 4 mm. In conclusion, the bridge can be calibrated after a finite number of iterations with the initial *migration* between 0 to 4 mm, at f = 100 kHz.

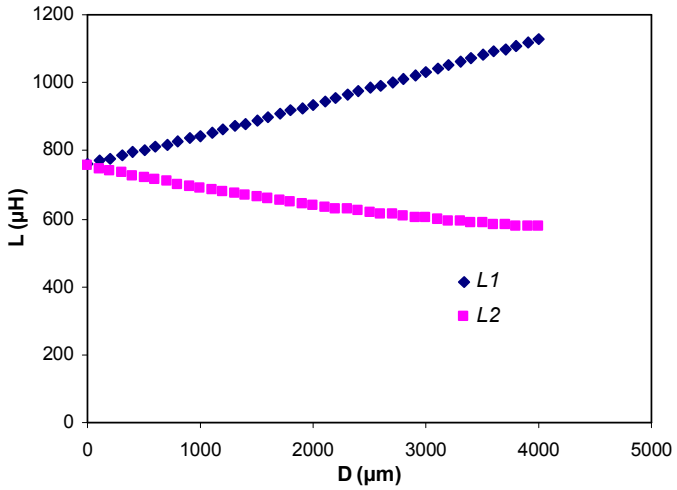

Fig B.1 Inductance of L_1, L_2 as a function of *migration D* between 0 and 4 mm.

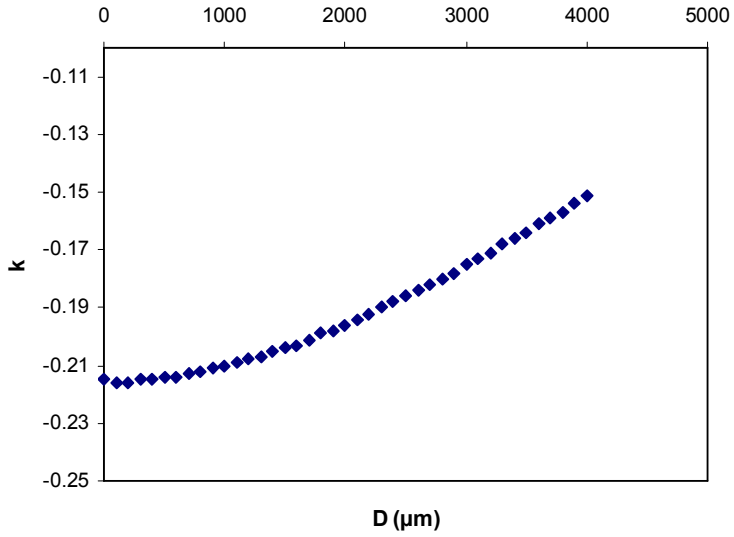

Fig B.2 Coupling coefficient *k* as a function of *migration D* between 0 and 4 mm.

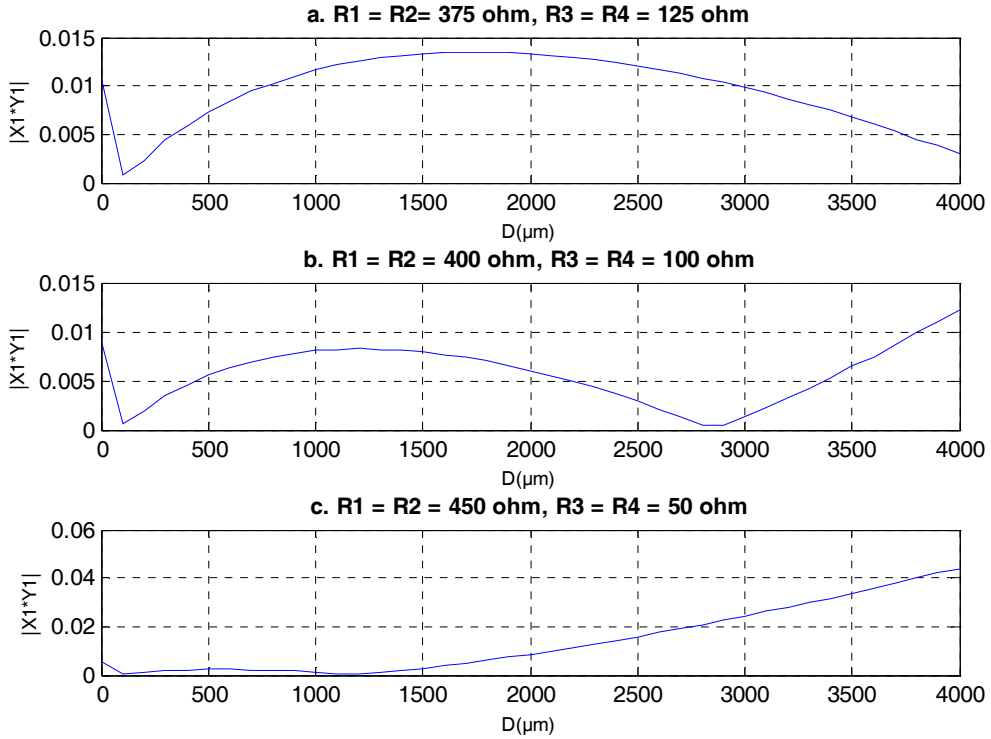

Fig B.3 X_1Y_1 as a function of the initial *migration* (D) in the range between 0 and 4 mm with f = 100 kHz and initially a) $R_1 = R_2 = 375\ \Omega$, $R_3 = R_4 = 125\ \Omega$; b) $R_1 = R_2 = 400\ \Omega$, $R_3 = R_4 = 100\ \Omega$ and c) $R_1 = R_2 = 450\ \Omega$, $R_3 = R_4 = 50\ \Omega$. It can be seen that $|X_1Y_1| < 1$ throughout the range in all three figures.

As shown in (B.8), when n → +∞, the values of $R_{1,n}$ and $R_{3,n}$ are:

$$R_{1,\infty} \approx \frac{X_0 + X_1 Y_0}{1 - X_1 Y_1}$$
$$R_{3,\infty} \approx \frac{Y_0 + X_0 Y_1}{1 - X_1 Y_1} \qquad \text{(B.9)}$$

It should be noted that $R_{1,\infty}$ and $R_{3,\infty}$ shown in eqn. (B.9) are both the sum of the variable resistance value and the coil resistance value, as mentioned in Appendix A. The accuracy validation of eqn. (B.9) is illustrated in Figs B.4a-B.4c by comparing the calibrated values for R_1, R_3 calculated from eqn. (B.9) and those from eqn. (B.1). The low errors (< 0.15%) between two groups of values validate not only the eqns. (B.8) and (B.9) as formulas for values of R_1, R_3 after calibration, but also the two assumptions made above for the simplification of (B.2).

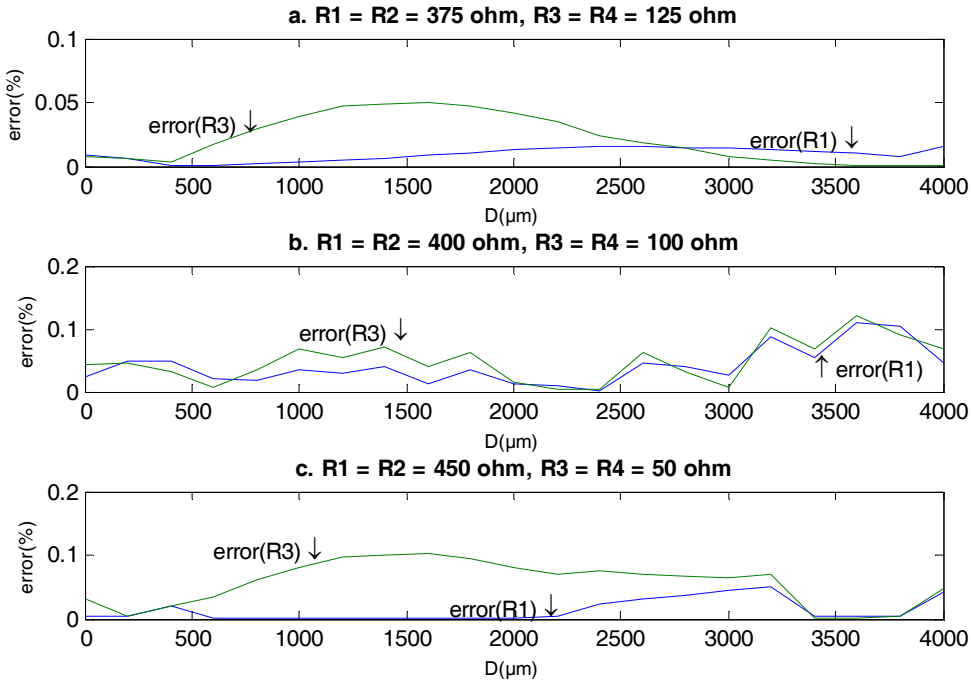

Fig B.4 Errors between the calibrated values for R_1, R_3 calculated from eqn. (B.9) and those from eqn. (B.1) as a function of *migration D* with f = 100 kHz and initially a) $R_1 = R_2 = 375\ \Omega$, $R_3 = R_4 = 125\ \Omega$; b) $R_1 = R_2 = 400\ \Omega$, $R_3 = R_4 = 100\ \Omega$ and c) $R_1 = R_2 = 450\ \Omega$, $R_3 = R_4 = 50\ \Omega$.

The bridge can also be calibrated by adjusting the output amplitude to minimum value instead of adjusting the output phase shift. In this case, the new calibration process is:

5. Sweep the oscillator frequency until the phase angle of $H_1(j\omega)$ is 0° or 180º. This is the balance frequency of the system and sets the term *IMAG* in (1) to zero.
6. Adjust R_1 until the output amplitude reaches its minimum value. This set $\partial|H(j\omega)|/\partial R_1$ to zero.
7. Adjust R_3 until the output amplitude reaches its minimum value. This set $\partial|H(j\omega)|/\partial R_3$ to zero.
8. Repeat steps 2 and 3 until the output is zero.

The equation $\partial|H(j\omega)|/\partial R_1 = 0$ and $\partial|H(j\omega)|/\partial R_3 = 0$ can be simplified as follows:

$$\frac{\partial |H(j\omega)|}{\partial R_1} = 0$$

$$\Rightarrow REAL\_NU * (\frac{\partial REAL\_NU}{\partial R_1} * DE - \frac{\partial DE}{\partial R_1} * REAL\_NU) \tag{B.10}$$

$$+ IMAG\_NU * (\frac{\partial IMAG\_NU}{\partial R_1} * DE - \frac{\partial DE}{\partial R_1} * IMAG\_NU) = 0$$

$$\frac{\partial |H(j\omega)|}{\partial R_3} = 0$$

$$\Rightarrow REAL\_NU * (\frac{\partial REAL\_NU}{\partial R_3} * DE - \frac{\partial DE}{\partial R_3} * REAL\_NU) \tag{B.11}$$

$$+ IMAG\_NU * (\frac{\partial IMAG\_NU}{\partial R_3} * DE - \frac{\partial DE}{\partial R_3} * IMAG\_NU) = 0$$

where:

$$REAL\_NU = (R_1 - aR_2)(R_1 + R_3 + \omega bM) - bR_2\omega(L_1 - aM)$$

$$IMAG\_NU = -bR_2(R_1 + R_3 + \omega bM) - \omega(R_1 - aR_2)(L_1 - aM)$$

$$DE = (R_1 + R_3 + \omega bM)^2 + \omega^2(L_1 - aM)^2$$

$$\frac{\partial REAL\_NU}{\partial R_1} = (R_1 - aR_2)(1 + \omega M\frac{\partial b}{\partial R_1}) + (R_1 + R_3 + \omega bM)(1 - R_2\frac{\partial a}{\partial R_1})$$

$$+ \omega MR_2 b\frac{\partial a}{\partial R_1} - \omega R_2(L_1 - aM)\frac{\partial b}{\partial R_1}$$

$$\frac{\partial REAL\_NU}{\partial R_3} = (R_1 - aR_2)(1 + \omega M\frac{\partial b}{\partial R_3}) - R_2\frac{\partial a}{\partial R_3}(R_1 + R_3 + \omega bM)$$

$$+ \omega bMR_2\frac{\partial a}{\partial R_3} - \omega R_2(L_1 - aM)\frac{\partial b}{\partial R_3}$$

$$\frac{\partial DE}{\partial R_1} = 2(R_1 + R_3 + \omega bM)(1 + \omega M\frac{\partial b}{\partial R_1}) - 2\omega^2 M(L_1 - aM)\frac{\partial a}{\partial R_1}$$

$$\frac{\partial DE}{\partial R_3} = 2(R_1 + R_3 + \omega bM)(1 + \omega M\frac{\partial b}{\partial R_3}) - 2\omega^2 M(L_1 - aM)\frac{\partial a}{\partial R_3}$$

$$\begin{aligned}
\frac{\partial a}{\partial R_1} &= \frac{R_2 + R_4}{(R_2 + R_4)^2 + \omega^2 (L_2 + M)^2} \\
\frac{\partial a}{\partial R_3} &= \frac{R_2 + R_4}{(R_2 + R_4)^2 + \omega^2 (L_2 + M)^2} \\
\frac{\partial b}{\partial R_1} &= -\frac{\omega (L_2 + M)}{(R_2 + R_4)^2 + \omega^2 (L_2 + M)^2} \\
\frac{\partial b}{\partial R_3} &= -\frac{\omega (L_2 + M)}{(R_2 + R_4)^2 + \omega^2 (L_2 + M)^2}
\end{aligned} \tag{B.12}$$

Terms *a* and *b* are defined in eqns (A.11) and (A.12).

Comparisons of the calibrated values for R_1 and R_3 using 'phase shift method' (to adjust the output phase shift) and 'amplitude method' (to adjust the output amplitude) are shown in Fig (B.5). It is apparent that the results are exactly the same. In conclusion, these two methods are equivalent.

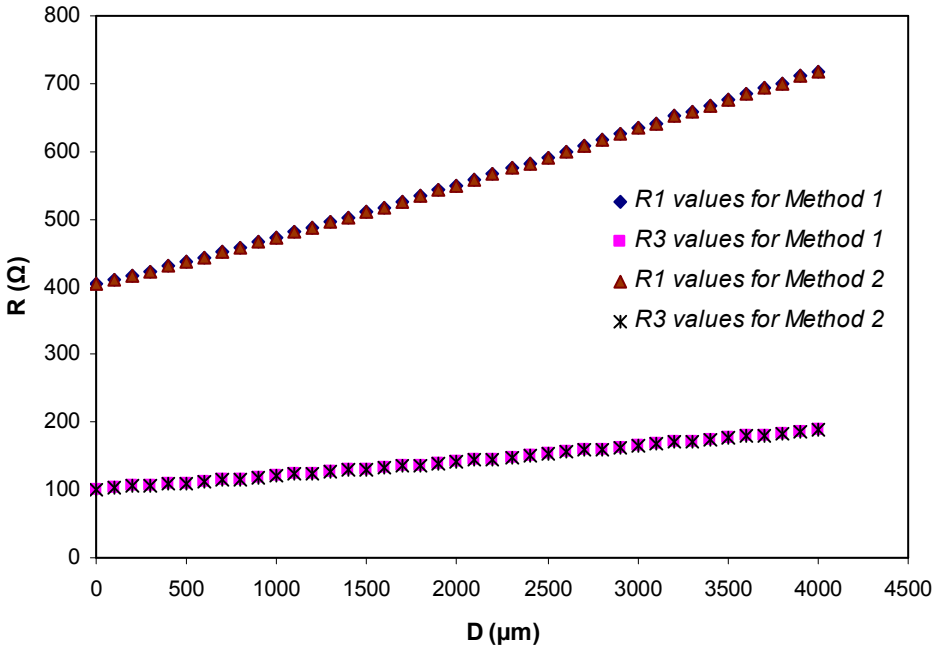

Fig B.5 Calibrated values of R_1 and R_3 as a function of gross displacement D, using phase judgment method (Method 1) and amplitude judgment method (Method 2) respectively. $R_1 = R_3 = 400\ \Omega$, $R_2 = R_4 = 100\ \Omega$, $f = 100$ kHz initially.

C. Gradient of the Output Voltage of the System

After calibration, the new values of R_1, $R3$ are R_1', R_3'. Assume that with a small axial displacement z, the new values of the L_1, L_2 and M is L_1', L_2' and M', thus the new values of a, b are a', b'. According to eqn. (A.8), the new output of the system can be written as:

$$V_o' = A_v.H_1'(j\omega).V_{in} = A_v.(REAL' + IMAG'j).V_{in} \tag{C.1}$$

Where $REAL'$ and $IMAG'$ are defined in the same way as $REAL'$ and $IMAG'$ except that R_1', R_3' replace R_1, R_3, $L_{1,2}'$, M' replace $L_{1,2}$, M and a', b' replace a, b.

Differentiating (C.1) with respect of z:

$$\frac{\partial V_o}{\partial z} = A_v.V_{in}.(\frac{\partial REAL'}{\partial z} + \frac{\partial IMAG'}{\partial z}j) \tag{C.2}$$

where

$$\begin{aligned}\frac{\partial REAL'}{\partial z} &= \frac{-R_2(R_1' + R_3' + \omega b'M')\frac{\partial a'}{\partial z} + (R_1' - a'R_2)(\omega M'\frac{\partial b'}{\partial z} + \omega b'\frac{\partial M}{\partial z})}{(R_1' + R_3' + \omega b'M')^2 + \omega^2(L_1' - a'M')^2} \\ &- \frac{\omega R_2((L_1' - a'M')\frac{\partial b'}{\partial z} + b'(\frac{\partial L_1}{\partial z} - M'\frac{\partial a'}{\partial z} - a'\frac{\partial M}{\partial z})}{(R_1' + R_3' + \omega b'M')^2 + \omega^2(L_1' - a'M')^2} \\ &- 2\omega[(R_1' - a'R_2)(R_1' + R_3' + \omega b'M') - b'R_2\omega(L_1' - a'M')] \\ &\cdot\frac{(R_1' + R_3' + \omega b'M')(M'\frac{\partial b'}{\partial z} + b'\frac{\partial M}{\partial z}) + \omega(L_1' - a'M')(\frac{\partial L_1}{\partial z} - M'\frac{\partial a'}{\partial z} - a'\frac{\partial M}{\partial z})}{[(R_1' + R_3' + \omega b'M')^2 + \omega^2(L_1' - a'M')^2]^2}\end{aligned} \tag{C.3}$$

$$\begin{aligned}\frac{\partial IMAG'}{\partial z} &= \frac{-R_2(R_1' + R_3' + \omega b'M')\frac{\partial b'}{\partial z} - R_2b'\omega(M'\frac{\partial b'}{\partial z} + b'\frac{\partial M}{\partial z})}{(R_1' + R_3' + \omega b'M')^2 + \omega^2(L_1' - a'M')^2} \\ &- \frac{\omega(R_1' - a'R_2)(\frac{\partial L_1}{\partial z} - M'\frac{\partial a'}{\partial z} - a'\frac{\partial M}{\partial z}) + \omega R_2\frac{\partial a'}{\partial z}(L_1' - a'M')}{(R_1' + R_3' + \omega b'M')^2 + \omega^2(L_1' - a'M')^2} \\ &- 2\omega[-b'R_2(R_1' + R_3' + \omega b'M') - \omega(R_1' - a'R_2)(L_1' - a'M')] \\ &\cdot\frac{(R_1' + R_3' + \omega b'M')(M'\frac{\partial b'}{\partial z} + b'\frac{\partial M}{\partial z}) + \omega(L_1' - a'M')(\frac{\partial L_1}{\partial z} - M'\frac{\partial a'}{\partial z} - a'\frac{\partial M}{\partial z})}{[(R_1' + R_3' + \omega b'M')^2 + \omega^2(L_1' - a'M')^2]^2}\end{aligned} \tag{C.4}$$

and

$$\frac{\partial a^{'}}{\partial z}=\frac{\omega^2[(\frac{\partial L_1}{\partial z}+\frac{\partial M}{\partial z})(L_2^{'}+M^{'})+(L_1^{'}+M^{'})(\frac{\partial L_2}{\partial z}+\frac{\partial M}{\partial z})][(R_2+R_4)^2+\omega^2(L_2^{'}+M^{'})^2]}{[(R_2+R_4)^2+\omega^2(L_2+M)^2]^2}$$
$$-\frac{2\omega^2(L_2^{'}+M^{'})(\frac{\partial L_2}{\partial z}+\frac{\partial M}{\partial z})[(R_1^{'}+R_3^{'})(R_2+R_4)+\omega^2(L_1^{'}+M^{'})(L_2^{'}+M^{'})]}{[(R_2+R_4)^2+\omega^2(L_2^{'}+M^{'})^2]^2} \quad \text{(C.5)}$$

$$\frac{\partial b^{'}}{\partial z}=\frac{\omega[(R_2+R_4)(\frac{\partial L_1}{\partial z}+\frac{\partial M}{\partial z})-(R_1^{'}+R_3^{'})(\frac{\partial L_2}{\partial z}+\frac{\partial M}{\partial z})][(R_2+R_4)^2+\omega^2(L_2^{'}+M^{'})^2]}{[(R_2+R_4)^2+\omega^2(L_2^{'}+M^{'})^2]^2}$$
$$-\frac{2\omega^2(L_2^{'}+M^{'})(\frac{\partial L_2}{\partial z}+\frac{\partial M}{\partial z})[(R_2+R_4)(L_1^{'}+M^{'})-(R_1^{'}+R_3^{'})(L_2^{'}+M^{'})]}{[(R_2+R_4)^2+\omega^2(L_2^{'}+M^{'})^2]^2} \quad \text{(C.6)}$$

Eqns. (C.2) to (C.6) indicate that $\partial V_0/\partial z$ is function of $\partial L_{1,2}^{'}/\partial z$, $\partial M^{'}/\partial z$, R_1, R_2, R_3, R_4, ω, $L_{1,2}^{'}$ and $M^{'}$, all of which are invariable during *micromotion* testing except $L_{1,2}^{'}$, $M^{'}$, $\partial L_{1,2}^{'}/\partial z$ and $\partial M^{'}/\partial z$. Substitute the measured results for these parameters shown in eqn. (5.1) to eqn. (C.2) to calculate $\partial V_0/\partial z$, and it can be seen in Fig C.1 that the values for $\partial V_0/\partial z$ with respect to z at different gross displacement D (*migration*) are preserved constant (with less than ±1% fluctuations) over the range of ± 300 μm irrespective of the variations in $L_{1,2}^{'}$ and $M^{'}$, i.e. The impact of the variations in $L_{1,2}^{'}$ and $M^{'}$ on $\partial V_0/\partial z$ can be ignored, and in eqns. (C.3) to (C.6) these variables can be replaced by the values of $L_{1,2}$ and M at $z = 0$. As a result, the output voltage of the system is linear with respect to the implant displacement z over the range so long as $\partial L_{1,2}/\partial z$ and $\partial M/\partial z$ are constant.

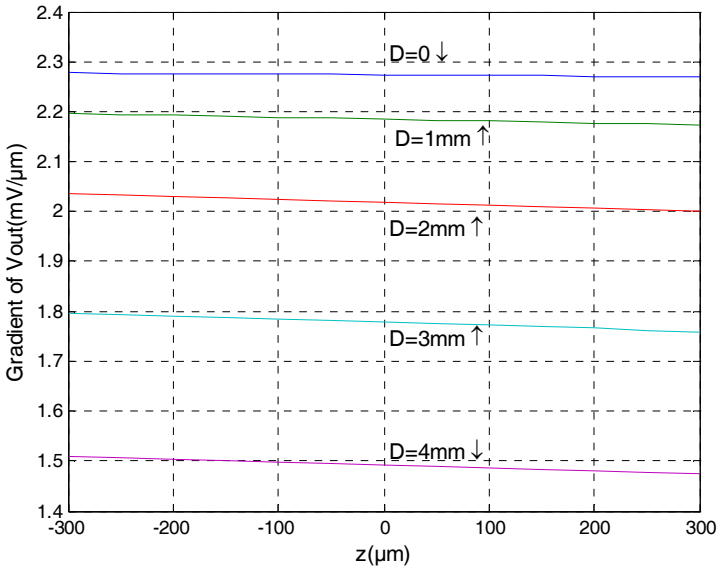

Fig C.1 The output gradient of the amplifier connected to the *RL* bridge. $R_1 = R_2 = 400$ Ω and $R_3 = R_4 = 100$ Ω initially. $f = 100$ kHz. It can be seen that a nearly constant gradient is preserved over the range between -300 μm and 300 μm, with different initial gross displacement D (*migration*).

D. Choice of the Resistor Values R_2 and R_4

As noted in Section 4.3.1, the operation of the calibration algorithm is much simplified if two of the resistors in the *RL* bridge are fixed, say R_2 and R_4. To determine suitable values for these components, consider the first step in the calibration algorithm which chooses the resonant frequency of the bridge by setting the function $IMAG = 0$. In the simplest case when $M = 0$ and assuming that $R_1 = R_2$ and $R_3 = R_4$, the expression for resonance reduces to:

$$\left(R_2 + R_4\right)^2 - \omega^2 L_1 L_2 = 0 \tag{D.1}$$

For $f = 100$ kHz and $L_1 = L_2 = 800$ μH, $(R_2 + R_4) \approx 500$ Ω. The same, $(R_2 + R_4) \approx 125$ Ω at 25 kHz, 250 Ω at 50 kHz and 1 kΩ at 200 kHz. MATLAB simulations indicate that even for $M \neq 0$, these typical values change very little. Also, due to the effects of the calibration, the values are not critical.

E. Influence of Phase Shift in Preamplifier and Errors of Phase Detectors on the Calibration Process

Assume that the amplifier has a phase shift of ϕ, the transfer function of the bridge is:

$$\begin{aligned} H_1(j\omega) &= (REAL + j.IMAG)e^{j\phi} \\ &= \cos\phi.REAL - \sin\phi.IMAG + j.(\cos\phi.IMAG + \sin\phi.REAL) \end{aligned} \tag{E.1}$$

Equation (B.1) describing the second step of the calibration then can be modified as:

$$\begin{aligned} \cos\phi.REAL(R_{1,n}, R_{3,n-1}) - \sin\phi.IMAG(R_{1,n}, R_{3,n-1}) = 0 \\ \cos\phi.IMAG(R_{1,n}, R_{3,n}) + \sin\phi.REAL(R_{1,n}, R_{3,n}) = 0 \end{aligned} \tag{E.2}$$

Errors of the phase detectors can also influence the transfer function. Assume that the errors of the 0 or 180º phase detector is θ_1, the errors of the ±90º phase detector is θ_2. Then eqn. (B.1) can be modified as:

$$\begin{aligned} \cos\theta_2.REAL(R_{1,n}, R_{3,n-1}) + \sin\theta_2.IMAG(R_{1,n}, R_{3,n-1}) = 0 \\ \cos\theta_1.IMAG(R_{1,n}, R_{3,n}) - \sin\theta_1.REAL(R_{1,n}, R_{3,n}) = 0 \end{aligned} \tag{E.3}$$

It is apparent that the resonant frequency of the bridge can be changed due to the phase shift of the preamplifier or the errors of the phase detection process.

The influence of the preamplifier phase shift and the phase detection errors on the calibrated values of R_1 and R_3 is discussed below.

As shown in eqn. (E.2), $REAL + j.IMAG = 0$ is the sufficient and necessary condition of $(REAL + j.IMAG).e^{j\phi} = 0$. In other words, the phase offset caused by the preamplifier doesn't change the calibrated values of R_1 and R_3, as long as R_1 and R_3 are irrespective of the operating frequency ω.

In the ideal case where $M = 0$, eqn. (B.9) reduces to:

$$\begin{aligned} R_{1,\infty} &= \frac{L_1}{L_2} R_2 \\ R_{3,\infty} &= \frac{L_1}{L_2} R_4 \end{aligned} \tag{E.4}$$

As shown in eqn. (E.4), in the ideal case the calibrated values of R_1 and R_3 are irrespective of ω, so the calibrated values of R_1 and R_3 remain the same so long as the calibration is successful. In other words, in the ideal case the final values of R_1 and R_3 are both independent of the phase shift of the preamplifier.

As for the influence of the phase detection errors, although two new parameters θ_1 and θ_2 are brought in to the calibration algorithm (eqn. (E.3)), the judgment of the completion of the calibration is that the value of $|H_1(j\omega)|$ is less than a threshold as mentioned in Section 4.3.1, i.e. the judgment is made at the output of the preamplifier rather than the output of the phase detectors. Therefore, the phase detection errors θ_1 and θ_2 don't influence the calibrated values of R_1 and R_3, as long as the calibration is successful and R_1 and R_3 are irrespective of the operating frequency ω, such as in the ideal case ($M = 0$).

In the general case where $M \neq 0$, the issue is more complicated as the calibrated values of R_1 and R_3 depend on the resonant frequency ω. The simulation results have shown that neither the phase shift of the preamplifier nor the errors of the phase detectors have impact on the calibrated values of R_1 and R_3. However the relevant theoretical analysis is beyond the scope of the thesis.

F. Description of the Whole System Including the Telemetry

The whole implantable system for in-vivo measurement generally comprises three parts: the external part, the internal part, and the inductive *transcutaneous* link, as shown in Fig F.1. The external part includes a data receiving system and a terminal PC for control and data analysis. The internal part contains a sensor device as the essential module, which has been designed in our project, and a data-processing-and-transmission system. Power and commands are transmitted from the external part to the internal part, while data are transmitted in the other way round, via an inductive *transcutaneous* link. A pair of coils is involved in the transmission as the transmitter and the receiver. Such link can be considered as a *telemetry* system.

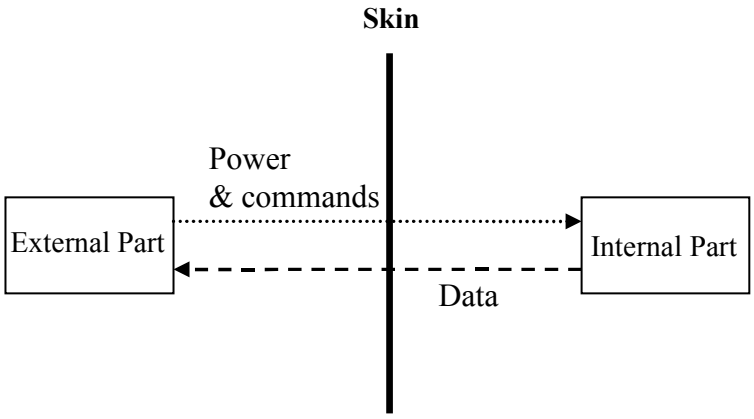

Fig F.1 Diagram for the whole system including the telemetry